EFFECT OF GRAIN SIZE AND MECHANICAL STRESS ON POLARIZATION SWITCHING OF FERROELECTRICS

by

Keisuke Yazawa

A Dissertation

Submitted to the Faculty of Purdue University

In Partial Fulfillment of the Requirements for the degree of

Doctor of Philosophy

School of Materials Engineering

West Lafayette, Indiana

August 2020

THE PURDUE UNIVERSITY GRADUATE SCHOOL
STATEMENT OF COMMITTEE APPROVAL

Dr. John E. Blendell, Co-chair

School of Materials Engineering

Dr. Carol A. Handwerker, Co-chair

School of Materials Engineering

Dr. R. Edwin García

School of Materials Engineering

Dr. Eric P. Kvam

School of Materials Engineering

Approved by:

Dr. David F. Bahr

Dedicated to my wife and daughter

ACKNOWLEDGMENTS

I would like to thank my advisors, Prof. John Blendell and Prof. Carol Handwerker, for all the support, instructions and encouragement which they have given me. They kindly invited my family to fun events, dinner and creek. I also thank my committees, Prof. Edwin García and Prof. Eric Kvam for fruitful discussions about ferroelectric thermodynamics and phase transformation, which turn out a fundamental knowledge base for my achievement. I would like to thank my collaborators, Prof. Hiroshi Uchida at Sophia University and Prof. Hiroshi Funakubo at Tokyo Institute of Technology for ferroelectric samples. The experimental results in this dissertation would not be made without their high quality ferroelectric thin films. I also thank Prof. Benjamin Ducharne at INSA Lyon for introducing and teaching me Barkhausen noise and sharing his insightful ideas. I would like to acknowledge my friends Dr. Wolfgang Rheinheimer's family and MSE graduate students for numerous discussions and joyful time spending together. They certainly have enriched my life. Finally, I thank Purdue technical assistance program for opportunities working with companies and funding my PhD program.

TABLE OF CONTENTS

LIST OF TABLES

LIST OF FIGURES

EXTRA HEADINGS

a_{ij}	Second order Landau expansion coefficient
a_{ijkl}	Fourth order Landau expansion coefficient
a_{ijklmn}	Sixth order Landau expansion coefficient
c_{ijkl}	Elastic stiffness tensor
D_i	Electric displacement tensor
d_{ijk}	Piezoelectric coefficient tensor in d form
δ_{ij}	Kronecker delta
e_{ijk}	Piezoelectric coefficient tensor in e form
E_i	Electric field tensor
EBN	Ferroelectric Barkhausen noise
EBN_{energy}	Ferroelectric Barkhausen noise energy
ε_{ij}	Strain tensor
ε^*_{ij}	Stress-free strain tensor
ε^c_{ij}	Constrained strain tensor
ε^e_{ij}	Elastic strain tensor
f	Helmholtz free energy density
g	Elastic Gibbs free energy density
g'	Gibbs free energy density
Γ_{iJKl}	Electro – elastic constant matrix
H	Elastic enthalpy
H'	Enthalpy
$I_{Barkhausen}$	Barkhausen raw signal in current
k_{ij}	Permittivity tensor
MBN	Ferromagnetic Barkhausen noise
MBN_{energy}	Ferromagnetic Barkhausen noise energy
P_i	Polarization tensor
Q	Heat
Q_{ijkl}	Electrostrictive tensor

S	Entropy
s_{ijkl}	Elastic compliance tensor
S_{ijkl}	Eshleby's tensor
S'_{IjKl}	Extended Eshelby's tensor like matrix
s_{ijkl}	Fourth order Landau expansion coefficient
σ_{ij}	Stress tensor
t	Time
t_0	Excitation field time period
Σ_{iJ}	Stress – electric displacement matrix
T	Temperature
U	Internal energy
$V_{Barkhausen}$	Barkhausen raw signal in voltage
W	Work
w	Out-of-plane (001) oriented domain width
Z_{Kl}	Stain – electric field matrix
Z^*_{Kl}	Stress – electric displacement free stain – electric field matrix
Z^c_{Kl}	Constrained stain – electric field matrix

ABSTRACT

The polarization response such as ferroelectric and ferroelastic switching in ferroelectrics is the important feature for ferroelectric and electromechanical applications. In polycrystalline form ferroelectrics, effects of the microstructural parameters such as texture, grain size, and residual stress are there and have not fully been understood. Among these effects, (1) the origin of grain size effects on ferroelastic switching, (2) mechanical stress effects on polarization switching, and (3) ferroelectric switching kinetics and the relationship to grain boundaries are investigated.

Firstly, the microscopic origin of ferroelastic switching suppression in smaller grains is discovered using a microscopic probing technique (piezoresponse force microscopy). It is demonstrated that there is no independent grain size effect on ferroelastic switching; the grain size affects the domain structure in a grain, and the domain structure plays an important role in the ferroelastic switching suppression. This result suggests that the grain size is not an independent critical parameter for the electromechanical property degradation in a grain < 1 μm as the ferroelastic switching is a dominant component for the electromechanical property.

The study about the mechanical stress effects on the electric field induced polarization switching rationalizes the emergence of the electric field induced low-symmetry phases observed in tetragonal $Pb(Zr,Ti)O_3$ and $BaTiO_3$ ceramics after poling. It is demonstrated that a shear stress plays an important role in stabilizing the monoclinic phase in $Pb(Zr,Ti)O_3$ whereas a normal stress along the polarization axis is a key for the monoclinic phase in $BaTiO_3$ with a thermodynamic approach. It is suggested that the fraction of the low-symmetry phase, which is important for the large electromechanical property, can be engineered by applying an appropriate stress.

For the work about ferroelectric switching kinetics, the first direct Barkhausen noise associated with ferroelectric switching is measured. The domain switching time is quantified by the frequency of the Barkhausen noise. It is discovered that the dominant domain wall pinning site is grain boundaries based on the domain wall jump distance between pinning sites calculated from the switching time. This result suggests that the technique is a good tool for understanding the relationship between microstructure – domain wall kinetics.

In sum, the mechanisms of the polarization switching suppression due to domain structure and grain boundaries, and the emergence of the low symmetry phases due to stresses are revealed.

These discoveries facilitate further improvements of the device performances with engineering the domain structure, grain boundaries and residual stress.

1. INTRODUCTION

1.1 Ferroelectricity

Ferroelectric materials have the switchable spontaneous polarization and non-linearity (hysteresis) in a polarization vs electric field curve [1]. Due to the attractive characteristic, the ferroelectric materials are used in a wide range of applications such as FeRAM, actuator and sensor devices [2–4]. Landau theory describes a phenomenological model for the ferroelectric physics [1,5]. Starting from fundamental thermodynamics, according to the first and second law of thermodynamics, the deferential of the internal energy can be expressed as,

$$dU = dQ + dW = TdS + \sigma_{ij}d\varepsilon_{ij} + E_i dP_i \tag{1.1}$$

where Q is the heat and W is the work done by the small amount of strain change and the polarization change here (other terms can be added depending on a system). Then, the elastic Gibbs free energy density, g is defined as [5],

$$g \equiv H - TS \tag{1.2}$$

where T is the temperature, S is the entropy and H is the elastic enthalpy which is defined as [5],

$$H \equiv U - \sigma_{ij}\varepsilon_{ij} \tag{1.3}$$

From equations (1.1) to (1.3), the differential of the elastic Gibbs free energy density can be expressed as,

$$dg = -SdT - \varepsilon_{ij}d\sigma_{ij} + E_i dP_i \tag{1.4}$$

With this equation and the second law of thermodynamics $dQ \leq T\mathrm{d}S$ at constant temperature, stress and polarization, the elastic Gibbs free energy density satisfies the well-known relationship $dg \leq 0$. This gives us an important insight that a negative value in dg is necessary for a spontaneous process, and a system reaches the equilibrium when $dg = 0$ at constant temperature, stress and polarization condition.

To identify the equilibrium state with the elastic Gibbs free energy density function, finding free energy density minima with the control variables which are temperature, stress and polarization is a convenient way. To express the non-linearity of a polarization - electric field curve in ferroelectrics, one needs to consider the higher order terms with Taylor expansion, namely,

$$g(P_i, \sigma_{ij}, T) = \sum_{k=0}^{n} \frac{1}{k!}\left\{P\left(\frac{\partial}{\partial P_i}\right)_{\sigma,T} + \sigma\left(\frac{\partial}{\partial \sigma_{ij}}\right)_{P,T} + T\left(\frac{\partial}{\partial T}\right)_{P,\sigma}\right\}^k g \tag{1.5}$$

Assuming the isothermal condition for convenience, equation (1.5) can be written out in full as follows,

$$g(P_i, \sigma_{ij}; T) = g_0 + \frac{1}{2!}\left(\frac{\partial^2 g}{\partial P_i \partial P_j}\right)_{\sigma,T} P_i P_j + \frac{1}{4!}\left(\frac{\partial^4 g}{\partial P_i \partial P_j \partial P_k \partial P_l}\right)_{\sigma,T} P_i P_j P_k P_l + \cdots + \frac{1}{2!}\left(\frac{\partial^2 g}{\partial \sigma_{ij} \partial \sigma_{kl}}\right)_{P,T} \sigma_{ij}\sigma_{kl} + \cdots + \frac{1}{2!}\left(\frac{\partial^3 g}{\partial \sigma_{ij} \partial P_k \partial P_l}\right)_{T} \sigma_{ij} P_k P_l + \cdots \quad (1.6)$$

The first two terms represent the second and forth order of the electric free energy density, the third term is the elastic energy density, and the fourth term is the polarization – stress coupling energy density. These terms continue going higher orders, so that an approximation at a certain order is usually done. Note that the summation symbols for each term are omitted. The partial derivatives in the equation corresponds to Landau coefficients and are determined by experimental observation in a constant temperature and stress condition for the coefficients of the electric free energy density, in a constant temperature and polarization for the elastic free energy density, and in a constant temperature for the polarization – stress coupling free energy density terms. These conditions and the control variables are exchangeable via Legendre transformation at the starting point when the free energy density is defined, i. e. one can select preferable control variables and coefficients in accordance with an assumed condition. For instance, if polarization and strain are the control variables, the Helmholtz free energy density *f* defined as,

$$f \equiv U - TS \quad (1.7)$$

$$df = -SdT + \sigma_{ij} d\varepsilon_{ij} + E_i dP_i \quad (1.8)$$

is useful. The Taylor expansion expression of the Helmholtz free energy density at the isothermal condition can be expressed as,

$$f(P_i, \varepsilon_{ij}; T) = f_0 + \frac{1}{2!}\left(\frac{\partial^2 f}{\partial P_i \partial P_j}\right)_{\varepsilon,T} P_i P_j + \frac{1}{4!}\left(\frac{\partial^4 f}{\partial P_i \partial P_j \partial P_k \partial P_l}\right)_{\varepsilon,T} P_i P_j P_k P_l + \cdots + \frac{1}{2!}\left(\frac{\partial^2 f}{\partial \varepsilon_{ij} \partial \varepsilon_{kl}}\right)_{P,T} \varepsilon_{ij}\varepsilon_{kl} + \cdots + \frac{1}{2!}\left(\frac{\partial^3 f}{\partial \varepsilon_{ij} \partial P_k \partial P_l}\right)_{T} \varepsilon_{ij} P_k P_l + \cdots \quad (1.9)$$

The coefficients may be different from the ones in the elastic Gibbs free energy density function (equation (1.6)) even though they are related and mathematically transformed [6–8]. This Helmholtz free energy density function is useful for investigating the equilibrium state in a epitaxially strained film as the strain can be fixed in a fully confined crystal lattice by a substrate [9–11].

To explain the ferroelectric behavior from the free energy density, a simple one-dimensional version of equation (1.6) in the stress-free state is considered [1], namely,

$$g(P) = aP^2 + bP^4 + cP^6 + \cdots \tag{1.10}$$

where *a*, *b* and *c* are the Landau coefficients. The polarization derivative of the free energy density, $\partial g/\partial P$ corresponds to the electric field, thereby,

$$\frac{\partial g}{\partial P} = E = 2aP + 4bP^3 + 6cP^5 + \cdots \tag{1.11}$$

Figure 1.1 shows a free energy density vs polarization curve and a polarization vs electric field curve based on equation (1.10) and (1.11). The free energy density curve exhibits a double well potential whose minima represent the spontaneous polarization in ferroelectrics. The broken line is in the negative curvature region, which can be defined as $\partial^2 g/\partial P^2 < 0$. A polarization in this region is unstable and spontaneously moves towards one of the energy minima, analogous to spinodal decomposition. In the polarization – electric field curve, the polarization range shown with the broken line is forbidden due to the instability in the free energy density. The electric field reaching the instability region, which is called the coercive electric field, induces the abrupt polarization jump, so that the curve shows the hysteresis.

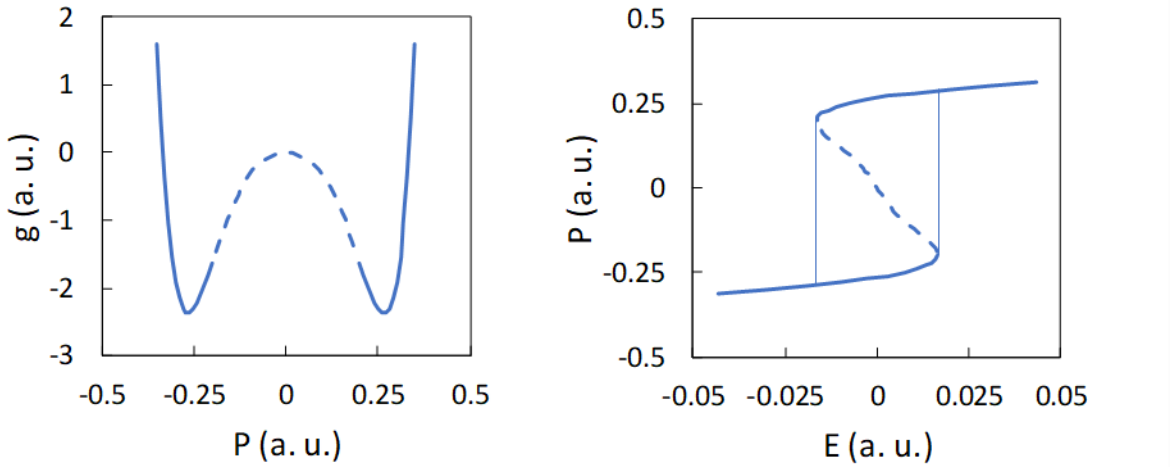

Figure 1.1. Gibbs free energy density vs polarization curve and polarization vs electric field curve.

One of the most investigated ferroelectric crystal systems is a perovskite oxide. The perovskite structure ferroelectrics are widely used for ferroelectric device application due to its

ferroelectric properties as well as its stability and usability in a ceramic form [1]. In a perovskite structure material, the spontaneous polarization switchability, which is the definition of ferroelectricity, is achieved by ion motions in a crystal under an electric field. Figure 1.2 shows the schematic diagram of the unit cell of a perovskite oxide $BaTiO_3$ [12]. The off body centered Ti^{4+} ion and off face centered O^{2-} ions produce the gap of the positive and negative charge gravity center, so that the permanent spontaneous polarization is generated. An external electric field higher than the coercive field makes the ions towards the opposite off-centered positions, then the spontaneous polarization direction also switches.

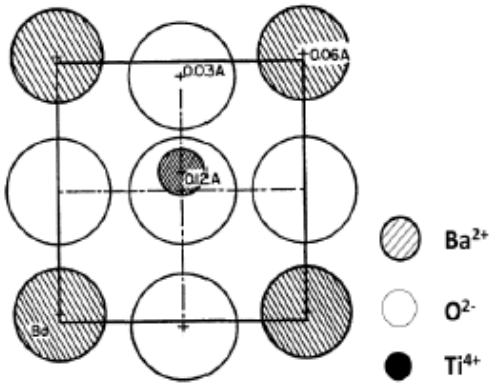

Figure 1.2. Schematic drawing of perovskite oxide, $BaTiO_3$. (Image sourced from [12])

1.2 Electric Field Induced Response in Ferroelectrics

Beyond ferroelectric polarization switching discussed in chapter 1.1, other electric field induced responses exist in ferroelectrics: piezoelectricity, ferroelastic switching and polarization rotation accompanying phase transformation, which are discussed here. These responses are important especially for electromechanical device applications such as an actuator, sensor and energy harvester devices since they usually accompany the electric field induced strains.

1.2.1 Piezoelectricity

Piezoelectricity is the electrical – mechanical coupling to the non-centrosymmetric nature of the ferroelectric crystal. All ferroelectric materials possess the piezoelectricity since the non-centrosymmetric is a necessary condition for a polar crystal. When an electric field is applied to ferroelectric materials, a dipole associated with the gap between the positive and negative charge gravity centers responds to the electric field, so that a lattice strain is induced, called the inverse

piezoelectricity. With stress, electric field and temperature as independent variables, the differential of a strain may be written as an exact differential form such as [6],

$$d\varepsilon_{ij} = \left(\frac{\partial \varepsilon_{ij}}{\partial \sigma_{kl}}\right)_{E,T} d\sigma_{kl} + \left(\frac{\partial \varepsilon_{ij}}{\partial E_k}\right)_{\sigma,T} dE_k + \left(\frac{\partial \varepsilon_{ij}}{\partial T}\right)_{\sigma,E} dT \tag{1.12}$$

Similarly, the differential of polarization can be expressed as[6],

$$dP_i = \left(\frac{\partial P_i}{\partial \sigma_{jk}}\right)_{E,T} d\sigma_{jk} + \left(\frac{\partial P_i}{\partial E_j}\right)_{\sigma,T} dE_j + \left(\frac{\partial P_i}{\partial T}\right)_{\sigma,E} dT \tag{1.13}$$

Note that the Einstein summation notation is employed for these equations [6]. With introducing Gibbs free energy density, g' defined as [5,6],

$$g' \equiv H' - TS \tag{1.14}$$

$$H' \equiv U - \sigma_{ij}\varepsilon_{ij} - E_i P_i \tag{1.15}$$

the differential of the Gibbs free energy density can be expressed as,

$$dg' = -\varepsilon_{ij} d\sigma_{ij} - P_i dE_i - SdT \tag{1.16}$$

The differential of the Gibbs free energy density can also be written in the exact differential form, namely [6],

$$dg' = \left(\frac{\partial g'}{\partial \sigma_{ij}}\right)_{E,T} d\sigma_{jk} + \left(\frac{\partial g'}{\partial E_i}\right)_{\sigma,T} dE_j + \left(\frac{\partial g'}{\partial T}\right)_{\sigma,E} dT \tag{1.17}$$

Therefore, with comparing equation (1.16) to equation (1.17), one can get

$$\left(\frac{\partial g'}{\partial \sigma_{ij}}\right)_{E,T} = -\varepsilon_{ij}\,, \quad \left(\frac{\partial g'}{\partial E_i}\right)_{\sigma,T} = -P_i \tag{1.18}$$

From Maxwell relations,

$$\left(\frac{\partial}{\partial E_k}\left(\frac{\partial g'}{\partial \sigma_{ij}}\right)\right)_T = \left(\frac{\partial}{\partial \sigma_{ij}}\left(\frac{\partial g'}{\partial E_k}\right)\right)_T \tag{1.19}$$

Thus, by plugging equation (1.18) into equation (1.19), the electrical – mechanical coupling coefficients in equations (1.13) and (1.14) has the following relationship [6],

$$\left(\frac{\partial \varepsilon_{ij}}{\partial E_k}\right)_{\sigma,T} = \left(\frac{\partial P_k}{\partial \sigma_{ij}}\right)_{E,T} = d_{kij} \tag{1.20}$$

This third rank tensor is one form of direct and inverse piezoelectric coefficients. Other forms can be obtained by changing independent variables.

The tensor components of the piezoelectric coefficient depend on symmetry of a crystal [6]. One of the most common symmetries in ferroelectrics is *4mm* (e. g. $BaTiO_3$ and $PbTiO_3$). Figure 1.3 shows the schematic diagram of a *4mm* crystal on the Cartesian coordinate. The red solid line along x_3 axis is the four-fold rotation axis. The x_1-x_3 plane shown as the broken red line is a mirror plane, and the plane with the broken-dot red line is another mirror plane. Considering the four-fold rotation operation (clockwise), the coordinate axes converts from x_1 to $-x_2$, x_2 to x_1, and x_3 to x_3. This operation should give the identical property due to the crystal symmetry, so that the piezoelectric coefficient tensor needs to satisfy the following relations: $d_{113} = d_{223}$, $d_{123} = -d_{213}$, $d_{133} = -d_{133}$… Among them, only $d_{113} = d_{223}$, $d_{123} = -d_{213}$, $d_{311} = d_{322}$ and d_{333} are the non-zero components in the four-fold rotation operation due to the tensor symmetry $d_{ijk} = d_{ikj}$, which comes from the strain or stress tensor relationship $\varepsilon_{jk} = \varepsilon_{kj}$ or $\sigma_{jk} = \sigma_{kj}$. Similarly, given the other mirror operations, the final non-zero components are $d_{113} = d_{223}$, $d_{311} = d_{322}$ and d_{333}. Therefore, the final piezoelectric coefficient tensor components in a *4mm* crystal is as follows,

$$d_{ijk} = \begin{pmatrix} 0 & 0 & 0 & 0 & d_{113} & 0 \\ 0 & 0 & 0 & d_{113} & 0 & 0 \\ d_{311} & d_{311} & d_{333} & 0 & 0 & 0 \end{pmatrix} \tag{1.21}$$

Note that the components are written in a matrix, not a tensor for visualization. In a *4mm* crystal, an electric field applied along the 3 axis causes normal strains in all three directions, and an electric field applied along the 1 or 2 axis induces a shear strain which is ε_{13} or ε_{23}. Other symmetry crystals can be investigated in the same manner, and the results are tabulated in literature [6].

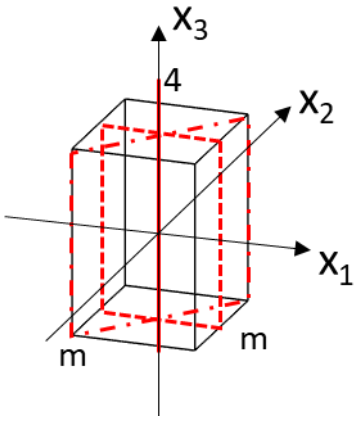

Figure 1.3. Symmetry operations of *4mm* crystal.

1.2.2 Ferroelastic Switching

Ferroelasticity is known as a non-linear (hysteresis) relationship between stress and strain, analogous to other ferroics: ferromagnetic and ferroelectric. It is originated from the switchable energetically equivalent orientation states in a crystallographically anisotropic crystal switched by an applied mechanical stress [13,14]. In ferroelectric materials, it is known that a mechanical stress as well as an electric field induce ferroelastic switching as the crystallographic anisotropy is related to the spontaneous polarization direction [15]. Figure 1.4 shows a schematic image of electric field induced ferroelastic switching in a $BaTiO_3$ type tetragonal ferroelectric material. The lattice parameter *c* is greater than the lattice parameter *a* due to the spontaneous polarization distortion. The six directions to the vertices of TiO_6 octahedral in a perovskite structure are equivalent in the parent cubic phase. By applying an external electric field in the tetragonal phase, a crystal whose polarization axis is perpendicular to the electric field direction can turn to a crystal whose polarization axis is parallel to the electric field direction [16]. The strain induced by an electric field E_z can be expressed as [15],

$$\varepsilon_{zz} = \frac{c}{a} - 1 \tag{1.22}$$

where *c* and *a* are the lattice parameters in a tetragonal crystal. Note that the electric field and strain direction *z* is described in the lab frame as the crystal frame is inconvenient in this case because of the crystal reorientation. As equation (1.22) shows, the strain associated with ferroelastic switching depends on the material tetragonality. For instance, in tetragonal $BaTiO_3$, the ferroelastic strain can be 1.1 % as a = 3.992 and c = 4.036 [17], which is much higher than a piezoelectric strain ($\varepsilon_{33} = d_{333}E_3$ = 0.009 % at d_{333} = 90 pm/V [18] and E_3 = 1 MV/m). Figure 1.5 shows the reported electric field - strain curve in a $BaTiO_3$ single crystal [19]. Nearly 1 % of non-linear strain was observed, in agreement with the calculation above. In $BaTiO_3$ base bulk ceramics, the dominance of the ferroelastic strain were also reported as shown in Figure 1.6 [20]. The vigorous X-ray diffraction results separating the total strain into the lattice strain (piezoelectric strain, green line) and the crystal reorientation (ferroelastic strain, red line). The ferroelastic strain larger than the piezoelectric strain can be seen in the bulk ceramics. Therefore, the ferroelastic strain induced by an electric field plays a dominant role in the electric field induced strain. As the tetragonality is the controlling parameter for the ferroelastic strain, large tetragonality materials have been suggested to achieve a higher electric field induced ferroelastic strain [21,22].

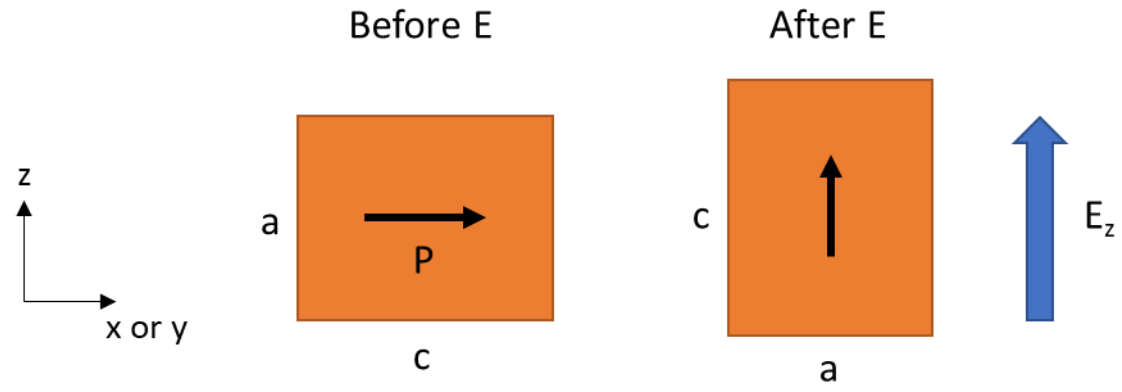

Figure 1.4. Schematic image of electric field induced ferroelastic switching in tetragonal ferroelectrics.

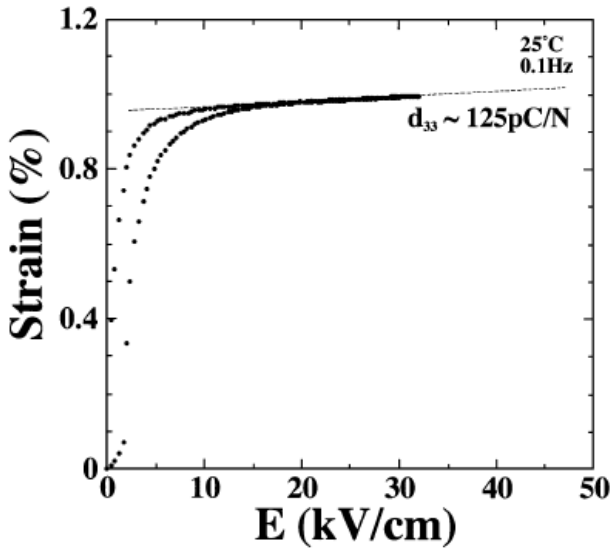

Figure 1.5. Electric field induced strain in $BaTiO_3$ single crystal. (Figure sourced from [19])

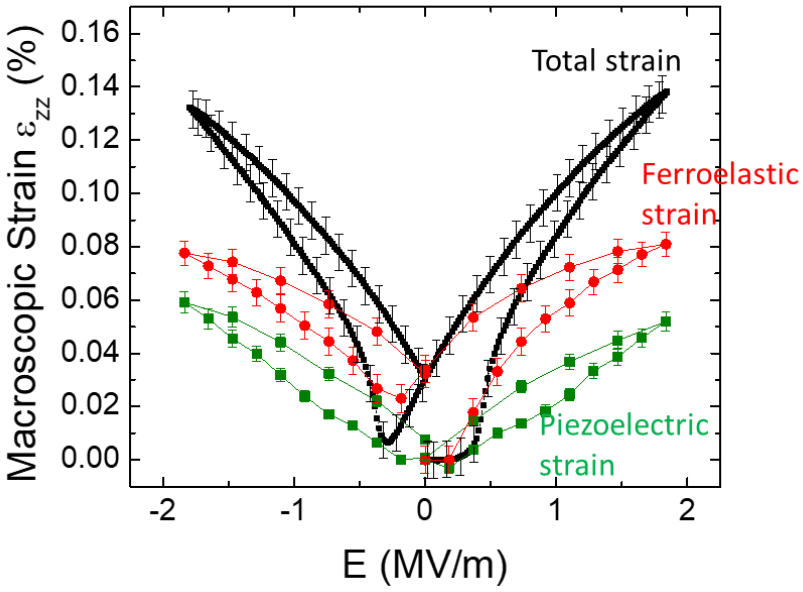

Figure 1.6. Piezoelectric (green) and ferroelastic switching (red) contributions to electric field induced strain in (Ba,Ca)(Zr,Ti)O_3 ceramics. (Figure sourced from [20])

1.2.3 Polarization Rotation and Phase Transformation

An electric field can also induce polarization rotation accompanying phase transformation. Figure 1.7 shows an experimental electric field induced strain curve in a $Pb(Zn_{1/3}Nb_{2/3})O_3$-$PbTiO_3$ single crystal and a model to explain the behavior [23]. The experimentally observed strain (Figure 1.7a) can be divided into the three stages A, B and C depending of the curve slope [23]. The theoretical calculation suggests that these stages are originated from polarization rotation from pseudo cubic [111] to [001] as shown in Figure 1.7b and c [23]. In accordance with polarization direction rotation, the crystal symmetry also transforms from rhombohedral to monoclinic to tetragonal as the spontaneous polarization direction directly relates to the crystallographic lattice distortion [23]. With the crystal symmetry transformation, the large electric field induced strain in this material can be explained.

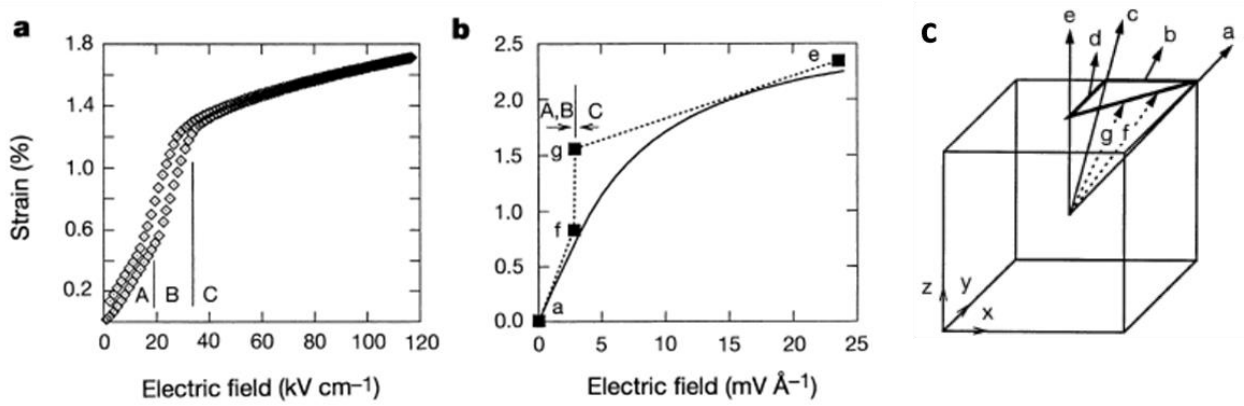

Figure 1.7. Strain – electric field relationship via polarization rotation. (a) Experimental result in $Pb(Zn_{1/3}Nb_{2/3})O_3$-$PbTiO_3$ single crystal. (b) Theoretical calculation for strain – electric field. (c) Schematic drawing of polarization direction. (Figure sourced from [23])

The polarization rotation is also seen in other ferroelectrics. In $Na_{0.5}Bi_{0.5}TiO_3$-$BaTiO_3$ single crystal [24] and ceramics [25], an electric field applied along the sample normal direction induces phase transformation from rhombohedral to tetragonal whose spontaneous polarization direction aligns to the sample normal direction, as shown in Figure 1.8 [24]. In these X-ray diffraction patterns, the intensities of the tetragonal peaks indicating the volume fraction of the tetragonal phase increase, and the intensities of the rhombohedral peaks decrease with increasing the applied DC electric field. Similar polarization rotation is seen in more typical and classic perovskite ferroelectrics such as $BaTiO_3$ [26] and $Pb(Zr,Ti)O_3$ (PZT) ceramics [27]. Figure 1.9 shows the X-ray diffraction patterns before and after poling in PZT [27]. After poling, ferroelastic switching ((100) domain to (001) domain) as well as a new peak attributed to a monoclinic phase are observed. This result suggests that an electric field induces the tetragonal - monoclinic phase transformation associated with polarization rotation. This monoclinic phase is thought of as a key for the large electromechanical property in PZT at the morphotropic phase boundary (MPB) as it appears only at the MPB in PZT [27,28].

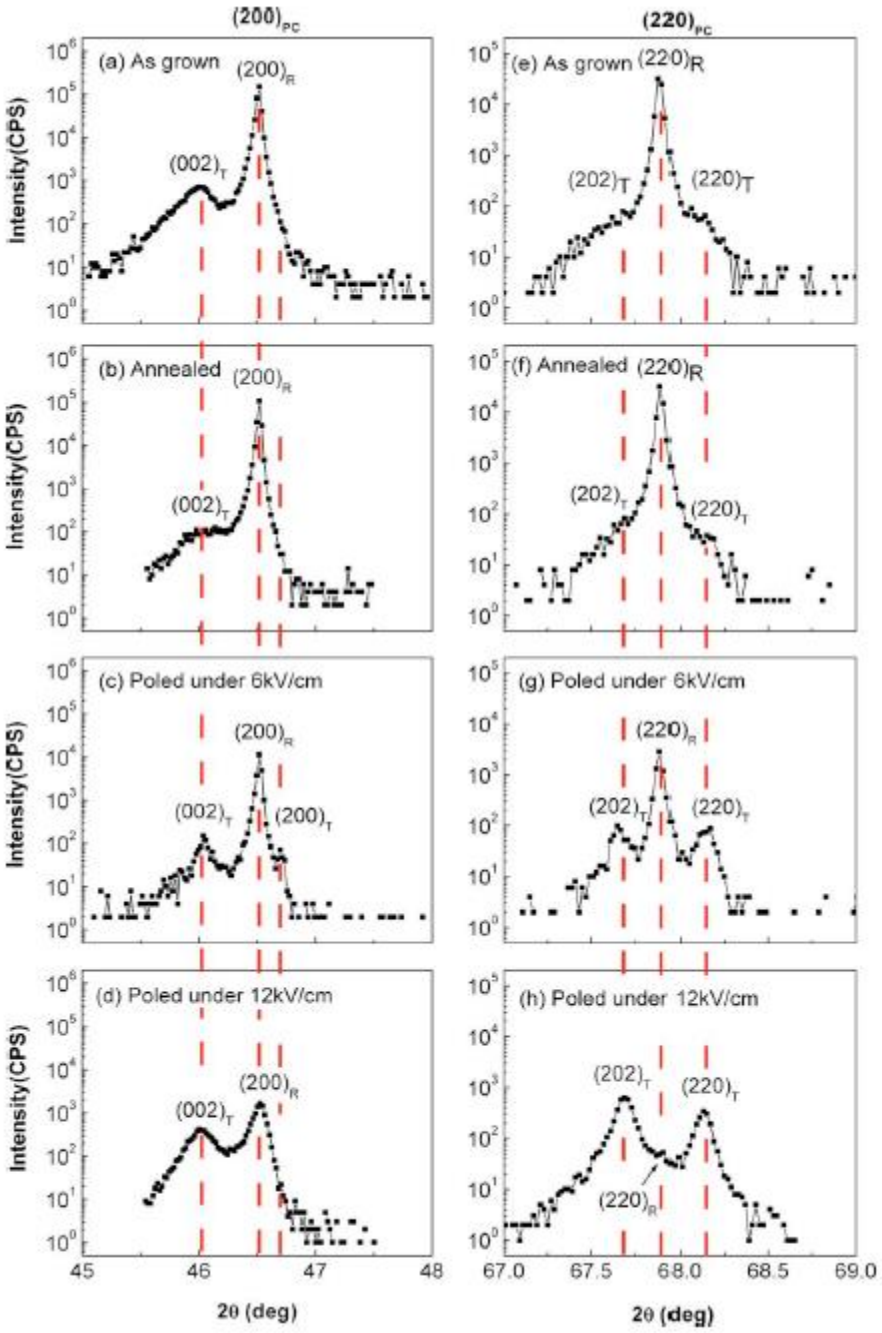

Figure 1.8. Electric field dependence of X-ray diffraction patterns near pseudo cubic (200) peak and (220) peak in $Na_{0.5}Bi_{0.5}TiO_3$-$BaTiO_3$ single crystal. (Figure sourced from [24])

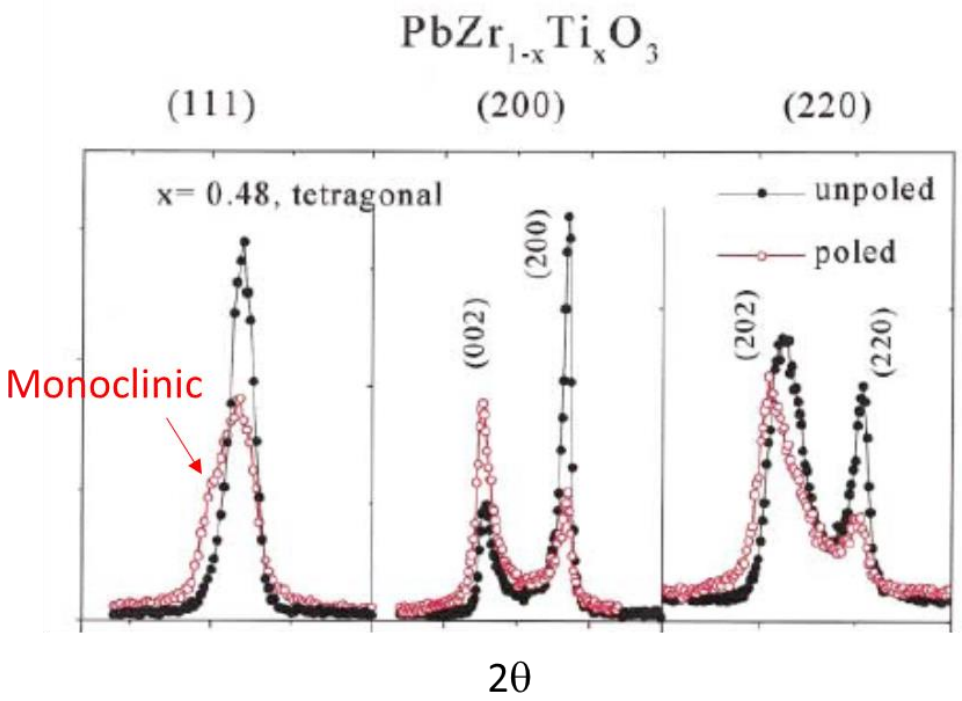

Figure 1.9. X-ray diffraction patterns near pseudo cubic (111), (200) and (220) peaks before and after poling in PZT ceramics. (Figure sourced from [27])

1.3 Microstructure Effects in Polycrystalline Ferroelectrics

Polycrystalline ferroelectrics are more practical than single crystal form materials because of the fabrication cost and process simplicity. In polycrystalline ferroelectrics, microstructure effects on the properties discussed above need to be considered. For example, a texture affects the macroscopic electric field induced strain due to the anisotropic piezoelectric coefficients, and highly textured ceramics exhibit a large electromechanical property [29,30]. Other than that, it is known that grain size influences the spontaneous polarization and electromechanical property. Moreover, residual stress/strain caused by an intergranular couple may contribute to both the electromechanical property and ferroelectric/ferroelastic switching behavior. Here, effects of the grain size and residual stress/strain due to an intergranular couple are discussed.

1.3.1 Grain Size Effect

It is known that the electromechanical properties abruptly decreases in a grain smaller than 1 μm in $BaTiO_3$ and PZT ceramics [31–33]. Figure 1.10 shows the macroscopically observed effective piezoelectric coefficients d_{33} and d_{31} (note that they are not the intrinsic material

properties discussed in chapter 1.2.1) as a function of grain size in PZT [31]. The origin was interpreted as several candidates such as ferroelastic domain wall motion suppression [31,34], tetragonality degradation [35] and effective volume decrease due to dead layers (grain boundary and domain boundary) [32,35]. An experimental evidence via in-situ X-ray diffraction technique suggests that ferroelastic domain wall motion is suppressed in a smaller grain [34], although the microscopic origin of this is still unclear due to the large probe size of the X-ray diffraction compared to the microstructure scale. A further detailed examination to understand the microscopic origin of the size effect is discussed in chapter 2.

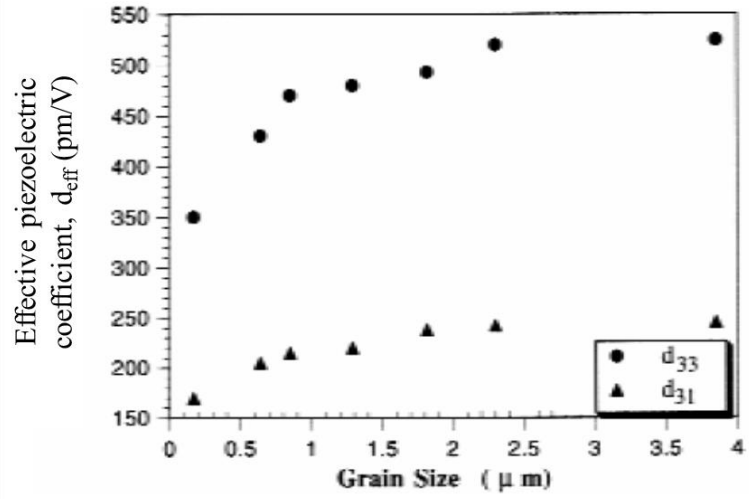

Figure 1.10. Effective piezoelectric coefficients as a function of grain size in PZT ceramics. (Figure sourced from [31])

1.3.2 Residual Stress/Strain Effect

The elastic stress/strain affects the piezoelectric property [36,37] and spontaneous polarization [37] due to the electromechanical coupling nature in ferroelectrics. In polycrystalline ferroelectrics, residual stress/strain may naturally occur in grains due to inhomogeneities of stress-free strains across grain boundaries [38]. These stress-free strains in ferroelectrics can be anisotropic strains such as thermal expansion, phase transformation and piezoelectric strain, thereby causing the strain inhomogeneities across grain boundaries due to misorientation. Indeed, experimental result of a distributed polar axis strains ε_{33} in a grain was reported [39]. Detailed analysis of the possible residual strain/stress is addressed in chapter 1.4.

This elastic stress/strain distribution influences the properties of polycrystalline ferroelectrics. Figure 1.11 shows the effective out-of-plane piezoelectric coefficient as a function of the amplitude of an applied drive electric field, and each component constituting the effective piezoelectric coefficient was identified via in-situ X-ray diffraction [40]. The lattice strain usually thought of as a piezoelectric strain can be divided into the constant component (green) and field dependent component (red). As discussed in chapter 1.2, a piezoelectric strain has a linear relationship to an electric field, so that the piezoelectric coefficient is constant about the electric field. Therefore, this field dependent component in the lattice strain is considered originating from elastic strains caused by intergranular coupling [40], namely piezoelectric strains depending on grain orientation cause the elastic strains in grains for maintaining the grain boundary compatibility.

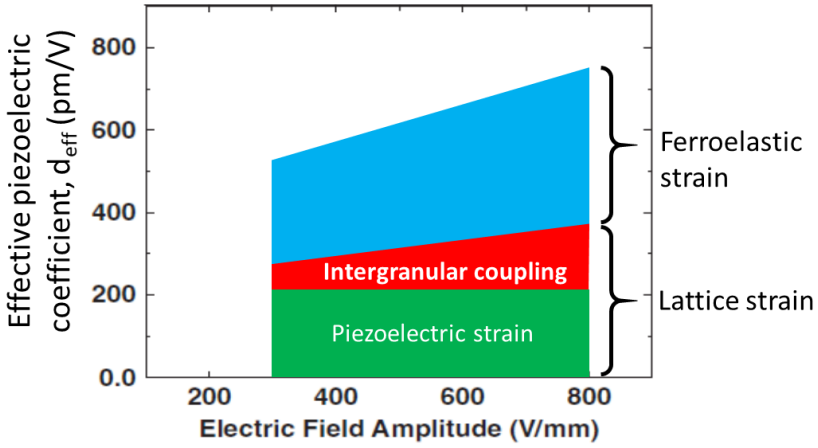

Figure 1.11. Effective piezoelectric coefficient and constituting components as a function of applied electric field amplitude in PZT ceramics. (Figure sourced from [40])

The strain distribution in a grain also effects the ferroelectric switching behavior. Figure 1.12 shows the simulated and experimental piezoelectric hysteresis loops in various positions in a grain in a PZT thin film [41]. The coercive field for ferroelectric switching varies depending on the positions in the simulation and experiment results, which are attributed to the residual strain distribution in a grain in the thin film [41].

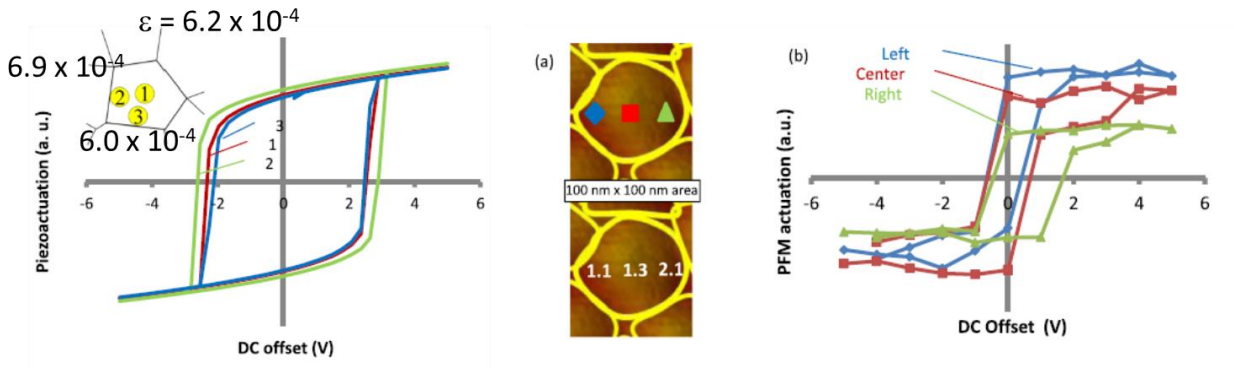

Figure 1.12. Simulation and experiment results of polarization switching hysteresis loops at a various position in a grain in polycrystalline PZT film (Figure sourced from [41]).

1.4 Residual Stress/Strain in Polycrystalline Piezoelectric Material

For analytical investigation of the residual stress/strain in a polycrystalline material, Eshelby's inclusion model can be employed [42,43]. A grain of interest is regarded as the inclusion and neighboring grains are the matrix surrounding the inclusion. Figure 1.13 shows a schematic drawing of the model. As these grains are comprised of a same material, a same elastic constant for all the grains is assumed for simplification here. Then, the grain of interest is subjected to uniform stress-free strains such as thermal expansion, phase transformation and piezoelectric strain. If there is no constraint to the grain, no elastic strain or stress arises. However, due to the neighboring matrix, the elastic strain and stress occur as the grain should fit the space initially occupied by itself to keep the grain boundary compatibility. The constrained strain and stress can be thought of as the residual strain and stress caused by the inhomogeneous stress-free strains across the grain boundary. Eshelby found the linear relationship between the constrained strain, ε^c_{kl} and stress-free strain to the inclusion, ε^*_{mn}, namely [42],

$$\varepsilon^c_{kl} = S_{klmn}\varepsilon^*_{mn} \tag{1.23}$$

where S_{klmn} is the Eshelby's tensor. Note that the equation is written in Einstein summation notation [6]. The stress associated with the constrained strain can be expressed as [42],

$$\sigma_{ij} = c_{ijkl}\varepsilon^e_{kl} = c_{ijkl}(S_{klmn}\varepsilon^*_{mn} - \varepsilon^*_{kl}) = c_{ijkl}(S_{klmn} - \delta_{kn}\delta_{lm})\varepsilon^*_{mn} \tag{1.24}$$

where ε^e_{kl} is the elastic strain tensor, c_{ijkl} is the stiffness tensor and δ_{ij} is the Kronecker delta. The elastic strain tensor is the subtraction of the stress-free strain, ε^*_{kl} from the constrained strain, ε^c_{kl}. Eshelby also discovered that the Eshelby's tensor was independent on the position when the inclusion is an ellipsoid, i. e. the constrained strain ε^c_{kl} is uniform throughout the grain [42]. The

explicit expressions of the Eshelby's tensor in the ellipsoidal inclusion can be found elsewhere [44]. From the explicit Eshelby's tensor and the assumed stress-free strain, one can get the constrained strain and stress state in the ellipsoidal inclusion. In other words, in a non-ellipsoidal real grain, determining Eshelby's tensor, which is a function of position, is much more complicated. In fact, a strain distribution observed experimentally in a $BaTiO_3$ grain exhibited non-uniform strains throughout the grain [39]. Nevertheless, it is an important insight that the constrained strain and stress linearly relate to the stress-free strain which the inclusion undergoes.

Deeg extended the Eshelby's work to piezoelectric materials using the electromechanical coupling equations (equation (1.12) and (1.13)) [45]. To consider the electromechanical coupling simultaneously, special matrixes using a notation introduced by Barnett [46] are convenient. First, the stress – electric displacement matrix, Σ_{iJ} is defined as[45],

$$\Sigma_{iJ} = \begin{cases} \sigma_{ij}, & J = 1,2,3 \\ D_i, & J = 4 \end{cases} \tag{1.25}$$

where D_i is the electric displacement. Normally, a suffix varies from 1 to 3 corresponding to the axis directions, while the capital suffix J can range from 1 to 4 in this notation [46]. Note that this matrix is not a tensor. Similarly, the strain – electric field matrix, Z_{Kl} is defined as [45],

$$Z_{Kl} = \begin{cases} \varepsilon_{kl}, & K = 1,2,3 \\ E_l, & K = 4 \end{cases} \tag{1.26}$$

As an analogy to the Eshelby's result, it was found that the constrained strain – electric field, Z^c_{Kl} and the uniform stress and electric displacement free strain, Z^*_{Mn} in the inclusion have a linear relationship, namely [45],

$$Z^c_{Kl} = S'_{KlMn} Z^*_{Mn} \tag{1.27}$$

where S'_{KlMn} is the Eshelby's tensor like matrix extended for a piezoelectric material. The stress – electric displacement state associated with the constrained strain – electric field matrix can be written as [45],

$$\Sigma_{iJ} = \Gamma_{iJKl}(S'_{KlMn} Z^*_{Mn} - Z^*_{Kl}) = \Gamma_{iJKl}(S'_{KlMn} - \delta_{KM}\delta_{ln}) Z^*_{Mn} \tag{1.28}$$

where Γ_{iJKl} is the electro – elastic constant matrix, which is defined as [45],

$$\Gamma_{iJKl} = \begin{cases} c_{ijkl}, & J,K = 1,2,3 \\ e_{lij}, & J = 1,2,3;\ K = 4 \\ e_{ikl}, & J = 4;\ K = 1,2,3 \\ -k_{il}, & J,K = 4 \end{cases} \tag{1.29}$$

In this definition, e_{lij} and e_{ikl} are the piezoelectric coefficient tensors in a different form from one in equation (1.20), and k_{il} is the permittivity tensor. The stress – electric displacement state in the inclusion linearly relates to the stress and electric displacement free strain and electric field which the inclusion undergoes, analogous to the Eshelby's result. The Eshelby's tensor like matrix extended for a piezoelectric material, S'_{KlMn} is uniform and independent on position in the inclusion if the inclusion is ellipsoidal. The explicit expressions of S'_{KlMn} in special cases can be found in previous reports [47–49].

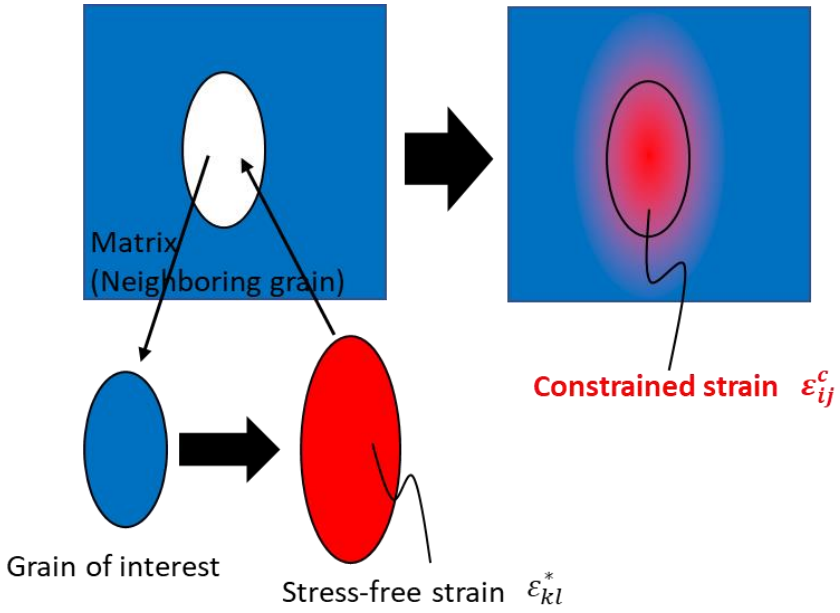

Figure 1.13. Schematic image of Eshelby's inclusion model.

2. ORIGIN OF GRAIN SIZE EFFECTS ON VOLTAGE DRIVEN FERROELASTIC DOMAIN EVOLUTION IN POLYCRYSTALLINE TETRAGONAL LEAD ZIRCONATE TITANATE THIN FILM

A portion of this chapter is a reprint, with journal permission, of a previous publication in Advanced Functional Materials [50], DOI: 10.1002/adfm.201909100.

2.1 Introduction

Microstructure effects on piezoelectric response are one of the most important but complicated topics in polycrystalline ferroelectrics. The texture of polycrystalline ceramics directly affects the piezoelectric response [29,51] and contributes to residual strains due to the thermal expansion anisotropy of the materials [37,40] as well as the ferroelectric switching behavior [41,52]. Among these microstructure parameters, grain size is an important parameter in determining the piezoelectric response.

Many experimental studies on the effect of grain size on properties have been reported in ferroelectric polycrystalline ceramics [31,32,35,51]. These papers consistently report that the piezoelectric response drastically decreased for an average grain size < 1 μm for typical ferroelectric materials ($Pb(Zr,Ti)O_3$ (PZT) or $BaTiO_3$). The suggested origin was the degradation of ferroelectricity [35], dead layers at the vicinity of grain boundaries [35] and domain walls [32] and the suppression of ferroelastic domain wall motion due to the domain pinning at grain boundaries [31]. Recently, in-situ XRD results showed that less ferroelastic domain wall motion occurred at a grain size of 0.3 μm compared to a grain size of 2 μm in $BaTiO_3$ [34]. However, it was not possible to determine the origin of the reduced ferroelastic domain wall motion in sub-micrometer grains due to the spatial resolution of the XRD technique. Marincel et al reported that a single grain boundary pinned domain walls in a bicrystal of PZT [53]. It is likely that grain boundaries act as pinning sites for ferroelastic domain wall motion in polycrystalline ferroelectrics, but the correlation between the local domain wall motion and grain size has not been directly observed. Identifying the exact nature of the grain size effect on ferroelastic domain wall motion will provide insight for microstructure design to enhance the effective piezoelectric response in polycrystalline ferroelectrics.

In this study, the nature of the grain size effect on ferroelastic domain wall motion with direct evidence of the correlation between ferroelastic domain wall motion and domain structure in a polycrystalline ferroelectric material is presented. The polycrystalline sample is a 300 nm thick $Pb(Zr_{0.4}Ti_{0.6})O_3$ film (*4mm*, tetragonal). The grain size, domain structures and in-situ domain evolution with applied DC voltage are locally investigated by piezoresponse force microscopy (PFM) [54] to relate domain wall motion to the grain size and domain structure.

2.2 Experimental

2.2.1 Sample Preparation and Crystal Phase

The 300 nm thick polycrystalline $Pb(Zr_{0.4}Ti_{0.6})O_3$ thin film was deposited on a $(111)Pt/TiO_2/SiO_2/(100)Si$ substrate by a chemical solution deposition method. The starting materials were $(CH_3COO)_2Pb\text{-}3H_2O$, $Ti(O\ n\text{-}C_4H_9)_4$ and $Zr(O\ i\text{-}C_3H_7)_4$. A solution in 2-methocyethanol was deposited on the substrate by spin coating. After the coating, heat treatments at 150 ^oC and 400 ^oC for 1 min each in air were performed for drying and pyrolysis. For crystallization, the film was annealed at 650 ^oC for 5 min in air by rapid thermal annealing. X-ray diffraction pattern shows that the film has a single perovskite phase without secondary crystalline phases as seen in Figure 2.1a. The perovskite (100)/(001) peak split represents the crystal tetragonal symmetry as expected. From the intensities of each peak, the film has (100)/(001) preferred out-of-plane orientation since the XRD peak intensities in random oriented PZT are {110} > (111) > {100} diffractions from a powder XRD pattern data [55]. The out-of-plane orientation map derived from electric backscattering diffraction (EBSD) supports the (100)/(001) preferred orientation in the film as shown in Figure 2.1b. The dominate green region shows the orientation that the 100 pole direction aligns to the out-of-plane direction, and the red region within the green grain exhibits the orientation that the 001 pole direction aligns to the out-of-plane direction. Some purple without any out-of-plane variants in a grain represents the orientation that the 111 pole direction aligns to the out-of-plane direction, which is seen as a small peak in the XRD pattern.

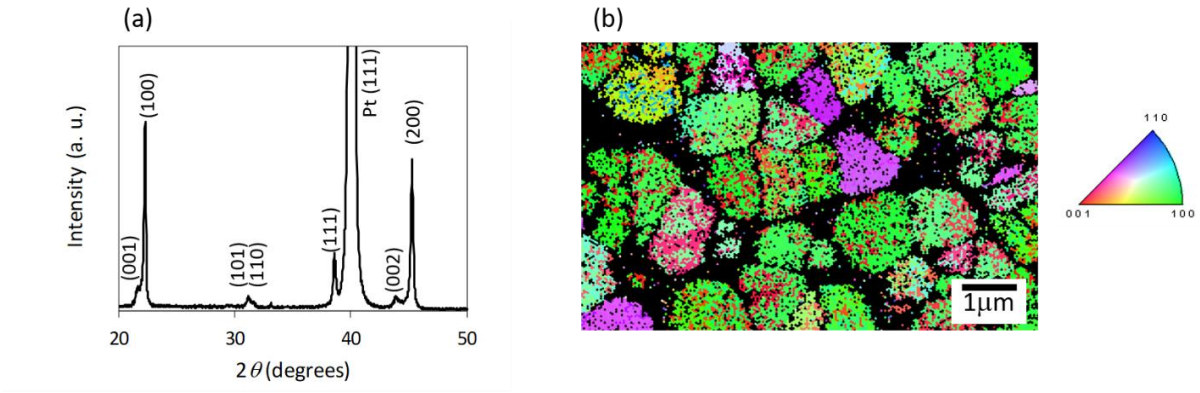

Figure 2.1. (a)XRD pattern and (b)out-of-plane orientation map for polycrystalline PZT film.

2.2.2 Piezoelectric Response Force Microscopy (PFM)

The principle of PFM is schematically shown in Figure 2.2 [56]. An AC voltage from a function generator is applied to a piezoelectric sample through a conductive atomic force microscopy (AFM) tip. The cantilever with the tip deflects in accordance with displacements by the piezoelectric response induced by the AC voltage as well as a topographic feature during surface scanning (normal AFM use). This cantilever deflections are detected using laser reflection from the cantilever and a photodiode laser position sensor. Now, the laser position information on the photodiode involves the piezoelectric response and the surface topography. To extract the piezoelectric response, a lock-in amplifier is utilized as the frequency of the piezoelectric vibration is known (same as the applied AC voltage). For the topographic data, a feedback loop intending to move back to the set point position on the photodiode controls the tip-sample distance, so that the height movement in this process provides the actual topographic height, which is nothing but the ordinary AFM procedure. In the end, PFM and topographic images can be obtained simultaneously.

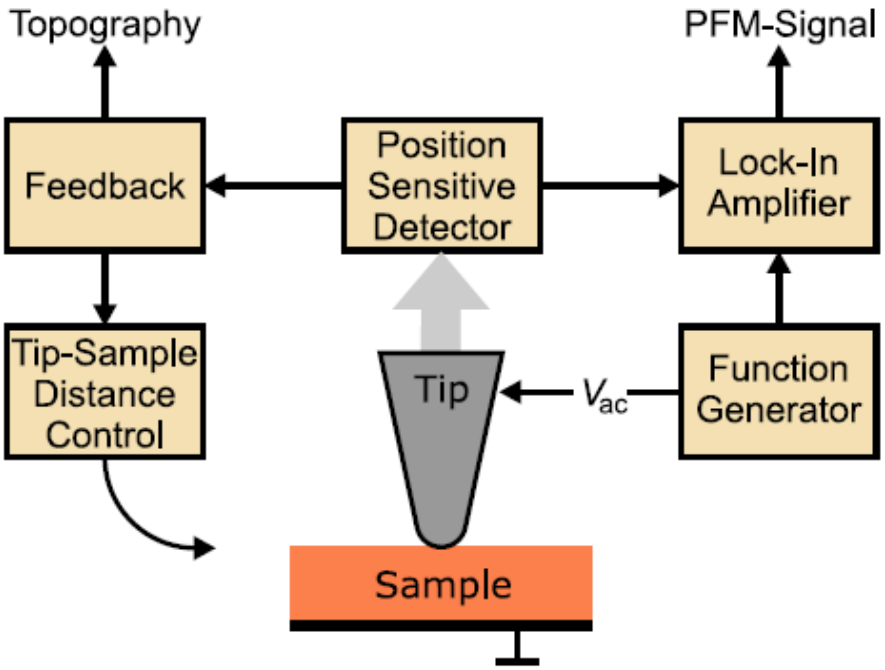

Figure 2.2. Schematic diagram of principle of PFM. (Image sourced from [56])

The PFM data includes two components: amplitude and phase, as the deflection is the AC signal. Figure 2.3 shows the PFM signal in a time domain. The amplitude of the piezoelectric response depends on the orientation of the grain or domain. As discussed in chapter 1.2, the piezoelectric response is an anisotropic property determined by the crystal symmetry. For instance, in a *4mm* crystal, an out-of-plane (001) oriented domain has a clear piezoelectric strain associated with a d_{333} coefficient whereas a (100) oriented domain theoretically shows no out-of-plane response as $d_{111} = 0$ [6]. Note that the suffix is written in the crystal frame, namely the out-of-plane direction for the (100) oriented domain is x_1. Thus, the electric field direction from the tip to the bottom electrode is E_1, and the normal strain along the out-of-plane direction is ε_{11} for the (100) oriented domain. The phase signal represents whether the polarization direction directs upward or downward as shown in Figure 2.3. A positive applied voltage from the bottom to top electrodes induced an out of plain tensile strain (blue line, in phase), no matter where the polarization directs in the upper hemisphere. On the other hand, a negative voltage from the bottom to top induces an out of plain tensile strain (orange line, out of phase) in a domain with downward polarization. Thus, 180^o phase difference appears between the two states.

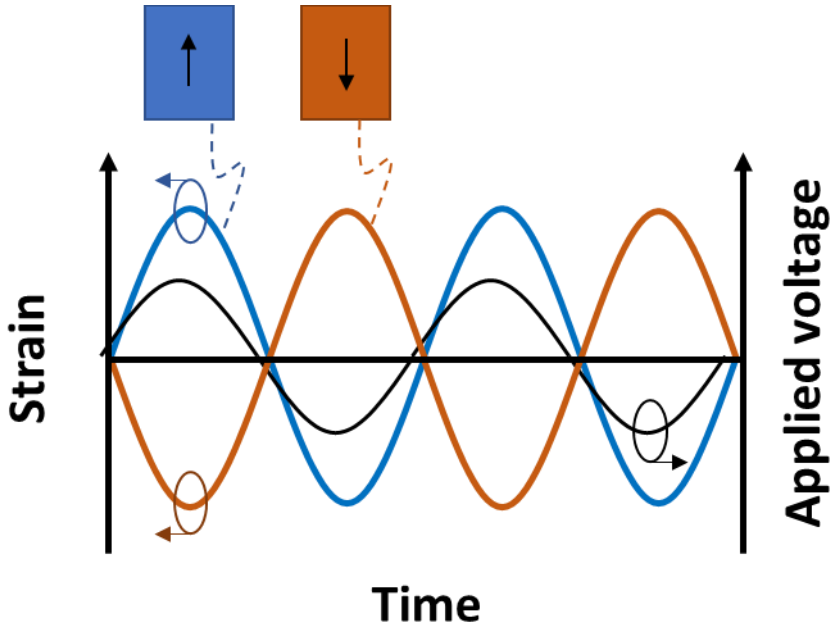

Figure 2.3. PFM signal and applied AC voltage in time domain.

Beyond the out-of-plane displacement measurement, one can measure in-plane displacement with a torsion deflection of the cantilever (called lateral PFM), so that 2D and 3D vectoral polarization direction can be analyzed [57–59]. In a *4mm* crystal, an out-of-plane (100) oriented domain has a shear displacement due to the non-zero d_{113} piezoelectric coefficient. That shear displacement causes a torsion deflection of the cantilever, whose direction depends on in-plane orientation of the domain.

For our PFM measurement, an AC voltage (4 V peak to peak at 4.5 kHz) superimposed with a DC voltage (0 to 9 V) was applied through a conductive AFM tip to excite piezoelectric vibration and drive ferroelastic domain wall motion. Only out-of-plane PFM was employed since the purpose of the study is distinguishing the (100) and (001) domains to observe ferroelastic domain walls. A region of the film was initially poled via AFM scanning with +9 V_{DC} (30 MV m^{-1}) to eliminate ferroelectric domain walls.

2.3 Results and Discussion

Figure 2.4 shows the topography and out-of-plane PFM images taken simultaneously after the 9 V_{DC} poling. No DC voltage was applied during the measurement. Smooth and well-defined

grains (~0.5 to 2 μm in diameter) were observed from the topography shown in Figure 2.4a. The out-of-plane PFM amplitude image exhibited clear ferroelastic (90°) domain structures in the grains as shown in Figure 2.4b. No ferroelectric (180°) domain structure was observed since the out-of-plane PFM phase image had no contrast (Figure 2.4c) after the poling process. The noisy regions in the PFM phase image are an amorphous phase (based on lack of piezoelectric response and no secondary phase from XRD). The dark and bright regions in the PFM amplitude correspond to (100) and (001) domains oriented towards the surface normal based on their anisotropic piezoelectric response as a (100) oriented domain does not show out-of-plane normal strain for an electric field in the normal direction for a *4mm* crystal. As the film has a (100)/(001) preferred orientation this contrast is from (100)/(001) ferroelastic domains.

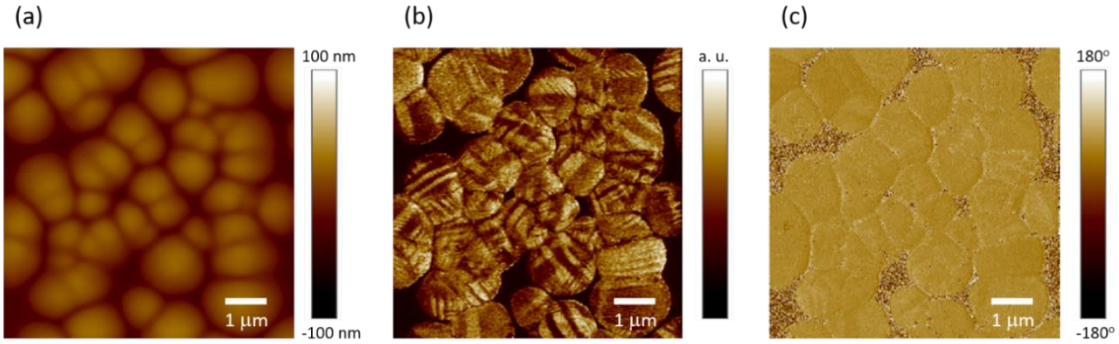

Figure 2.4. PFM results for polycrystalline PZT film after poling. (a) Topography, (b) out-of-plane PFM amplitude image and (c) out-of-plane PFM phase image. The images were taken simultaneously.

To investigate ferroelastic domain evolution induced by an applied voltage, a DC voltage up to 9 V_{DC} was superimposed through the AFM tip while acquiring out-of-plane PFM amplitude images. Figure 2.5 shows the analysis procedure. Figure 2.5a is the PFM amplitude images of an arbitrary grain at 0 V_{DC} and 7 V_{DC}. The (001) out-of-plane oriented domains expansion attributed to the DC voltage is seen (red and blue arrows). The domain width is plotted as a function of the applied DC voltage in Figure 2.5b. The red diamond is the width of the (001) domain pointed out by the red arrow whereas the blue square is the width of the (001) domain pointed out by the blue arrow in Figure 2.5a, and they increase with the applied DC voltage increase. To compare the domain width increase rate, the normalized domain widths with respect to the domain width at 0 V_{DC}, w/w_{0V}, are plotted in Figure 2.5c. Both the domains expand up to 1.4 at 9 V_{DC} compared to the width at 0 V_{DC}.

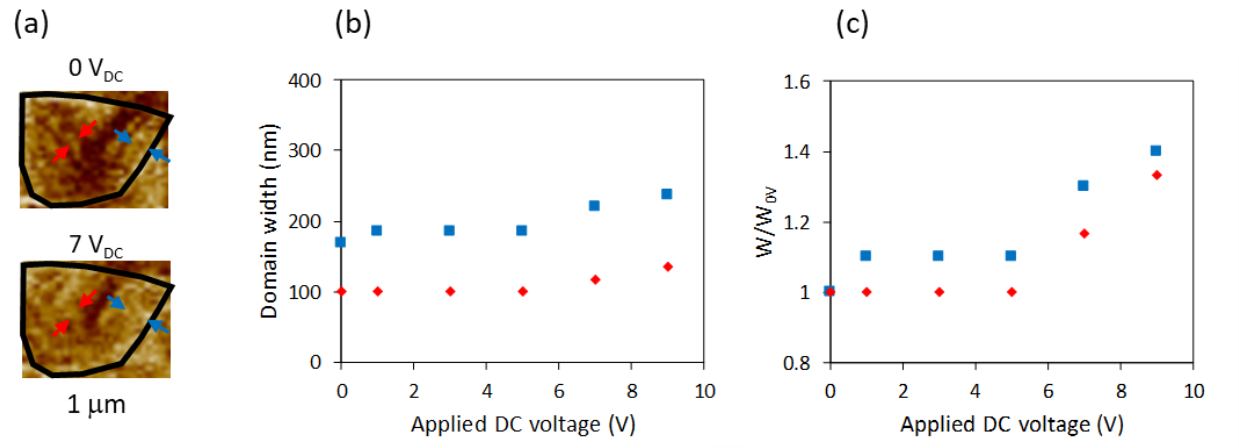

Figure 2.5. Domain width analysis with respect to applied DC voltage. (a) PFM amplitude images with 0 and 7 V_{DC} at a grain (b) Domain width of two selected (001) oriented domains (red and blue arrows) as a function of applied DC voltages for the grain. (c) Normalized domain widths as a function of applied DC voltages for the grain.

To obtain the domain evolution data from a wide range of grain size, a DC voltage up to 9 V_{DC} was superimposed through the AFM tip while acquiring out-of-plane 7 µm square PFM amplitude images as shown in Figure 2.6. From the contrast evolution in these images the fraction of the out-of-plane (100) oriented domains and (001) oriented domains changes depending on the DC voltage, and at higher DC voltage there are more out-of-plane (001) oriented domains. From these images, the normalized domain widths, w/w_{0V} of the (001) oriented domains were extracted and plotted as a function of the DC voltage as shown in Figure 2.6b. The data (blue squares, red diamonds and black triangles) in each figure are the widths of three arbitrarily selected domains in the four grains i, ii, iii and iv marked in Figure 2.6a. Insets in each figure show the PFM amplitude images at 0 V_{DC} and 9 V_{DC} of the focused grains. The grains i, ii and iii exhibited (001) domain width increasing up to 1.4 of the domain width at 0 V_{DC} with increasing the applied DC voltage. The (001) domain expansion are also seen in the inset images. On the contrary, grain iv did not show significant domain width increase with respect to the applied DC voltage.

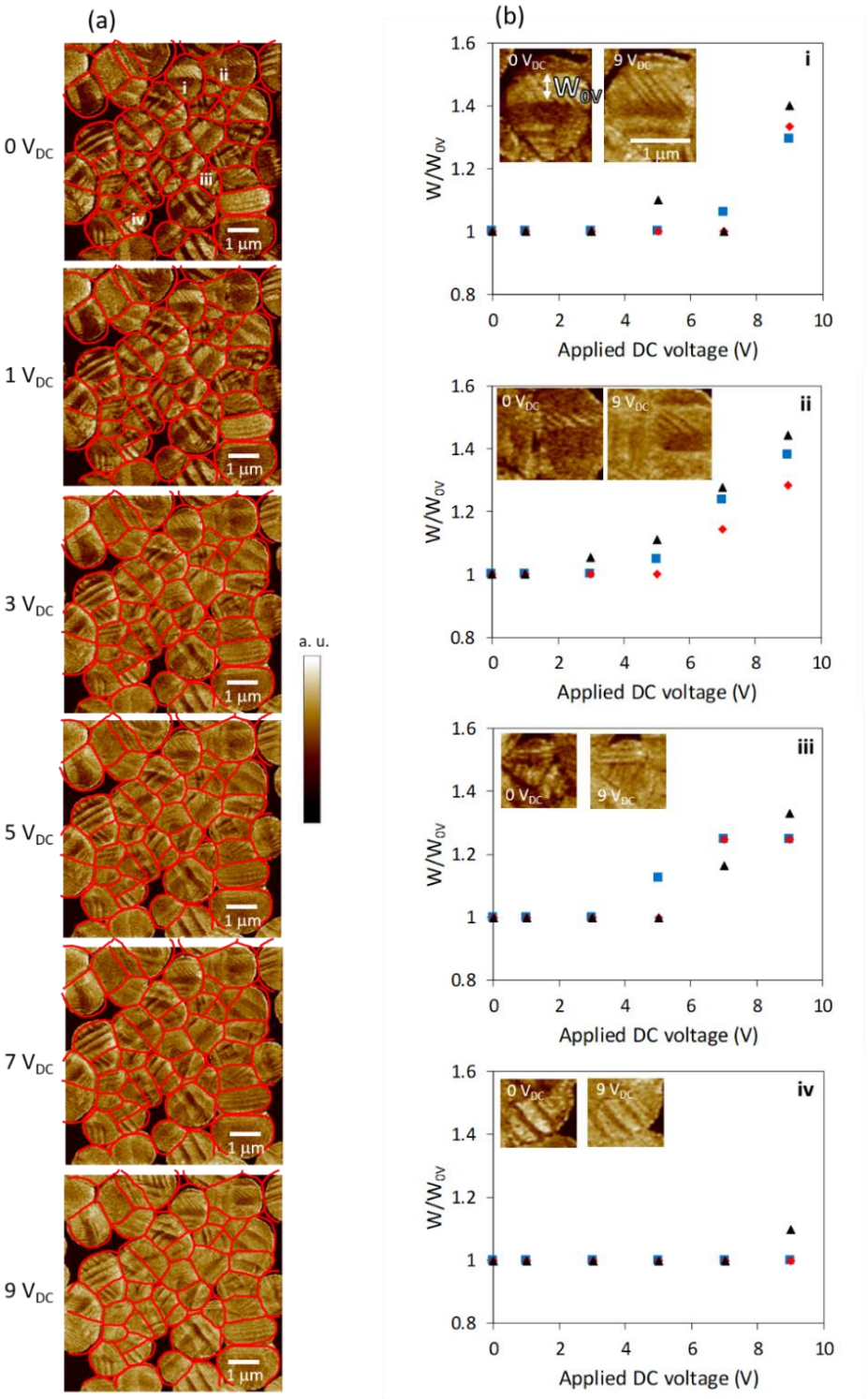

Figure 2.6. Domain evolution with respect to applied step-up DC voltage. (a) PFM amplitude images with 0, 1, 3, 5, 7 and 9 V_{DC}. (b) Normalized (001) oriented domain width as a function of applied DC voltages for arbitrarily selected four grains i, ii, iii and iv. Domain widths were extracted from three domains in each grain. Insets show PFM amplitude image of focused grains at 0 V_{DC} and 9 V_{DC}.

The domain evolution for voltage cycling (0 – 9 – 0 V) was investigated to determine the reversibility of domain wall motion. Figure 2.7 shows the average normalized (001) oriented domain width for sixteen arbitrary grains, chosen as they showed relatively clear domain structures. The dark squares (black) show the domain evolution for increasing voltage while the light (red) triangles are for decreasing voltages. The (001) oriented domain width increment was the same showing that ferroelastic domain wall motion in this voltage range is reversible. This reversibility implies that the observed ferroelastic domain wall motion directly contributes to non-linearity in the piezoelectric response. There is no hysteresis in domain width for changing voltage. This is expected from a unipolar strain curve since the hysteresis was believed to be from ferroelastic domain wall motion [60,61]. Tsurumi *et al* showed no hysteresis in (200)/(002) XRD peak intensity evolution with applied electric fields even in a tetragonal PZT whose strain curve exhibited hysteresis [60]. The results reported here are related to the ferroelastic domain volume fraction and thus comparing to XRD intensity evolution rather than the strain curve is appropriate. The origin of the lack of hysteresis in the ferroelastic domain switching volume fraction is unclear, but it is likely due to domain evolution kinetics [60]. The acquisition time for the different measurements is quite different. The strain curve was acquired in 110 seconds whereas in-situ XRD took 110 minutes [60] and PFM in this study took 170 minutes for a cycle.

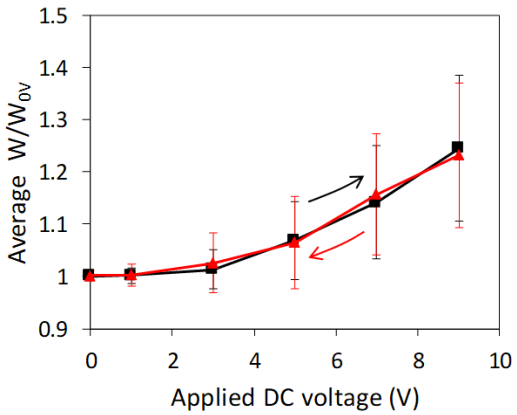

Figure 2.7. Average normalized (001) oriented domain width as a function of step-up and step-down applied DC voltage. Black squares represent domain width evolution with step-up voltages whereas red triangles show that with step-down voltages. Error bars represent standard deviations of domain widths of all studied grains.

The ferroelastic domain wall motion is also able to be seen by the polarization increase due to an applied voltage as the fraction of the out-of-plane (001) oriented domains increases. Figure

2.8 shows the polarization – voltage (*P* - *V*) relationship. The polarization was measured using a Au/PZT/Pt capacitor structure with a ϕ100 μm Au top electrode. The *P* - *V* loop taken after poling shows clear hysteresis whose coercive voltage is 3 V as shown in Figure 2.8a. From this hysteresis loop, the remanent polarization with applied voltages was extracted (Figure 2.8b). The remanent polarization gradually increases as the voltage increases even beyond the ferroelectric coercive voltage: 0.17 C m^{-2} at 5 V to 0.21 C m^{-2} at 10 V. This polarization increment is comparable to the 1.2 times (001) domain width expansion shown in Figure 2.7. Moreover, the threshold voltage for the ferroelastic domain wall motion is also compatible in these PFM and *P* - *V* loop results. The significant ferroelastic domain wall motion started at 3 V in PFM measurements (Figure 2.7), and the gradual polarization increase also started from right after reaching the coercive voltage. Thus, it is most likely that the gradual polarization increase indicates the ferroelastic domain wall motion observed in PFM. It is known that the remanent polarization increase with applied voltages can also be due to the leakage current contribution [62,63]. However, the clear hysteresis loop without rounded shape and the small leakage current (< 1 A m^{-2} at 10 V, shown in Figure 2.9) imply that the leakage current contribution to saturation is limited in this film.

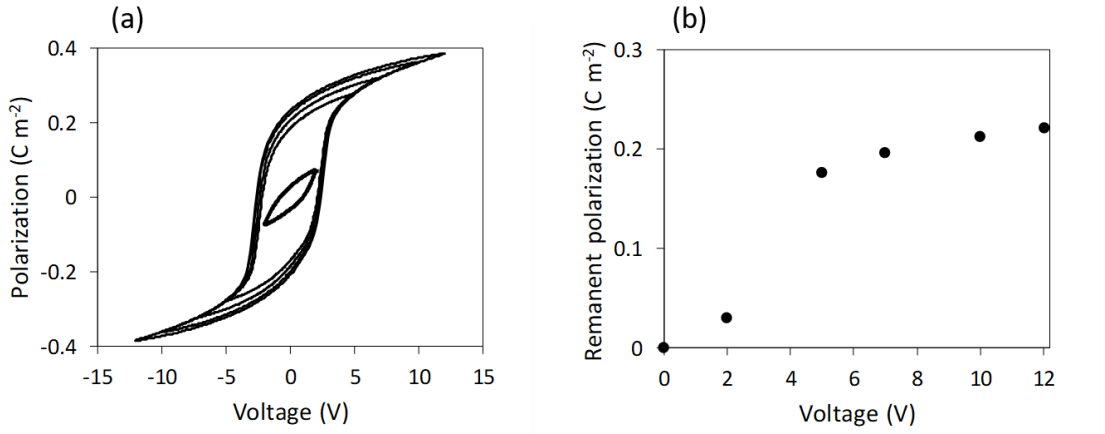

Figure 2.8. Polarization – voltage relationship using a Au/PZT/Pt capacitor structure with a ϕ100 μm Au top electrode. (a) Polarization – voltage hysteresis loop after 9 V_{DC} poling. (b) Remanent polarization as a function of applied sweep voltages.

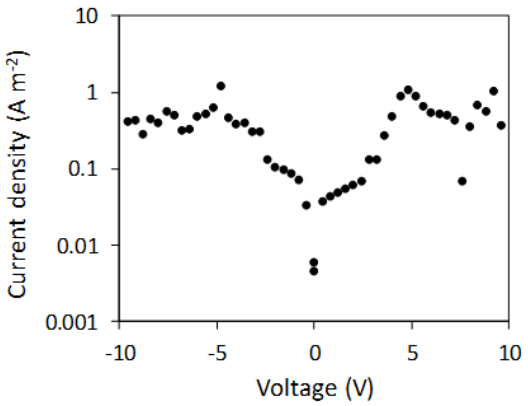

Figure 2.9. Current density – voltage curve measured with an Au/PZT/Pt capacitor structure with a ϕ100 μm Au top electrode.

The domain structure within the grains was observed to vary. It was reported that the domain structure in a large grain tends to split into several variants [64,65], here called colonies. These colonies in a grain were also observed in these results. Figure 2.10a shows regions of the PFM amplitude of grains from Figure 2.4 and schematics of the domain structures. The dark (brown) region in the schematics represents (100) oriented domains and the light (yellow) region shows (001) oriented domains. Some grains have a single colony and in other grains the domain structure has two and more colonies. Figure 2.10b shows the correlation between grain size and the number of colonies in the grains. The grain size is the equivalent area diameter. The grains for these plots were the arbitrarily chosen sixteen grains (2-5 grains for each colony group). The error bars are the standard deviation of the grain diameter for each colony group. There is a significant tendency that smaller grains have fewer colonies, which is in agreement with a previously reported study [65]. However, this correlation is not perfect as the range of the error bars implies. Indeed, the single colony grain in Figure 2.10a is larger than the two and three colony grains. Hence, grain size is not the only parameter to determine the colony structure. It is likely that the residual strain in a grain should also be an important parameter for controlling the colony structure since the origin of the colony structure is the relaxation of the residual strains due to anisotropic properties of the elasticity, phase transformation strains across the Curie temperature, and thermal strains. Figure 2.10c shows the normalized (001) domain width at 9 V_{DC} (w_{9V}/w_{0V}) for each grain with respect to the number of colonies. The grains for these plots were the arbitrarily chosen sixteen. The error bars are the standard deviation of the normalized domain width. A clear reduction in

domain wall motion is seen in the single colony grains. All the single colony grains exhibited limited (001) domain expansion at 9 V_{DC} (less than 1.1) whereas the multi-colony grains showed the significant domain expansion (1.2-1.3). The number of colonies, especially single or multi, plays a dominant role in determining the degree of domain wall motion. This result is the first direct evidence that a single colony domain structure suppressed the ferroelastic domain wall motion in a grain, which supports domain pinning by grain boundaries as predicted [31]. Both edges of ferroelastic domains in a single colony grain must intersect grain boundaries whereas in a multi-colony grain at least an edge of the ferroelastic domains will intersect a domain boundary. The domain pinning force at a domain boundary has not been investigated. However, based on these results, it is likely that the pinning force at a domain boundary is significantly smaller than that at a grain boundary. Moreover, the fact that domain motion was suppressed at a bicrystal grain boundary [53] also supports the domain pinning at grain boundaries in a single colony grain.

The normalized (001) oriented domain widths at 9 V_{DC} (w_{9V}/w_{0V}) for each grain were plotted as a function of the grain diameter (Figure 2.10d). The grains for these plots were the arbitrarily chosen sixteen grains. The error bars are the standard deviation of the normalized width of three domains in each grain. There is a decrease in ferroelastic domain wall motion at grains smaller than 1 μm, corresponding to the reported grain size at which effective piezoelectric response drastically decreases [31,32]. However, the correlation between grain size and domain width is not that clear. Half of grains less than 1 μm in diameter did not show considerable (001) domain expansion (width <1.1 at 9 V_{DC}) while the other half exhibited significant (001) domain expansion (1.2 -1.3 at 9 V_{DC}). In Figure 2.10d, the plot colors and shapes represent the number of colonies within the grains; open red squares represent the single colony grains, blue diamonds are for the two colony grains, green triangles are for the three colony grains and black circles are for the four colony grains. As expected from Figure 2.10c, single colony grains exhibit less ferroelastic domain wall motion than multi-colony grains. In addition to that, there was no significant size dependence for the grains having the same number of colonies. Hence, the observed grain size dependence on ferroelastic domain wall motion does not originate from an independent size effect, but from the number of colonies within a grain. This result implies that the number of colonies is a more significant controlling factor to determine ferroelastic domain wall motion in this size range (0.6 – 1.6 μm) than substrate clamping effect as a smaller grain has smaller film/substrate interface area, although significant hinderance of ferroelastic domain wall motion due to the substrate

clamping was reported [66]. The reason for the observed grain size effect in polycrystalline materials is due to the correlation of the grain size and number of colonies [65]. This correlation will dominate the effective piezoelectric response and there will be an apparent dependence of the piezoelectric response on grain size.

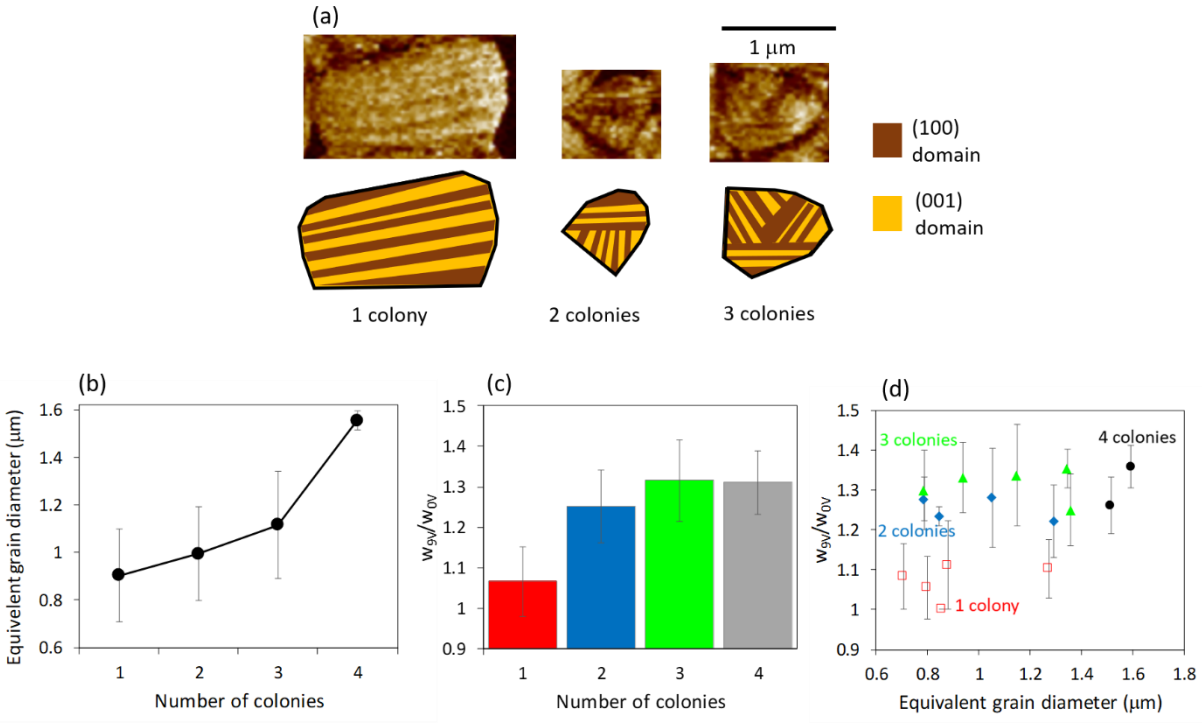

Figure 2.10. Colonies in grains and effect of number of colonies and grain size on ferroelastic domain evolution. (a) PFM images and schematics which show colony structure in a grain. (b) Equivelent grain diameter of arbitrary selected sixteen grains with respect to number of colonies in each grain. Error bars represent standard deviations of grain diameter for chosen grains. (c) (001) domain width at 9 V_{DC} normalized to that at 0 V_{DC} (w_{9V}/w_{0V}) for same grains with respect to number of colonies in each grain. Error bars represent standard deviations of normalized domain width for chosen grains. (d) (001) domain width at 9 V_{DC} normalized to that at 0 V_{DC} (w_{9V}/w_{0V}) for same grains as a function of equivalent grain diameter. Error bars represent standard deviations of normalized domain width in several domains in each grain.

2.4 Conclusion

The in-situ local ferroelastic domain evolution was measured as a function of the grain sizes via a PFM technique in a polycrystalline $Pb(Zr_{0.4}Ti_{0.6})O_3$ film. A reversible ferroelastic domain motion was observed with an applied DC voltage. This result means that the ferroelastic domain wall motion contributed to the macroscopic electric field induced strain. A polarization increase due to applied voltages larger than the coercive voltage was also observed, which supports

the ferroelastic domain wall motion with an applied DC voltage. Single colony grains did not show significant domain wall motion. Multi-colony grains exhibit domain wall motion but no dependence on grain size even in the grains less than 1 μm in diameter. This result is the first direct evidence of the correlation between the domain structure and ferroelastic domain wall motion. This evidence reinforces the hypothesis that ferroelastic domain pinning occurs at grain boundaries. Thus, the number of colonies in a grain plays a dominant role in determining ferroelastic domain wall motion.

3. STRESS-INDUCED METASTABLE PHASES AND FERROELASTIC SWITCHING MECHANISMS

3.1 Introduction

Electric field induced polarization responses in ferroelectrics are unique and wide ranging, such as ferroelectric switching, ferroelastic switching and polarization rotation (phase transformation). These responses play an important role not only in establishing the performance and degradation in electromechanical actuators and devices [67–69], but also in defining the physical couplings in multiferroic materials [70–72], and the performance in perovskite solar cells [73,74]. In the first two cases, the community has spent a great deal of effort to quantify the effect of the underlying multiphysical coupling on the desired engineered system [75].

Among them, the elastic energy contribution to the free energy landscape has a strong impact on these polarization responses, due to the electromechanical coupling and the natural tendency of the material system to minimize the total free energy [9,76]. Experiments and simulation results showed that strains tune ferroelectric switching behavior in tetragonal $Pb(Zr_{0.2}Ti_{0.8})O_3$ [41,52]. Due to the nature of ferroelasticity, mechanical loading directly contributes to ferroelastic switching volume, and hysteretic behavior in electric field induced ferroelastic switching [50,67,77,78]. Recently, in a $PbTiO_3$ thin film, a detailed analysis of biaxial epitaxial strain effects on the thermodynamically stable domain configuration and reversible ferroelastic switching was presented [69]. For the polarization rotation, it was reported that an electric or stress field induced phase transformation from tetragonal-like phase to rhombohedral-like phase in a specific biaxial strain condition for $BiFeO_3$ epitaxial thin films [79–81]. These polarization responses in ferroelastic switching and polarization rotation by external stimuli likely originated from the free energy degeneration between different ferroelastic domain configurations or different phases due to the biaxial epitaxial strains [69,82].

In polycrystalline materials, both ferroelastic switching and polarization rotation accompanying a low-symmetry phase induced by an applying electric field were observed in $Pb(Zr_{0.52}Ti_{0.48})O_3$, $BaTiO_3$ and $Bi_{0.5}Na_{0.5}TiO_3$ base ceramics [24–27,34]. It is believed that the polarization rotation is induced by an electric field along the polarization direction of the induced phase as observed in relaxor ferroelectrics [23,24]. In addition, ab initio calculation suggested that an electric field in the pseudo-cubic [111] direction induces a tetragonal – monoclinic –

rhombohedral phase transition cascade in a classic ferroelectric $Pb(Zr_{0.5}Ti_{0.5})O_3$ [83]. However, it is unclear what causes the difference in several low-symmetry phases especially in $BaTiO_3$ (M_C) and $Pb(Zr_{0.52}Ti_{0.48})O_3$ (M_A) phases. Moreover, in the well-studied $BaTiO_3$ system, the polarization rotation and low symmetry phase has not been observed when characterized in a single crystal at room temperature [26,84], although it is likely easy to achieve polarization rotation with an electric field along [111] or [101].

The missing factor to explain the unknown polarization rotation behavior in $Pb(Zr,Ti)O_3$ and $BaTiO_3$ ceramics can be the mechanical loading. Indeed, residual stress or strain caused by elastic contributions including anisotropic thermal and chemical expansion, phase transformation, and elastic properties was predicted and observed in polycrystalline materials [38,39]. In a mean field approximation, the residual stress state can be addressed using Eshelby's analytical investigation on an inclusion and its extension to piezoelectric materials by Deeg [42,45]. Deeg reported that elastic stress/strain states and electric displacement in an inclusion is a linear function of stress-free strains that the inclusion underwent, by introducing the extended Eshelby tensor [45]. The extended Eshelby tensor depends on the inclusion shape and is a function of position in the inclusion unless the inclusion is ellipsoidal. The possible stress-free strains in piezoelectric materials are phase transformation, thermal expansion and piezoelectric strain, thereby being ε_{11}, ε_{22}, ε_{33}, ε_{23}, ε_{13} in a 4mm crystal. Thus, the residual stress or strain distribution can be complicated in a real (non-ellipsoidal) grain as experimentally observed [39], and it is likely necessary to consider not only normal stress but also shear stress components to determine what exactly occurs for the polarization response in polycrystalline materials.

Here, we analytically demonstrate the impact of the six independent mechanical stress components on the electric field induced ferroelastic switching and on the stabilization of metastable low symmetry polarization states by combining the volumetric free energy landscape of the stress-free variants, and an analytical implementation of the gradient descent method [85]. For a representative volume element of material subjected to an homogeneous stress, σ, the Landau-Devonshire free energy density for tetragonal $Pb(Zr_{0.52}Ti_{0.48})O_3$ and $BaTiO_3$ single domain crystals [86] enables rationalization of the switching process, i.e., the details of the polarization path transition from an initial state along the *x*-axis to a final state along the *z*-axis with a constant electric field applied along the *z*-axis in this paper.

3.2 Model and Method

As discussed in chapter 1.1, the elastic Gibbs free energy density at the isothermal condition, g, is described as [86]

$$g(\{P_i\},\{\sigma_{ij}\};T) = a_{ij}P_iP_j + a_{ijkl}P_iP_jP_kP_l + a_{ijklmn}P_iP_jP_kP_lP_mP_n - P_iE_i - \frac{1}{2}s_{ijkl}\sigma_{ij}\sigma_{kl} - Q_{ijkl}\sigma_{ij}P_kP_l \quad (3.1)$$

where a_{ij}, a_{ijkl} and a_{ijklmn} are the Landau expansion coefficients at constant stress, s_{ijkl} is the elastic compliance tensor at constant polarization and Q_{ijkl} is the electrostrictive tensor. Material properties for PZT and $BaTiO_3$ are tabulated in Table 3.1 [10,87,88] [89,90]. Assumed is that the crystal is only subjected to the external homogeneous stress, σ_{ij}.

Table 3.1. Material properties used in the free energy density calculation.

Symbol	$Pb(Zr_{1-x}Ti_x)O_3$ [10,87,88]	$BaTiO_3$ [89,90]	Units
a_{11}	$(298-T_0)/(2\times8.85\times10^{-12}\times C_0)$	-2.772×10^7	J m C^{-2}
a_{1111}	$(10.612-22.655x+10.955x^2)\times10^{13}/C_0$	-6.476×10^8	J m^5 C^{-4}
a_{1122}	$[\{2.6213+0.42743x-(9.6+0.012501x)e^{-12.6x}\}\times10^{14}/C_0]/3-a_{1111}$	3.23×10^8	J m^5 C^{-4}
a_{111111}	$(12.026-17.296x+9.179x^2)\times10^{13}/C_0$	8.004×10^9	J m^9 C^{-6}
a_{111122}	$(4.2904-3.3754x+58.804e^{-29.397x})\times10^{14}/C_0$	4.47×10^9	J m^9 C^{-6}
a_{112233}	$\{0.887-0.76973x+(16.225-0.088651x)e^{-21.255x}\}\times10^{15}/C_0-3a_{111111}-6a_{111122}$	4.91×10^9	J m^9 C^{-6}
Q_{1111}	$0.029578/(1+200(x-0.5)^2)+0.042796x+0.045624$	0.110	m^4 C^{-2}
Q_{1122}	$-0.026568/(1+200(x-0.5)^2)-0.012093x-0.013368$	-0.045	m^4 C^{-2}
Q_{2323}	$0.025325/(1+200(x-0.5)^2)+0.020857x+0.046147$	0.029	m^4 C^{-2}
s_{1111}	$-1.6667x^5+6.5833x^4-10.317x^3+8.0192x^2-3.0942x+0.48306$	0.00747	10^{-9} m^2 N^{-1}
s_{1122}	$0.5833x^5-2.375x^4+3.8292x^3-3.0562x^2+1.2086x-0.1924$	-0.00295	10^{-9} m^2 N^{-1}
s_{2323}	$-3.9167x^5+15.083x^4-23.104x^3+17.624x^2-6.7361x+1.05846$	0.0184	10^{-9} m^2 N^{-1}

$T_0 = 462.63+843.4x-2105.5x^2+4041.8x^3-3828.3x^4+1337.8x^5$
$C_0 = \{2.8339/(1+126.56(x-0.5)^2)+1.4132\}\times10^5$

The ferroelastic switching path corresponds to the sequence of states in the direction of steepest descent [85], mathematically expressed as

$$-\nabla g = -\frac{\partial g}{\partial P_x}\mathbf{i} - \frac{\partial g}{\partial P_y}\mathbf{j} - \frac{\partial g}{\partial P_z}\mathbf{k} \tag{3.2}$$

so that, the streamline of the steepest descent path can be expressed as [91]

$$\frac{dP_x}{\frac{\partial g}{\partial P_x}} = \frac{dP_y}{\frac{\partial g}{\partial P_y}} = \frac{dP_z}{\frac{\partial g}{\partial P_z}} \tag{3.3}$$

for a representative ferroelectric volume with a uniform polarization state, in the absence of polarization, stress, or electric field heterogeneities, including domain walls. This can be numerically solved using the stream3 function in MATLAB. An example of the MATLAB scrips can be found in Appendix A. The calculated ranges for P_x, P_y and P_z were -0.1 to 0.7 C m^{-2}, -0.4 to 0.4 C m^{-2} and -0.1 to 0.7 C m^{-2}. The polarization grid size for the calculation was 0.004 C m^2 for P_x, P_y and P_z. The initial polarization condition for the streamline calculation is that the spontaneous polarization directed near the *x*-axis with an external stress, σ_{ij}, and without external electric field. Thus, the initial polarization vector is given as a solution to

$$\frac{\partial g}{\partial P_x} = \frac{\partial g}{\partial P_y} = \frac{\partial g}{\partial P_z} = 0 \tag{3.4}$$

To find the solution, this ordinary differential equation was solved using the MATLAB numeric solver, vpasolve function. An example of the MATLAB scripts can be found in Appendix A. The polarization vector near (P_s, 0, 0) was selected as the initial polarization vector from all solutions describing the local maxima/minima in the free energy density function. P_s is the spontaneous polarization with neither external stress nor electric field and is simply given as a solution of $\partial g/\partial P_x = 0$ at $P_y = P_z = 0$.

3.3 Results and Discussion

Figure 3.1 shows the free energy density landscape without any stress and electric field in $Pb(Zr_{0.4}Ti_{0.6})O_3$ based on equation 3.1. The left figure is a contour map in the P_x - P_z plane while the right one is that in the P_y - P_z plane. On these planes, there are six free energy minima on the axes, which represent the six directions of the off centered Ti^{4+} or Zr^{4+} ions in a *4mm* $Pb(Zr_{0.4}Ti_{0.6})O_3$. The ferroelastic polarization switching is the transition from one energy minimum

to another whose angle between them is 90°. The free energy density landscape implies that there is an energy barrier between the states which needs to be overcome to achieve ferroelastic switching.

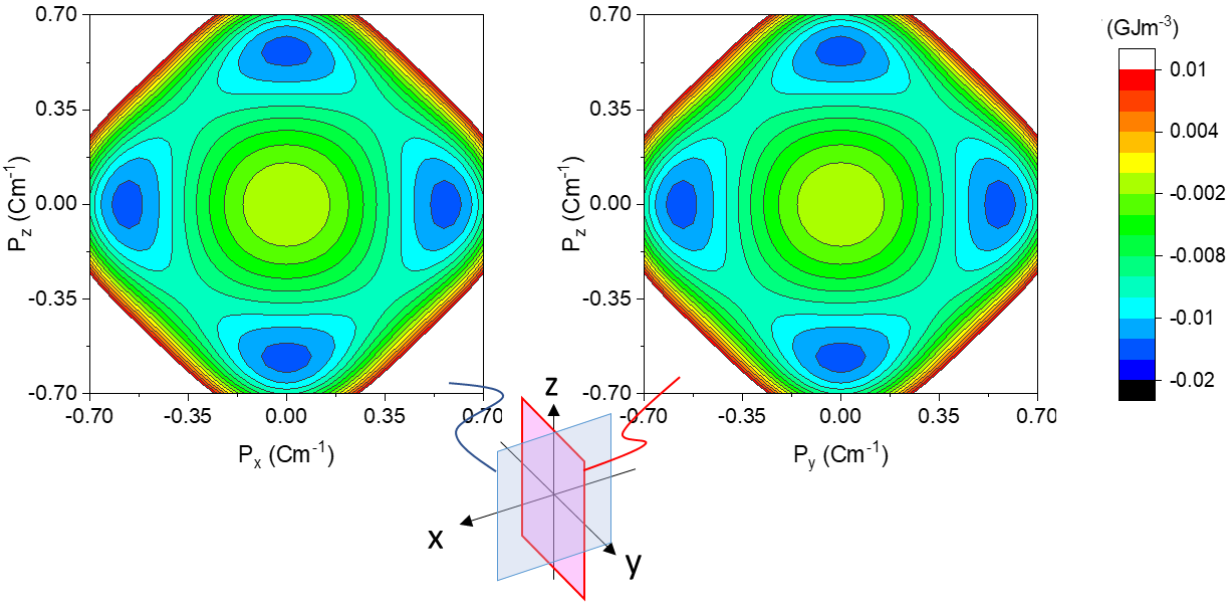

Figure 3.1. Free energy density landscape without stress nor electric field in $Pb(Zr_{0.4}Ti_{0.6})O_3$.

Figure 3.2 shows the ferroelastic polarization switching paths and free energy densities along the paths for selected E-fields in $Pb(Zr_{0.52}Ti_{0.48})O_3$ with three externally applied stress conditions: $\sigma_{ij} = 0$ (stress-free, Figure 3.2a), $\sigma_{xx} = 50$ MPa (tension, Figure 3.2b), and $\sigma_{xy} = 50$ MPa (shear, Figure 3.2c). The standard stereographic projection in a pseudo-cubic reference frame is used on these three-dimensional plots and stereographic projections for visualization, namely the pseudo-cubic [100] pole is along the *x*-axis. The material does not switch for $E_z = 4$ MVm^{-1}, whereas for $E_z = 9$ MVm^{-1} it undergoes a full switching event (Figure 3.2a). The polarization path deviates from the sphere of radius, P_r, from the initial to the final state on the $x - z$ plane. The free energy density curves along the expected polarization paths indicate that there is an energy barrier between the initial state and the final state, which corresponds to the ferroelastic switching coercive field. If a tensile stress is applied along the initial polarization direction, $\sigma_{xx} = 50$ MPa, (Figure 3.2b), the ferroelastic switching coercive field increases, as compared to without external stress, in agreement with experimentally observed ferroelastic switching behavior [13][36].

In contrast, the application of a shear stress, σ_{xy} = 50 MPa, induces the appearance of polarization states that are not coplanar with the x – z polarization plane, as shown in Figure 3.2c. Further, for E_z = 9 MV m^{-1}, the polarization vector converges to the vicinity of the [111] pseudo-cubic direction. This indicates not only the formation of an intermediate polarization state, but the energy minimizing requirement for the polarization vector to perform an elongation and rotation step, as a necessary requirement to complete a 90° switching event, from [111] to [001]. This is demonstrated for E_z > 14 MV m^{-1}, where the ferroelastic switching path is through the [111], and then rotates to the [001] pseudo-cubic direction. The free energy density curves exhibit two barriers for switching. For E_z = 9 MV m^{-1} the barrier is low enough to reach [111], but too high to reach [001]. This intermediate state corresponds to the corner of the path and is a monoclinic M_A phase, as observed at the MPB in Pb(Zr,Ti)O_3 [92]. The resultant ferroelastic switching mechanisms for non-zero σ_{yy}, σ_{zz}, σ_{yz} and σ_{xz} are equivalent to the ones already described as shown in Figure 3.3.

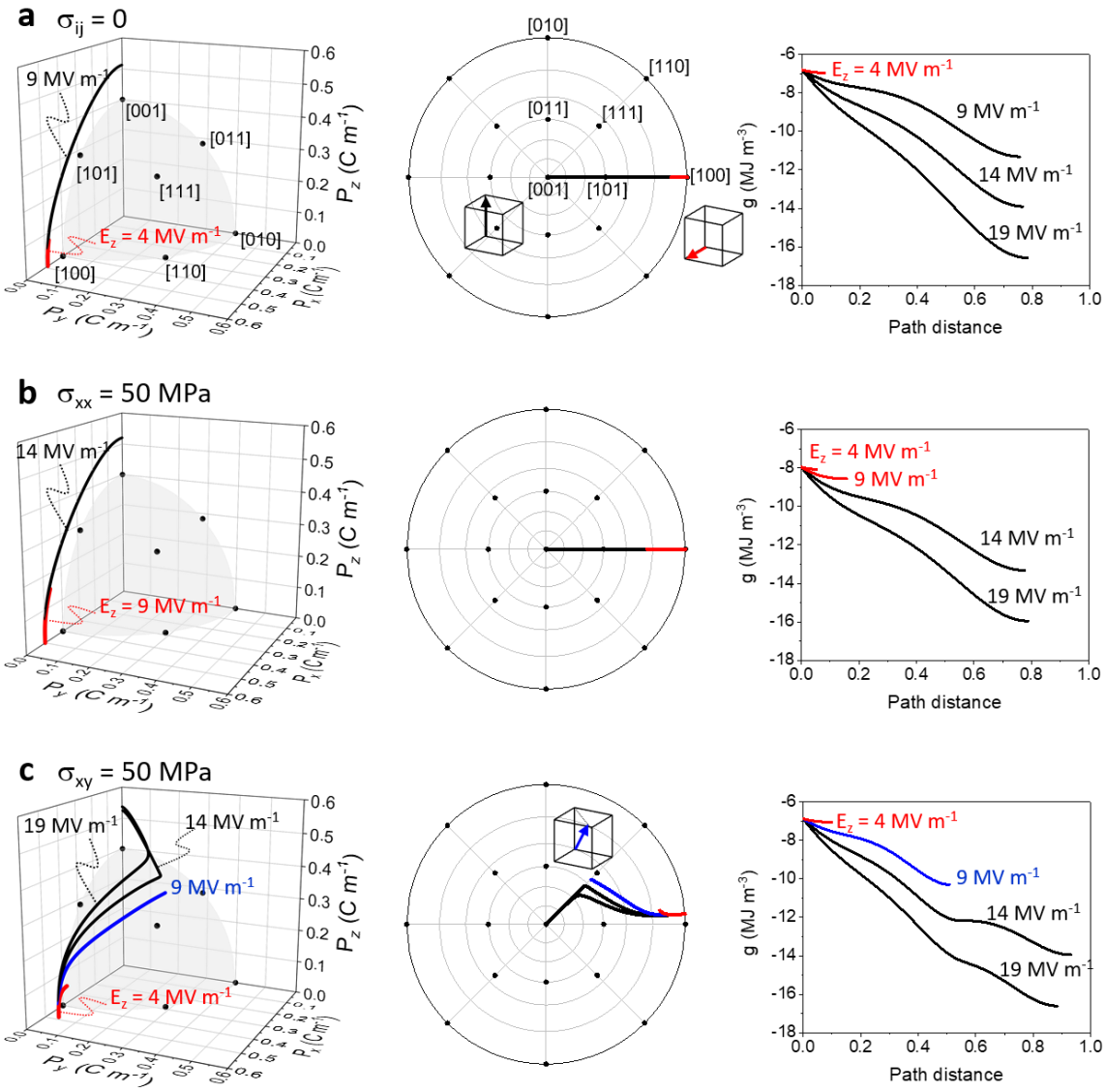

Figure 3.2. Polarization switching mechanisms in $Pb(Zr_{0.52}Ti_{0.48})O_3$ from pseudo-cubic [100] to pseudo-cubic [001]. (a) corresponds to stress-free system, (b) for external tension stress along *x*-axis (σ_{xx} = 50 MPa), and (c) for an external shear stress (σ_{xy} = 50 MPa).

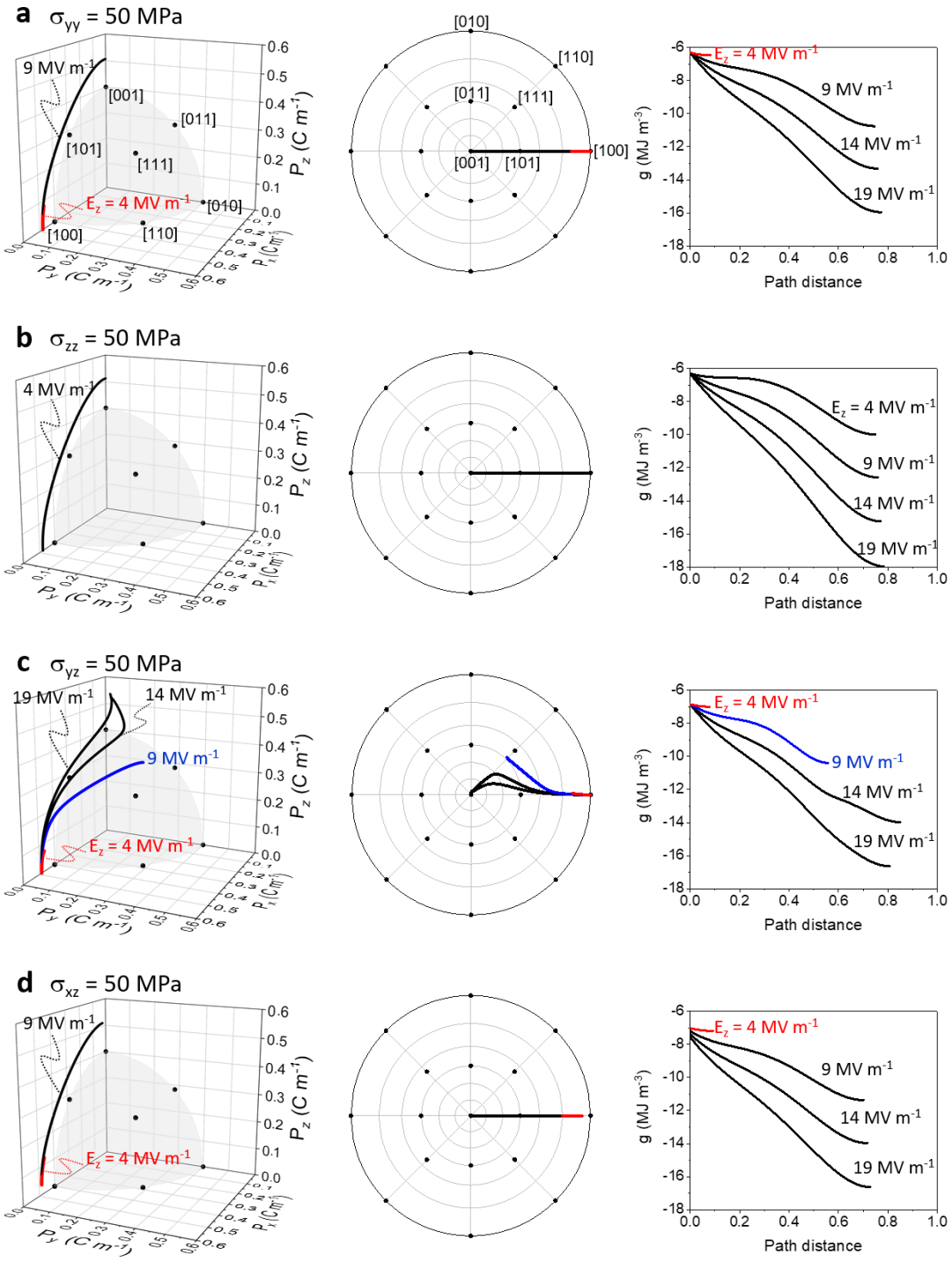

Figure 3.3. Polarization switching mechanisms in $Pb(Zr_{0.52}Ti_{0.48})O_3$ from pseudo-cubic [100] to pseudo-cubic [001]. (a) for external tension stress along *y*-axis (σ_{yy} = 50 MPa), (b) for external tension stress along *z*-axis (σ_{zz} = 50 MPa), (c) for an external shear stress (σ_{yz} = 50 MPa), and (d) for an external shear stress (σ_{xz} = 50 MPa).

Figure 3.4 shows the ferroelastic switching polarization mechanism and free energy densities for $BaTiO_3$ with selected mechanical stresses (Figure 3.4a: $\sigma_{ij} = 0$, Figure 3.4b: $\sigma_{xx} = 50$ MPa and Figure 3.4c: $\sigma_{xy} = 50$ MPa). The stress-free switching process is qualitatively equivalent to the one predicted for $Pb(Zr_{0.52}Ti_{0.48})O_3$. For $BaTiO_3$, however, the free energy density displays two energy barriers for switching, even in the absence of applied stresses. If $\sigma_{xx} = 50$ MPa (Figure 3.4b), the polarization state stabilizes at 4 MV m^{-1}, between the [101] and [001], resulting in a monoclinic metastable phase, as has been experimentally observed in $BaTiO_3$ ceramics after poling [26,34]. For a shear stress, $\sigma_{xy} = 50$ MPa, the metastable phase never appears in $BaTiO_3$. The difference in the type of stress-stabilized crystal structure between $Pb(Zr_{0.52}Ti_{0.48})O_3$ and $BaTiO_3$ is a result of the strength of the coupling terms, a_{ijkl}, which energetically penalizes the appearance of polarization states away from the expected, coplanar path. The ferroelastic switching paths with other external stress components in $BaTiO_3$ are crystallographically equivalent to the path without stress, and paths for an external σ_{yy}, σ_{zz}, σ_{yz} and σ_{xz} (50 MPa) switch directly towards the final states as shown in Figure 3.5.

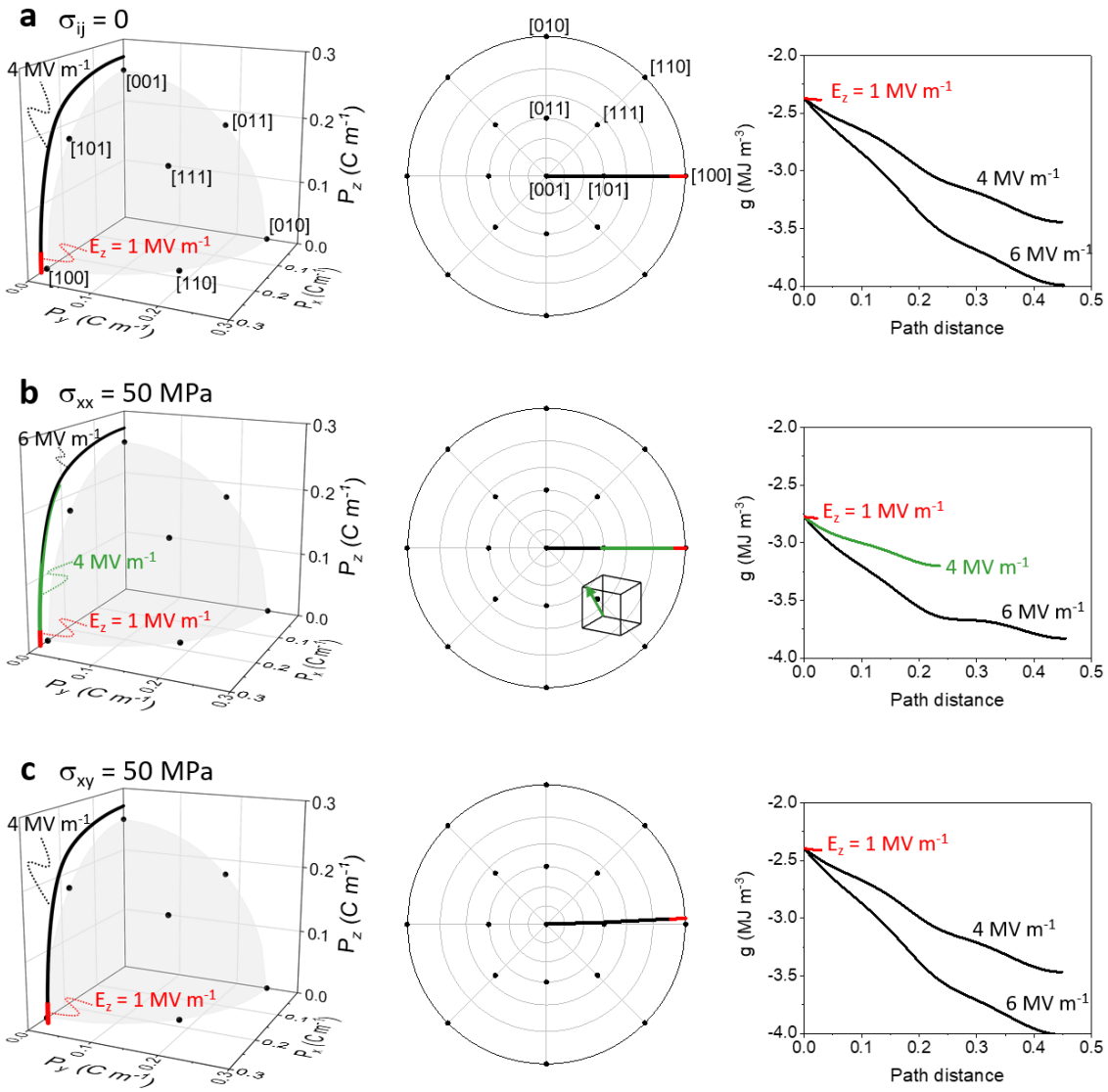

Figure 3.4. Polarization switching mechanisms in $BaTiO_3$ from pseudo-cubic [100] to pseudo-cubic [001]. (a) corresponds to stress-free system, (b) for external tension stress along *x*-axis (σ_{xx} = 50 MPa), and (c) for an external shear stress (σ_{xy} = 50 MPa).

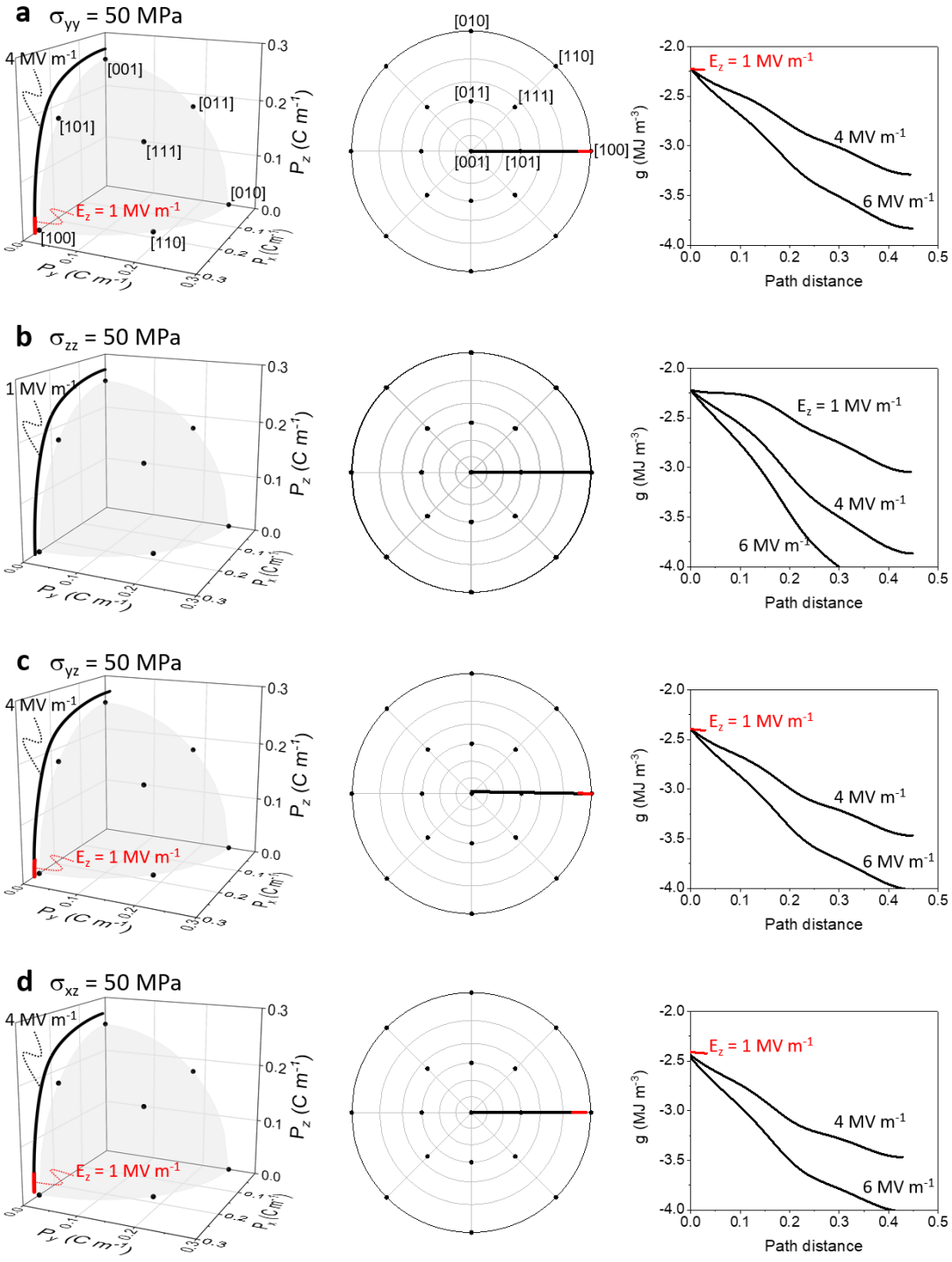

Figure 3.5. Polarization switching mechanisms in $BaTiO_3$ from pseudo-cubic [100] to pseudo-cubic [001]. (a) for external tension stress along *y*-axis (σ_{yy} = 50 MPa), (b) for external tension stress along *z*-axis (σ_{zz} = 50 MPa), (c) for an external shear stress (σ_{yz} = 50 MPa), and (d) for an external shear stress (σ_{xz} = 50 MPa).

The difference in the type of the stress-stabilized crystal structures between $Pb(Zr_{0.52}Ti_{0.48})O_3$ and $BaTiO_3$ comes from the second most energetically stable phases in those materials. In $Pb(Zr_{0.52}Ti_{0.48})O_3$, the free energy densities along near the <100> and <111> directions show the local minima and comparable values each other whereas those along the <110> direction exhibit a saddle point and higher than those of <100> and <111> directions, which can be seen in free energy landscapes on the spontaneous polarization sphere surface and axis planes (see supplementary Figure 3.6a). In $BaTiO_3$, on the contrary, the free energy densities along near the <100> and <110> directions show local minima whereas that along the <111> direction exhibits a saddle point and higher than those of <100> and <110> directions (see supplementary Figure 3.6b). Thus, the polarization path tends to deviate from the coplanar path to near <111> in $Pb(Zr_{0.52}Ti_{0.48})O_3$, but not in $BaTiO_3$. These facts are likely reflected by the stable phases adjacent to the tetragonal phase, which are the rhombohedral in Zr rich $Pb(Zr,Ti)O_3$ phase and the low temperature orthorhombic phase in $BaTiO_3$. From the phenomenological model perspective, the sign of the axis coupling a_{112233} coefficient plays a key role in determining whether the free energy density along <111> is a local minimum or saddle point. The axis coupling term with a positive coefficient increases the free energy in a polarization state along <111> while one with a negative coefficient reduces the free energy density along <111>.

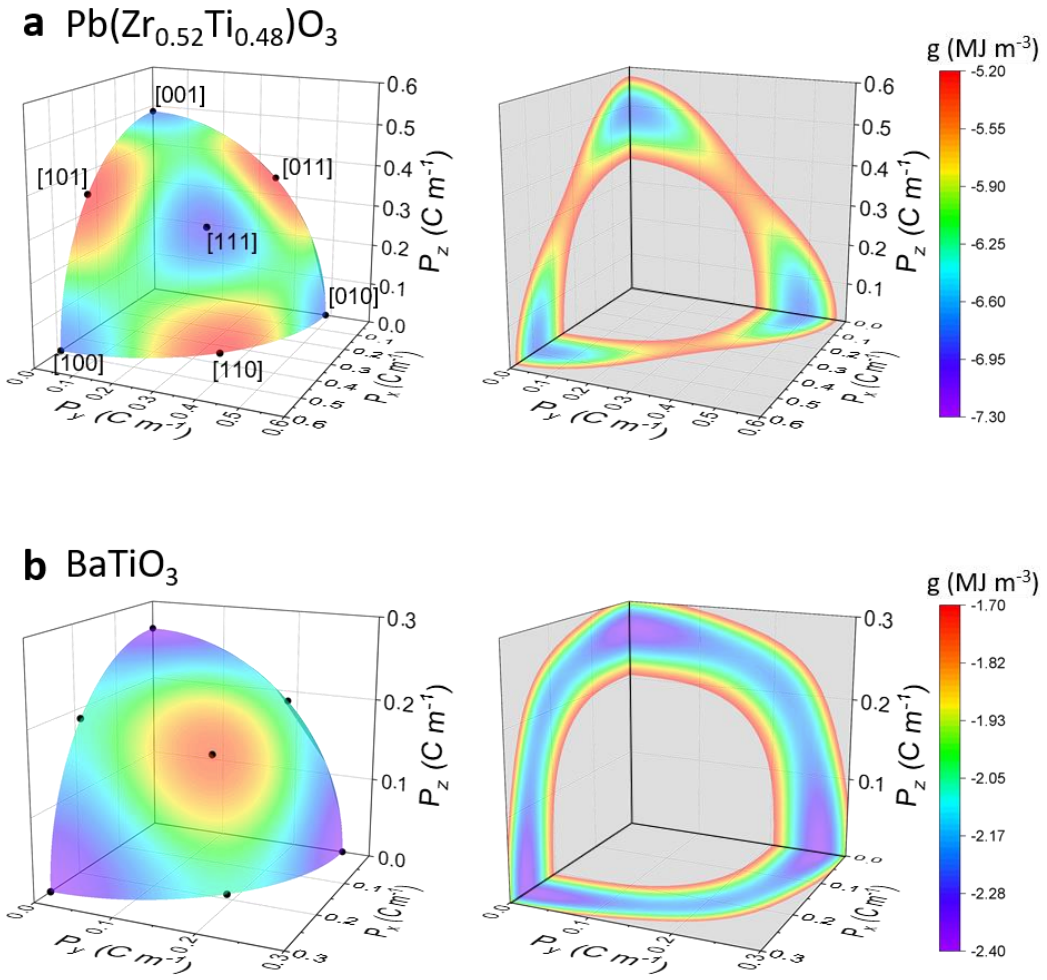

Figure 3.6. Free energy density landscape on spontaneous polarization sphere surface (left) and *x*-*y*, *y*-*z* and *x*-*z* planes (right). (a) for $Pb(Zr_{0.52}Ti_{0.48})O_3$ (P_s = 0.486), (**b**) for $BaTiO_3$ (P_s = 0.265). Gray area in planes has larger than the scale maximum.

In addition to that, the sensitivity of the free energy change due to an applied stress likely contributes to the deviation from the coplanar path in $Pb(Zr_{0.52}Ti_{0.48})O_3$. The change of the free energy density landscape due to the applied stress in the polarization space is attributed to the stress-polarization coupling term, $-Q_{ijkl}\sigma_{ij}P_kP_l$, so that the electrostrictive coefficient $Q_{2323} = Q_{1313} = Q_{1212}$ determines the sensitivity of the free energy change associated with the applied shear stress, and the free energy change maximizes at $|P_k| = |P_l|$ ($k \neq l$) which includes the <111> polarization state. As the coefficients in $Pb(Zr_{0.52}Ti_{0.48})O_3$ (0.080 m^4 C^{-2}) [88] is about three times larger than the one in $BaTiO_3$ (0.029 m^4 C^{-2}) [90], the free energy density in $Pb(Zr_{0.52}Ti_{0.48})O_3$ is more

susceptible to the applied shear stress than that in $BaTiO_3$. Thus, the free energy density near the <111> polarization state decreases more in $Pb(Zr_{0.52}Ti_{0.48})O_3$, so that the polarization path switches towards the vicinity of <111> state. The origin of the large electrostrictive coefficient comes from the sensitivity of the polarization induced strain, given the nature of the electrostrictive coefficient. $Pb(Zr_{0.52}Ti_{0.48})O_3$ exhibits more shear strain per an electric field induced polarization perpendicular to the spontaneous polarization compared to $BaTiO_3$. Note that $BaTiO_3$ piezoelectric coefficient d_{113} expressed as $2Q_{1313}\kappa_{11}P_s$ is larger than PZT d_{113} due to the much larger electric permittivity κ_{11} in $BaTiO_3$ [93]. This material property in $Pb(Zr_{0.52}Ti_{0.48})O_3$ induces the larger free energy reduction at the <111> polarization state and the polarization path deviation towards near the <111>. In the specific transition from P_x to P_z with shear stress σ_{xz}, however, the polarization path stays in the *x*-*z* plane as shown above in Figure 3.3d. This is likely due to the large reduction of the energy barrier in the coplanar path from P_x to P_z. The largest free energy density decrease occurs at the [101] polarization state because the coupling term, $-Q_{2323}\sigma_{xz}P_xP_z$ minimizes at the state (see supplementary Figure 3.7), so that the polarization gradient descent direction stays on the *x*-*z* plane in contrast to the cases with σ_{yz} and σ_{xy}.

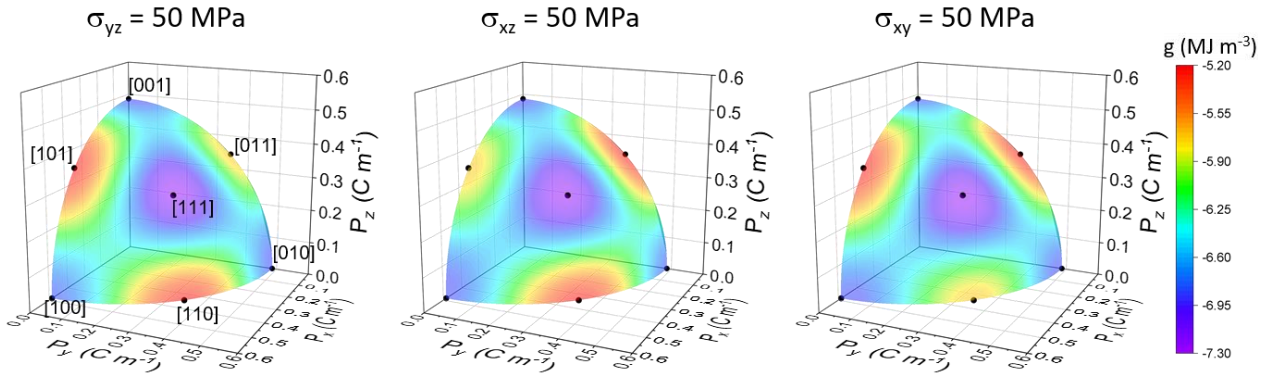

Figure 3.7. Free energy density landscape on spontaneous polarization sphere surface in $Pb(Zr_{0.52}Ti_{0.48})O_3$ with σ_{yz} (left), σ_{xz} (middle) and σ_{xy} (right).

Figure 3.8 shows the regions of phase stability for $Pb(Zr_{0.52}Ti_{0.48})O_3$ as a function of applied E-field and state of stress, σ_{yz} (Figure 3.8a) and σ_{xy} (Figure 3.8b). The solid line, dashed line, and dash-dotted line represent the coercive electromechanical field to induce a ferroelastic or structural

transition. The calculated coercive electric field value in this study is in agreement with Nakajima et al [94]. There, experimentally reported out-of-plane polarizations abruptly increase at 10 MVm^{-1} for $Pb(Zr_{0.5}Ti_{0.5})O_3$ thin films [94], which is associated with ferroelastic domain wall motion. The gap between our calculation and the experimental result is a result of the composition difference and the compatibility stresses induced by the substrate, which are not considered in our calculation. For both shear stress components, the structural transition to the monoclinic phase occurs. The electric field range of the stability of the stress-induced monoclinic phase is wider for a larger stress and significant (3 – 16 MV m^{-1} at σ_{xy} = 100 MPa).

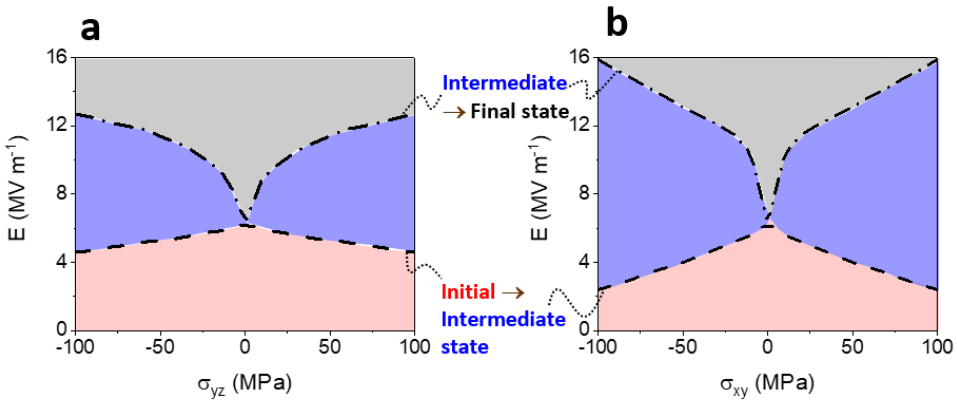

Figure 3.8. Ferroelastic switching coercive electric fields for each stress component in $Pb(Zr_{0.52}Ti_{0.48})O_3$. (a) for σ_{yz} shear stress and (b) for σ_{xy} shear stress. Solid lines, dashed lines and dash-dotted lines represent coercive electric fields of switching from the initial to final states, the initial to intermediate states and the intermediate to final states.

For other external stress states, where σ_{xx}, σ_{yy}, σ_{zz} and σ_{xz}, are non-zero, the thermodynamic analysis predicts direct switching from [001] to [100] variants as shown in Figure 3.9. As expected from the ferroelastic switching coercive field change in Figure 3.2b, a tensile stress raises the coercive field while a compressive stress (negative value) reduces it for σ_{xx}. Similarly, for $\sigma_{zz} > 0$ (tensile) reduces the ferroelastic switching coercive field, while $\sigma_{zz} < 0$ (compressive) increases it. σ_{vv} and σ_{xz} also have slight effects on the ferroelastic switching coercive field, although the directions of these stresses do not directly relate to the initial and final polarization axes because of the free energy density change due to the axis coupling.

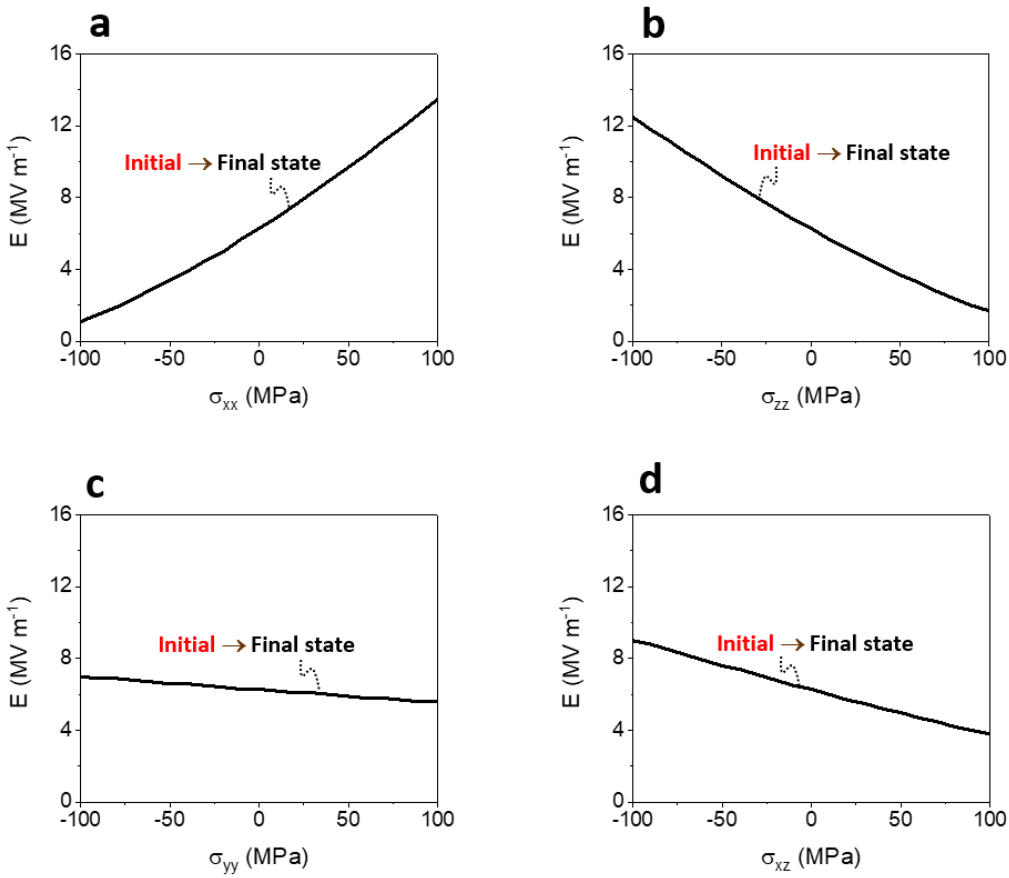

Figure 3.9. Ferroelastic switching coercive electric fields for each stress component in $Pb(Zr_{0.52}Ti_{0.48})O_3$. (a) for normal stress along *x*-axis, (b) for normal stress along *z*-axis, (c) for normal stress along *y*-axis, and (d) for σ_{xz} shear stress.

Figure 3.10 shows the stable electromechanical states as a function of applied E-field and stresses for $BaTiO_3$. The ferroelastic switching coercive field at zero stress is 1.8 MV m^{-1} in this calculation, which is comparable to the reported experimental data in a single crystal (~1 MV m^{-1}) [67]. The stress-induced monoclinic (*M*c) phase is predicted only for the tensile stresses, $\sigma_{xx} > 0$, and $\sigma_{zz} > 0$, as shown in Figure 3.10a and b. The intermediate state is achieved above 20 MPa of $\sigma_{xx} > 0$ (tensile) or below -20 MPa of σ_{zz} (compressive). This is because the free energy of the initial and final states due to tensile stresses are comparable, and at a local minimum. A compressive σ_{zz}-value, induces a free energy potential whose final state is shallow. The ferroelastic switching coercive field increases with increasing σ_{xx} and decreases with increasing σ_{zz} as shown above in $Pb(Zr_{0.52}Ti_{0.48})O_3$.

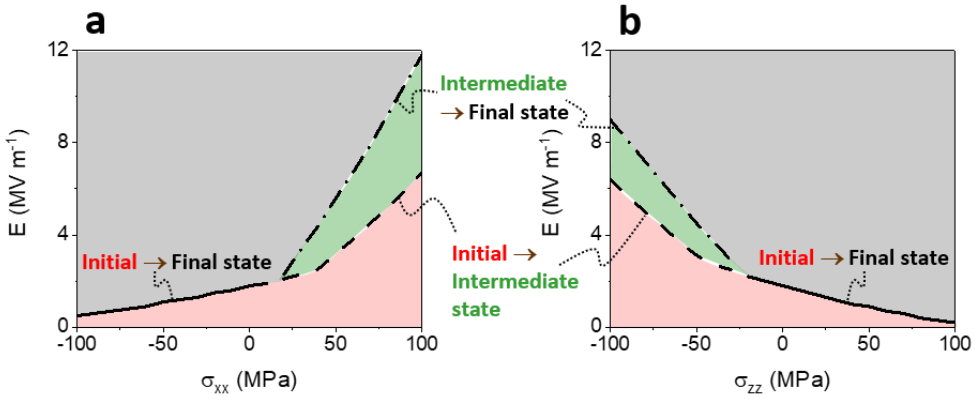

Figure 3.10. Ferroelastic switching coercive electric fields for each stress component in $BaTiO_3$. (a) for σ_{xx} normal stress along *x*-axis and (b) for σ_{zz} normal stress along *z*-axis. Solid lines, dashed lines and dash-dotted lines represent coercive electric fields of switching from the initial to final states, the initial to intermediate states and the intermediate to final states.

For other external stress components, σ_{yy}, σ_{yz}, σ_{xz} and σ_{xy}, thermodynamics predict the direct transition from [100] to [001] polarization states as shown in Figure 3.11. Unlike $Pb(Zr_{0.52}Ti_{0.48})O_3$, the shear stresses, σ_{yz} and σ_{xy}, neither affect the ferroelastic switching coercive field nor induce the intermediate state as expected from the paths.

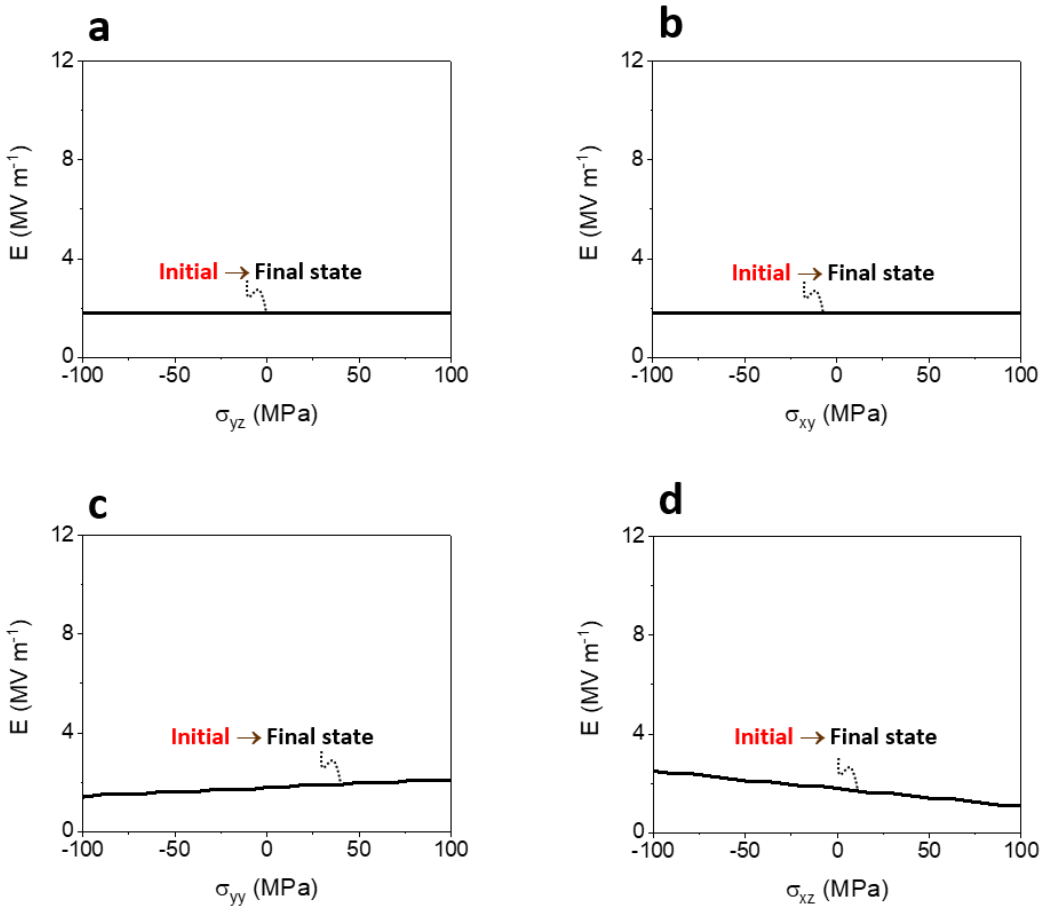

Figure 3.11. Ferroelastic switching coercive electric fields for each stress component in $BaTiO_3$. (a) for σ_{yz} shear stress, (b) for σ_{xy} shear stress, (c) for normal stress along *y*-axis, and (d) for σ_{xz} shear stress.

Figure 3.12 summarizes the composition dependence of the monoclinic phase in $Pb(Zr,Ti)O_3$, and shows the switching coercive fields as a function of the $PbTiO_3$ fraction with σ_{xy} = 50 MPa. The monoclinic phase is only predicted near the MPB, $PbTiO_3$ mole fraction = 0.48 ~ 0.52. For mole fractions greater than 0.52, no intermediate state is stabilized although the switching path is not contained in the *x* - *z* plane, as one would traditionally expect shown in Figure 3.13 - Figure 3.15. This result is in agreement with reported experimental [27,95] measurements. This suggests that stresses and E-fields can be tailored to improve the extrinsic electromechanical properties in $Pb(Zr,Ti)O_3$. The low symmetry phase near the MPB is known as an important component for electromechanical properties as it has higher dielectric and piezoelectric coefficient [27,96]. The volume fraction of low symmetry phase can be tuned by applying stresses and E-field,

so that electromechanical properties likely increase. Lattice and substrate thermal expansion mismatch, crystallographic texture, grain shape, and heat treatment procedure are among the possible controlling variables [39].

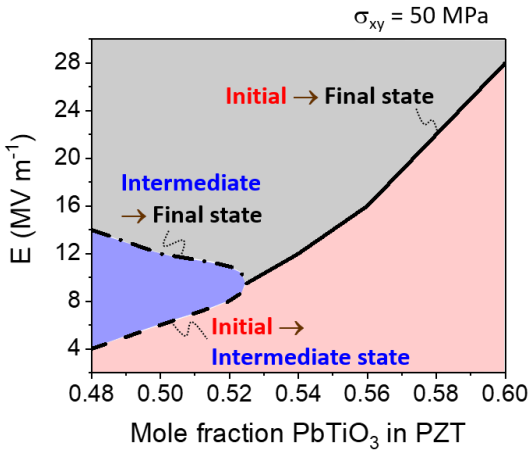

Figure 3.12. Composition dependence of switching coercive electric fields with shear stress (σ_{xy} = 50 MPa) in $Pb(Zr,Ti)O_3$. Solid lines, dashed lines and dash-dotted lines represent coercive electric fields of switching from the initial to final states, the initial to intermediate states and the intermediate to final states.

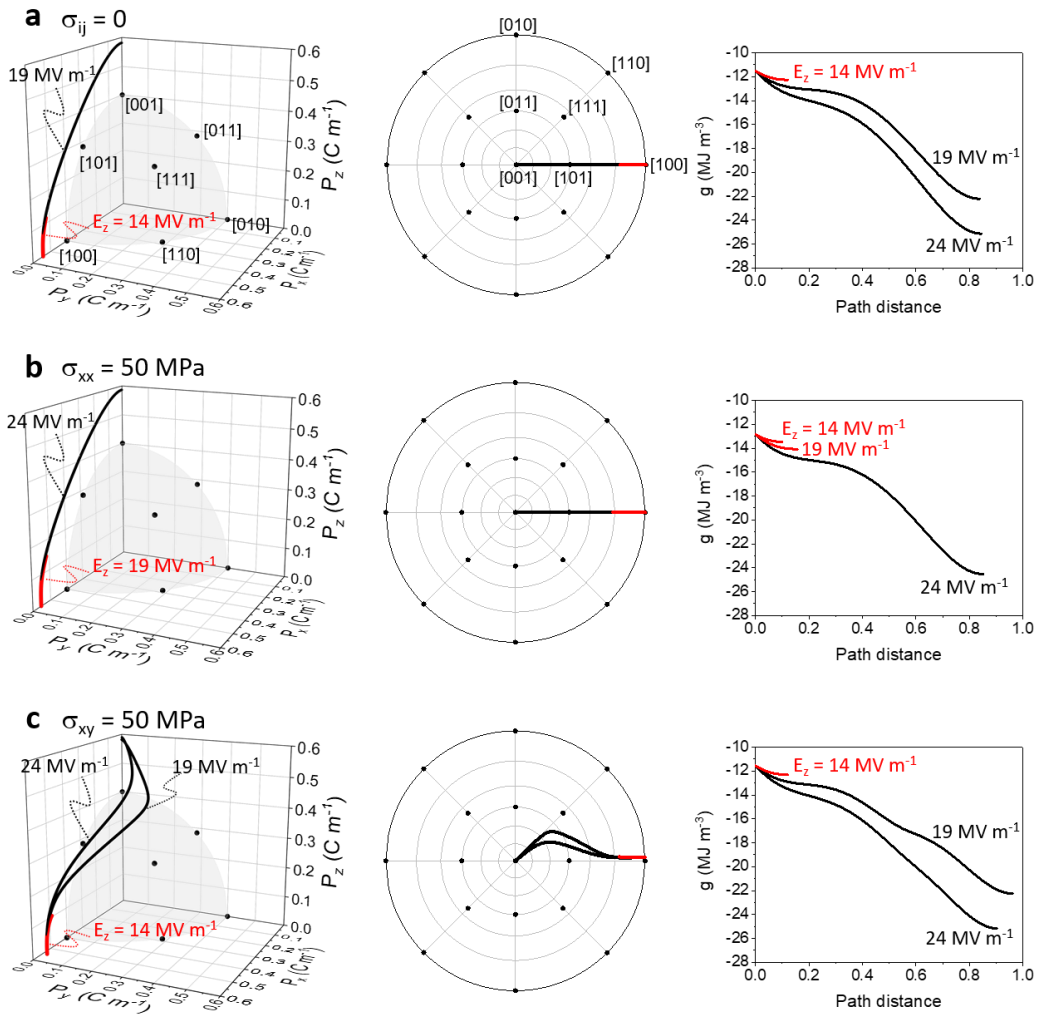

Figure 3.13. Polarization switching mechanisms in $Pb(Zr_{0.44}Ti_{0.56})O_3$ from pseudo-cubic [100] to pseudo-cubic [001]. (a) corresponds to stress-free system, (b) For external tension stress along *x*-axis (σ_{xx} = 50 MPa), and (c) for an external shear stress (σ_{xy} = 50 MPa).

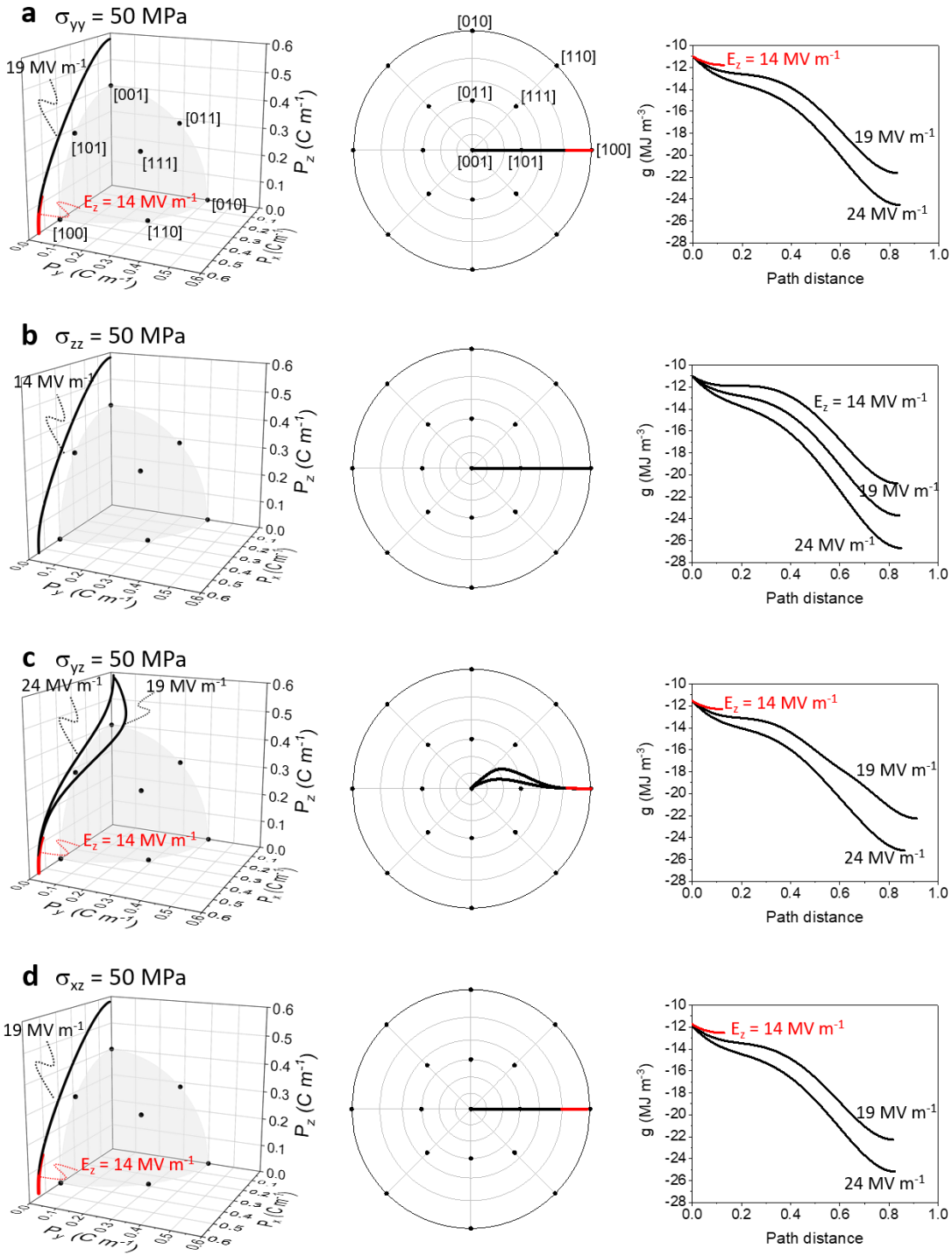

Figure 3.14. Polarization switching mechanisms in $Pb(Zr_{0.44}Ti_{0.56})O_3$ from pseudo-cubic [100] to pseudo-cubic [001]. (a) for external tension stress along *y*-axis (σ_{yy} = 50 MPa), (b) for external tension stress along *z*-axis (σ_{zz} = 50 MPa), (c) for an external shear stress (σ_{yz} = 50 MPa), and (d) for an external shear stress (σ_{xz} = 50 MPa).

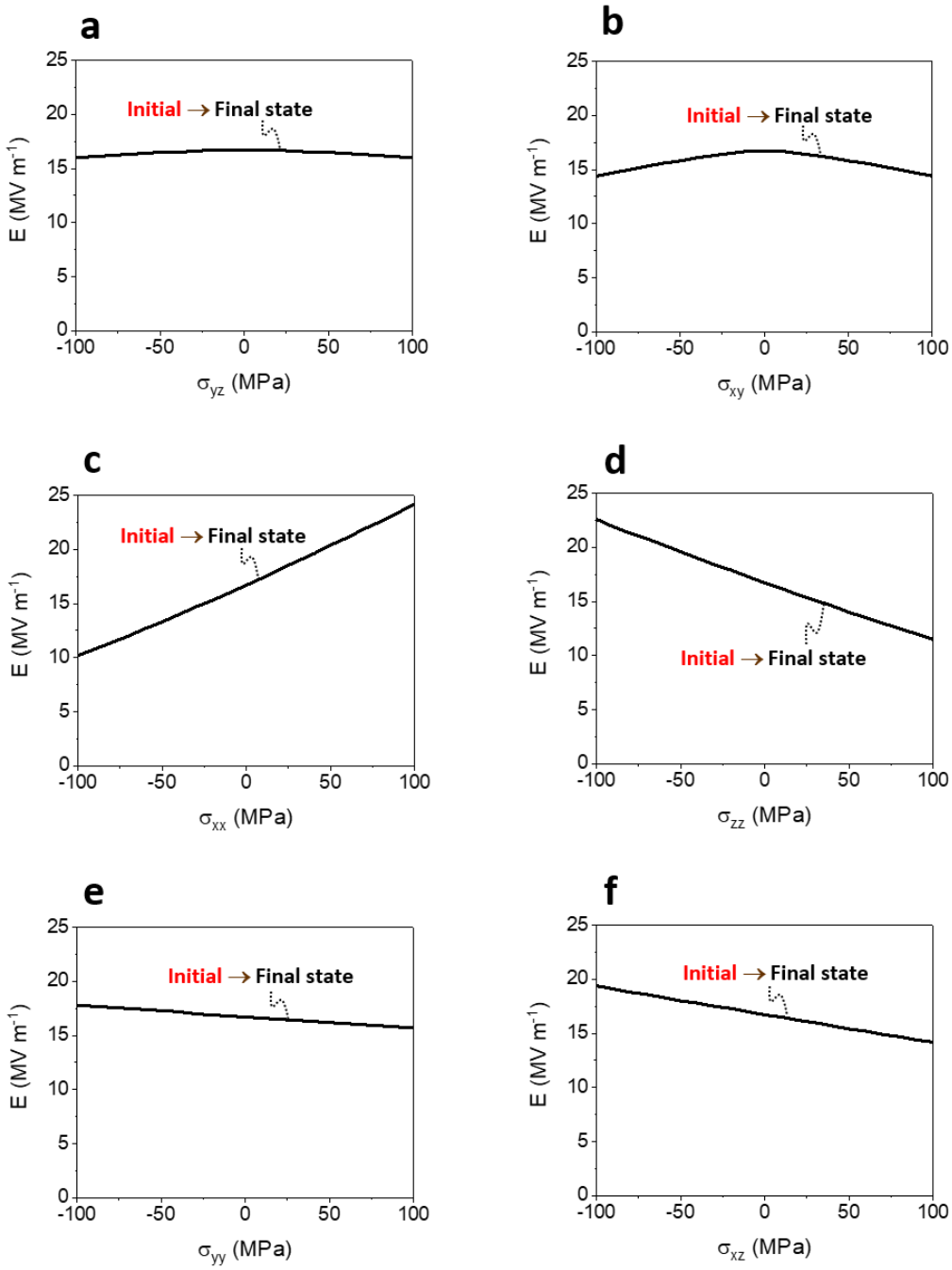

Figure 3.15. Ferroelastic switching coercive electric fields for each stress component in $Pb(Zr_{0.44}Ti_{0.56})O_3$. (a) for σ_{yz} shear stress, (b) for σ_{xy} shear stress, (c) for normal stress along *x*-axis, (d) for normal stress along *z*-axis, (e) for normal stress along *y*-axis, and (f) for σ_{xz} shear stress.

3.4 Conclusion

In summary, the polarization switching path that results from the multiphysical, externally applied electrical fields and six independent mechanical field tensor components was analytically predicted for $Pb(Zr_{0.52}Ti_{0.48})O_3$ and $BaTiO_3$. These electromechanical effects not only quantify the ferroelastic switching coercive field, but also rationalize the experimentally observed low-symmetry phases after poling in $Pb(Zr_{0.52}Ti_{0.48})O_3$ (M_A phase) and $BaTiO_3$ (M_C phase) ceramics. In contrast to what have been previously reported, neither electric field along pseudo cubic [111] nor [101] is energetically favorable for polarization rotation and to stabilize the low symmetry phases observed in $Pb(Zr_{0.52}Ti_{0.48})O_3$ and $BaTiO_3$ ceramics. The difference in the metastable phases between the two materials is likely originated from the second most stable phases and the sensitivity of the free energy change due to an applied shear stress in each material. Residual stresses due to the processing and microstructural interactions are responsible for enabling these effects. Due to the significant range of the stabilization of these intermediate states, the fraction of the low-symmetry phase can be controlled by selecting appropriate stress and electric field conditions for poling. Stress manipulation not only enables tuning of the ferroelastic switching coercive field, but also provides a new paradigm to engineer the phase fraction of the low-symmetry phases to improve the resultant extrinsic piezoelectric properties, as the low-symmetry phase plays an important role in the macroscopic electromechanical response at the MPB.

4. BARKHAUSEN NOISE ANALYSIS OF THIN FILM FERROELECTRICS

A portion of this chapter is a reprint, with journal permission, of a previous publication in Applied Physics Letters [97], DOI: 10.1063/5.0012635.

4.1 Introduction

Magnetic Barkhausen noise comes from the irregular/intermittent/discontinuous local magnetization or demagnetization processes of a ferromagnetic material from external excitations (magnetic, thermic or even mechanical [98]). As the magnetic domain distribution is unstable, even a weak external stimulus can easily modify this distribution [99]. Over the magnetization/demagnetization processes, some domains are growing while others are shrinking and this is a dynamic state determined by energy minimization [100]. Variations in domain size and shape will generate domain wall movements and local magnetic flux variations that can be detected externally. The Barkhausen noise signal is linearly connected to the domain wall speed. The speed, the density and the timing of the Barkhausen noise events are directly correlated with the specimen microstructure, including precipitates, local residual stresses, cracks and any defects that influence domain wall displacements. In bulk materials, magneto-striction and local thermal coupling prevent stable states from one magnetization cycle to another and MBN becomes a stochastic phenomenon with the signals observed always fundamentally different. The domain distribution is so unstable and unpredictable that identical Barkhausen response never occurs. However, under extremely controlled conditions, a certain degree of reproducibility has been observed but only in thin layers where identical stable states are easier to be reached [101–103]. Historically for the study of the magnetic Barkhausen noise (*MBN*), researchers have tried to replace this erratic raw signal with reproducible parameters. For their simplicity, the raw signal RMS value or the *MBN* envelope are the most common parameters used [104–106]. More recently, Magnetic Barkhausen Noise energy (MBN_{energy}) has been proposed [107–109] and is defined as:

$$MBN_{energy} = \int_0^{t_0} sgn\left(\frac{dH}{dt}\right)(V_{Barkhausen})^2 dt \tag{4.1}$$

where t_0 is the excitation field period and $V_{Barkhausen}$ is the Barkhausen raw signal in volts. By plotting the MBN_{energy} as a function of a magnetic field H, a hysteresis cycle MBN_{energy} vs H is

obtained. In practice, where a multitude of domain walls are displaced quasi-simultaneously and spatially distributed within the specimen, the resulting signal is composed of microsecond pulses, which are the superposition (whether constructive or destructive) of these induced pulses. By integrating the square of the signal (equation 4.1), the resulting area of the MBN_{energy} vs H cycle is an image of the kinetic energy dissipated during the magnetization/demagnetization processes. Normalization of the MBN_{energy} loop allows comparison to the magnetic hysteresis loop and interesting hysteresis cycles comparisons can be made. In the case of ferromagnetic materials characterized by a high magneto-crystalline anisotropy energy, both hysteresis shapes are similar. This observation leads to the conclusion that the domain wall motion is dominant compared to the domain magnetic moment rotations during the magnetization process. Oppositely, strong differences are observed for materials of low magneto-crystalline anisotropy energy where the coexistence of both contributions is more evident.

The parallel between the ferromagnetic magnetization and the ferroelectric polarization is evident and has been widely discussed [110]. Ferroelectric domain wall motion has already been observed by piezoelectric response force microscopy (PFM) [111,112] and optical microscopy [113]. Related to domain wall kinetics, crackling noises associated with the motion of ferroelectric-paraelectric phase transformation front [114] and ferroelastic domain wall [115] motion have been observed. Very recently, Tan *et al* reported a switching current noise and its self-organized criticality in ferroelectric bulk ceramics with post-processing [116]. These authors detected a polarization switching current and then extracted the "noise" from it as the time derivative of the current as the switching current directly reflect the polarization switching kinetics. However, a Barkhausen noise spectra as observed for ferromagnetic materials (erratic, oscillating signal with a spectral content varying from approximately 1 kHz to almost 100 kHz) has never been observed in ferroelectrics. The advantage of the classic Barkhausen noise analysis is potential usability for measurement of the dynamics of domain wall motion as the classic Barkhausen noise includes noise frequency information. In addition, it allows us to investigate the domain wall dynamics at an actual driving condition, unlike a stroboscopic domain wall observation done by PFM. These advantages are critical for accurate modeling of the dynamics of switching in ferroelectrics and microstructure design to improve performance. From an application perspective, thin ferroelectric films are interesting for ferroelectric applications such as FeRAM and MEMS [2,3]. Given that polarization switching plays a critical role in these devices, a Barkhausen noise analysis for thin

film ferroelectrics is important as it can directly assess the dynamics of ferroelectric switching. Moreover, considering these applications, local analysis is important due to the small device size. One difficulty is that the capacitive current and leakage current can affect the measurement due to the relatively higher capacitance and lower resistance of thin films as compared to bulk ceramics.

In this study, the first direct Barkhausen noise measurement in local regions (~50 μm^2) in ferroelectric thin films is reported. A hysteresis cycle of EBN_{energy}, is reconstructed from the Barkhausen noise. The thin film used here is a 300 nm thick polycrystalline $Pb(Zr_{0.4}Ti_{0.6})O_3$ on $(111)Pt/TiO_2/(100)Si$ substrate, which is the same sample investigated in chapter 2. The crystalline phase and microstructure of the film are found in chapter 2. For the local measurement, a Pt probe directly contacted the sample surface. The Barkhausen noise was extracted from the switching current through the Pt bottom electrode.

4.2 Switching Current Detection

In a ferroelectric material, ferroelectric polarization switching induces a current flow through electrodes due to the surface charge transfer [117]. As the current flow is the time derivative of the change in charge, the switching current flows during only the switching event. In other words, the time integral of the switching current corresponds to the surface charge change due to the polarization reversal. The surface charge change is a constant determined by the material spontaneous polarization and a polarization switched area. To obtain a clear switching current peak, therefore, ferroelectric switching excitation frequency needs to be optimized, i. e. a higher frequency results in a shorter switching duration, thereby generating a larger switching current peak. Figure 4.1 shows the switching current (red line) in the film excited with 100 and 10 Hz triangular electric fields (black line). The larger current peak is observed in the 100 Hz excitation result as expected. In this study, the 100 Hz excitation is employed for the sharp current peak.

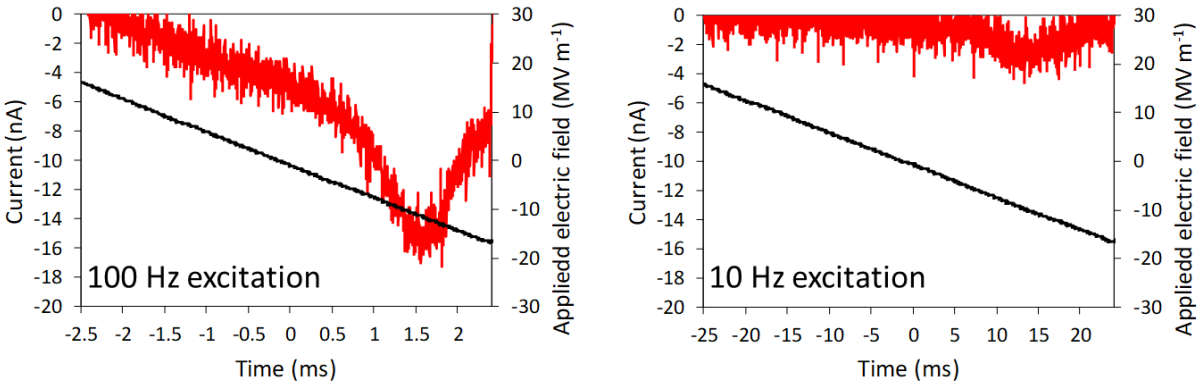

Figure 4.1. Switching current with 100 Hz (left) and 10 Hz (right) excitation electric fields.

4.3 Results and Discussion

Figure 4.2a shows the schematic diagram of the experimental setup. An AC voltage (5 V_{P-P}, 100 Hz) was applied to the sample through the Pt probe (Figure 4.2b). The electrical current was amplified and converted to a voltage signal by the trans-impedance amplifier (OPA657 with 10 MΩ of feedback resistance). The cut off frequency of the amplifier was set near 100 kHz as shown in Figure 4.2c, so that the critical noise data was not cut-off at this stage. A bandpass filter was used to extract the Barkhausen noise and amplify it from the amplifier output signal. To measure the switching current and get the *P-E* hysteresis loop, the bandpass filter is removed. The switched surface area was estimated from a PFM vertical phase image after poling using the Pt probe as shown in Figure 4.2d. The image was a standard PFM image [54] at the Pt probe contact location. Prior to the PFM image, -5 V was applied through the Pt probe, so that the darker region (negative polarization) in the image shows the active area in this measurement setup, and it is determined to be 55 μm^2.

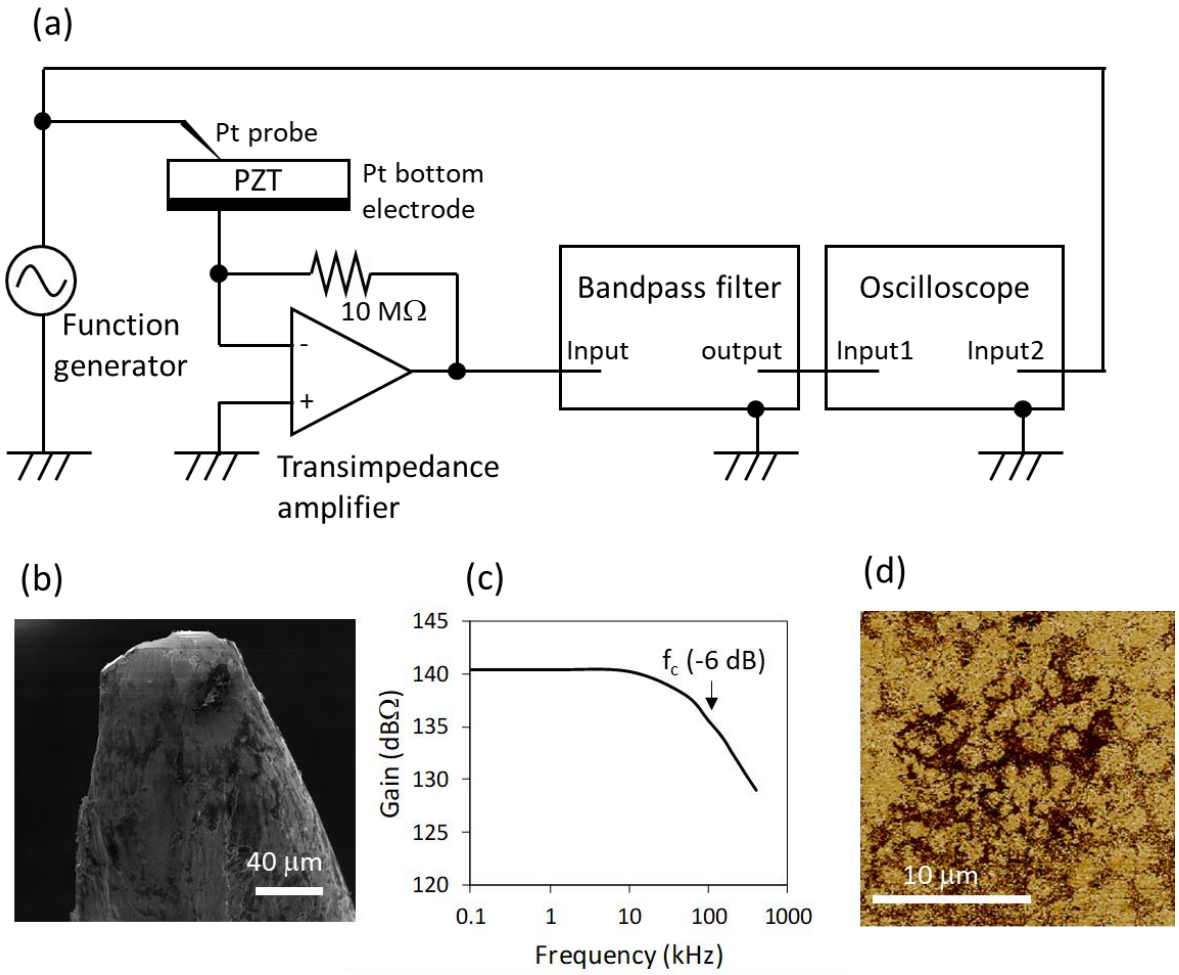

Figure 4.2. Barkhausen noise measurement setup. (a) Schematic diagram of equipment configuration. (b) SEM image of Pt probe contacted to PZT sample. (c) Bode plot of transimpedance amplifier. (d) Vertical phase PFM image of PZT sample after -5 V poled with Pt probe. Darker region represents active surface area in this Pt probe.

The switching current (red line) and the applied sinusoidal electric field (black line) are shown in Figure 4.3a. The measurement was conducted first without the bandpass filter to measure the current response. The data exhibits current spikes superimposed on a sine wave with a phase shift from the applied electric field. The sine wave is the capacitive current and the leakage current. These currents can be estimated using the film capacitance and resistance. Figure 4.3b shows the capacitance – frequency (*C*-*F*) and the current – voltage (*I*-*V*) curves used to determine the constants, and the currents. The *I*-*V* curve shows a clear ohmic relationship. The capacitance and resistance are respectively 1.5 pF at 100 Hz and 4 GΩ. The current from the capacitance and resistance is calculated by modeling a parallel equivalent circuit as shown in this figure. In Figure

4.3c the calculated current is subtracted from the raw signal current (Figure 4.3a), removing this component of the signal and the switching current spikes are clearly seen at specific applied electric fields, representing the coercive electric field (~10 MV m^{-1}). The switching current includes the Barkhausen noise, but it is hard to directly extract the Barkhausen noise from the signal as other signal components (100 Hz excitation component and amplifier noise for example) are superimposed.

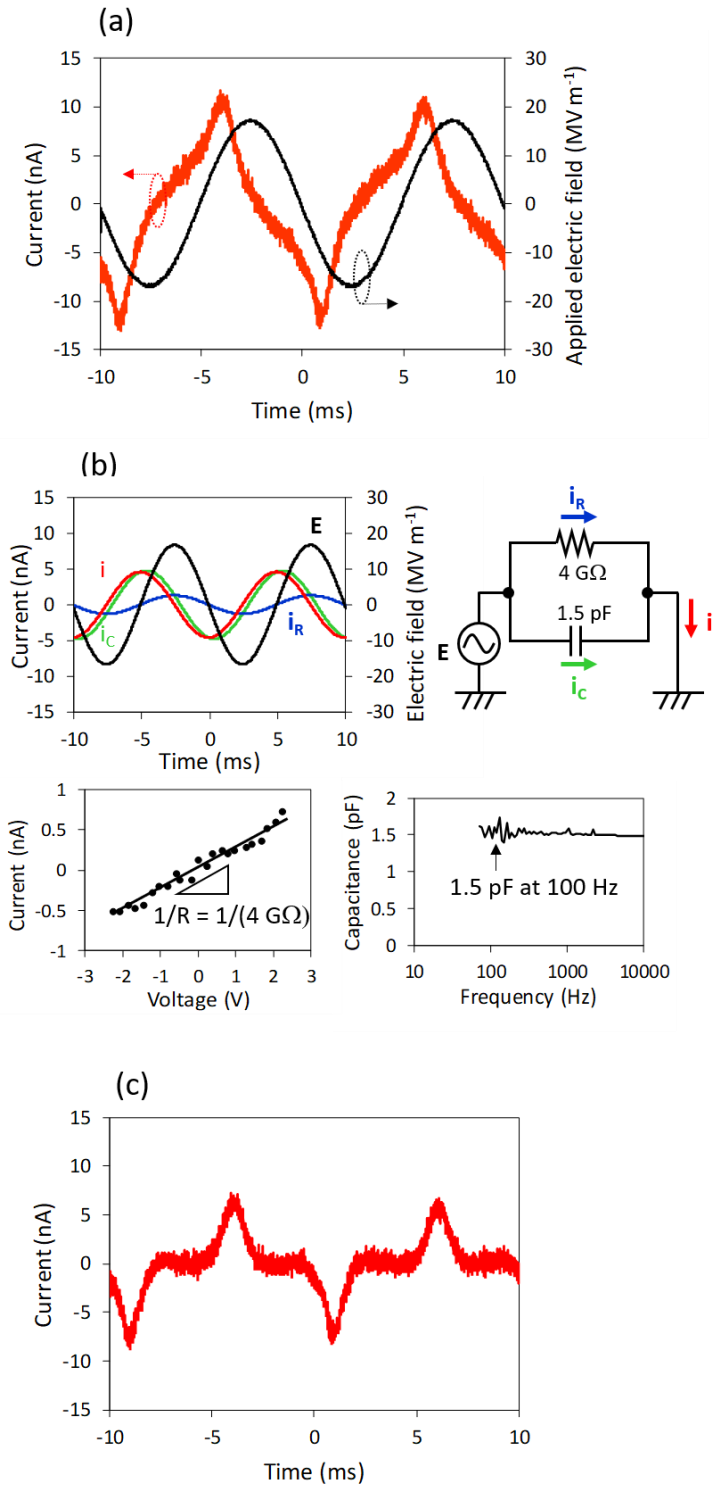

Figure 4.3. Switching current excited by 5 $V_{p\text{-}p}$ (16.7 MV m^{-1}) 100 Hz sine wave. (a) Measured current through amplifier (red line) and applied electric field (black line). (b) Calculated capacitive and leakage current based on *I-V* curve (bottom left) and *C-F* curve (bottom right). (c) Switching current extracted from measured current using the calculated capacitive and leakage current.

Ferroelectric *P* vs *E* hysteresis loops are generated as an integral of the switching current as shown in Figure 4.4. The polarization is approximated by a Riemann sum, $\sum I\Delta t$, and plotted as a function of the applied electric field. The solid line is calculated from the switching current extracted from the raw measured current with the estimated leakage and capacitive current whereas the broken line is from the raw current in Figure 4.3. The *P* vs *E* hysteresis loop from the extracted switching current does not exhibit neither the linear polarization increase due to the applied electric field nor the rounded shape in the loop as they are associated with the dielectric permittivity (proportional to the capacitance) and leakage current component [62]. The remanent polarization value is ~0.1 C m^{-2} in this measurement, which is smaller than the result shown in Figure 2.8. This difference is likely originated from the amplitude of the applied electric field. In this chapter, applied electric field is 16.7 MV m^{-1}, corresponding to 5 V which is near the coercive voltage of the film. Thus, the loop is not a fully opened hysteresis loop due to the relatively low applied electric field. However, as the switching current was clearly observed in Figure 4.3, the small loop is not critical to extract the Barkhausen noise out of the current.

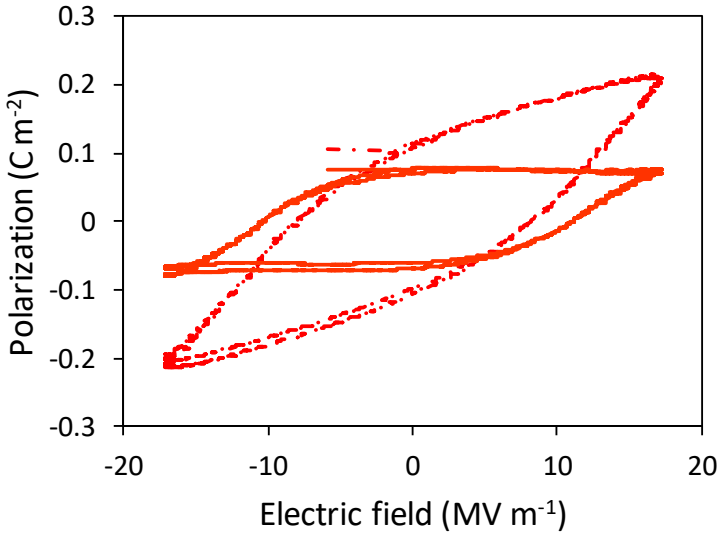

Figure 4.4. Ferroelectric *P* vs *E* hysteresis loop as time integral of switching current. Solid line is calculated from extracted switching current, and broken line is from measured raw current.

To extract the Barkhausen noise, a bandpass filter is used to separate the high amplitude 100 Hz excitation component from the target signal. Figure 4.5 shows the filtered current data with various frequency bands, 1 – 2 kHz, 2 – 4 kHz, 5 – 10 kHz, 10 – 20 kHz and 20 – 40 kHz. The blue lines are the filtered current, and the black lines are the applied electric field. The red broken lines represent the time when the electric field reach the coercive electric field from the hysteresis loop shown in Figure 4.4. For the 1 – 2 kHz band, no significant Barkhausen noise is observed at the coercive field when the maximum domain wall motion occurs. Instead of that, a large noise not related to the domain wall motion is seen. The frequency band from 2 to 20 kHz exhibits clear activities at the coercive electric field, and these activities stand out of noises at the non-switching time. Thus, it is concluded that these activities are the Barkhausen noise associated with the domain wall pinning. For the frequency range from 20 to 40 kHz, these activities are buried with the surrounding noises and get weaker, although some slight activities are observed. Based on the results, the frequency bandwidth from 2 to 20 kHz is the best condition for the Barkhausen noise extraction in this film. This bandwidth corresponds to 500 μs - 50 μs in the time domain. A single domain wall jump distance in this time scale is easily estimated for a given domain wall velocity. Tybel *et al* reported that the domain wall velocity without pinning can be expressed as $\exp(-E_0/E)$ with E_0 = 50 MV m^{-1} for a tetragonal PZT [118]. The velocity is estimated as 6700 μm s^{-1} at E = 10 MV m^{-1}, the coercive field of this film, and the domain wall jump distance is 0.35 to 3.5 μm. Considering the grain size in this film is 0.5~2 μm (in-plane direction) times 0.3 μm (thickness), it is most likely the grain boundary acts as a dominant domain wall pinning site, in good agreement with previously reported studies [50,53,119]. This result comes from the ferroelectric Barkhausen noise associated with the all grains in the probe contact area. An analysis of the individual events potentially yields statistical insight such as the grain size distribution and avalanche nature of ferroelectric domain wall motion, which require further investigation.

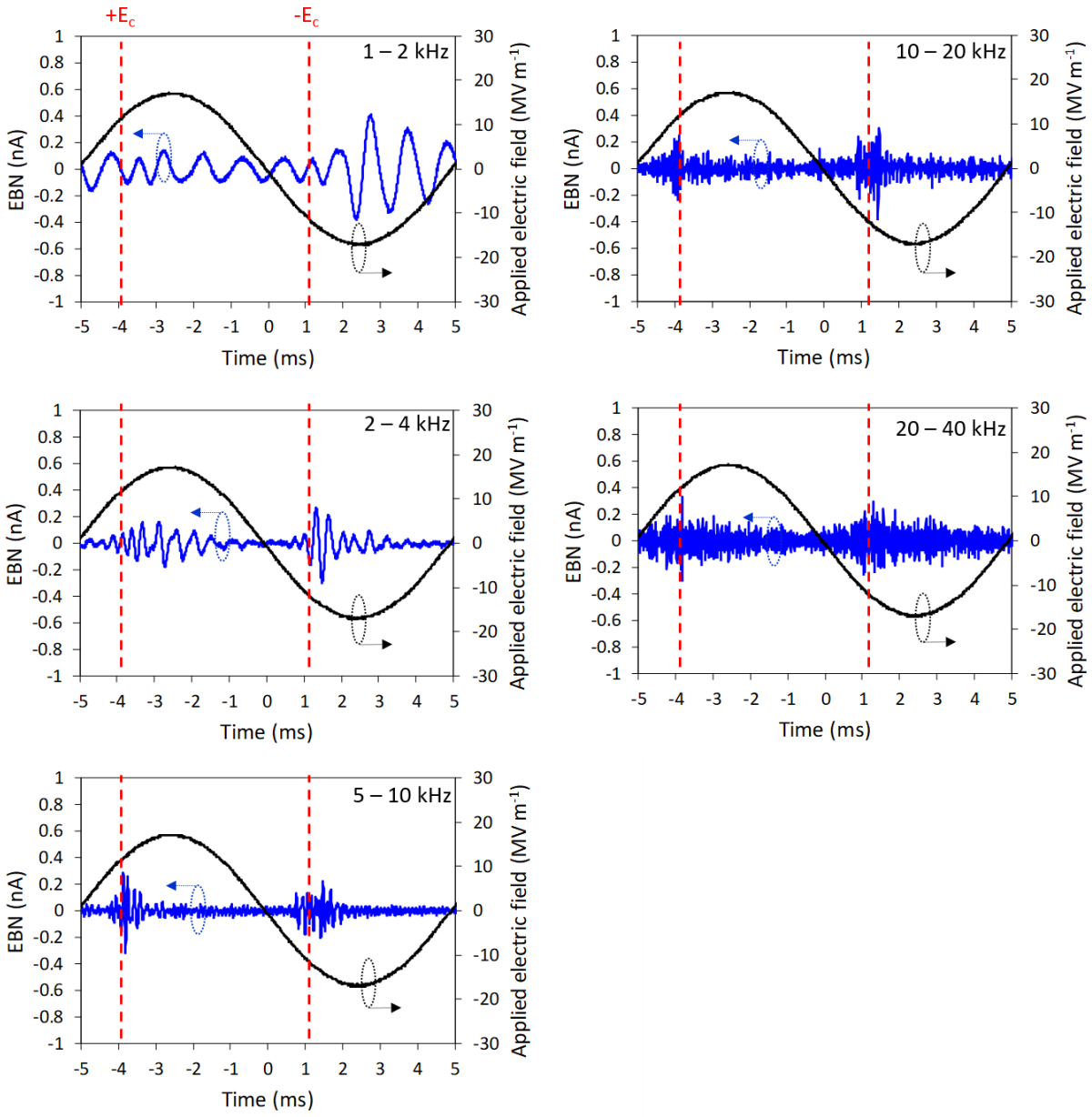

Figure 4.5. Filtered switching current with various bandwidths. Black lines are applied electric field. Broken red lines are the time when electric field reach coercive field.

The current filtered with the best bandwidth (2 – 20 kHz) is shown in Figure 4.6a. The blue line represents the filtered current data and the black line is the applied electric field sine wave. Similar to ferromagnetic materials, the ferroelectric Barkhausen noise shows stochastic behavior. The maximum activity is always observed at an electric field close to the coercive electric field (10 MV m^{-1}). To go forward with the understanding of the ferroelectric Barkhausen noise,

following usage in ferromagnetism, the ferroelectric Barkhausen noise energy hysteresis cycle, EBN_{energy} vs E can be plotted to yield a reproducible Barkhausen noise indicator with physical interpretations.

Figure 4.6b gives the process of the EBN_{energy} vs E hysteresis cycle reconstruction process. The process is analogous to that for ferromagnetic materials [108] with the field is the electric field and the signal is the electric current. The EBN_{energy} can be expressed as

$$EBN_{energy} = \int_0^{t_0} sgn\left(\frac{dE}{dt}\right)(I_{Barkhausen})^2 dt \tag{4.2}$$

where t_0 is the excitation field period and $I_{Barkhausen}$ is the ferroelectric Barkhausen raw current signal. The process in Figure 4.6b shows how the EBN_{energy} vs E loop is generated. The EBN_{energy} vs E loop has a clear hysteresis as observed in ferromagnetic materials [108]. To confirm and validate our ferroelectric Barkhausen noise measurement, a comparison between the reconstructed EBN_{energy} vs E cycles and the classic P vs E poling loop is shown in Figure 4.4c. The blue cycle is the reconstructed EBN_{energy} vs E cycle and the red cycle is the classic hysteresis loop P vs E obtained from the integration of the current measurement (Figure 4.6c). Both P vs E and EBN_{energy} vs E hysteresis cycles show closed absolute coercive field values, confirming the maximum Barkhausen noise activity over this field. Both hysteresis shapes are relatively closed as well, validating the Barkhausen noise measurement. Small divergence can be observed at the saturation elbow possibly due to accumulative issues during the reconstruction processes. This zone is particularly sensitive as the relative permittivity is changing rapidly. Another potential origin is the effect of polarization rotation due to electric field [23]. As the EBN_{energy} hysteresis loop should only contain a signal from the domain wall motion due to the nature of the Barkhausen activity, polarization changes such as dielectric response and polarization rotation do not contribute to the EBN_{energy}. Here, the dielectric response was already considered in the capacitive current subtraction process (Figure 4.4b), so that the polarization rotation can be the candidate causing the difference between the loops. This is supported by the thermodynamic study shown in chapter 3, investigating possible polarization rotations at a shear residual stress and relatively low electric field condition in PZT.

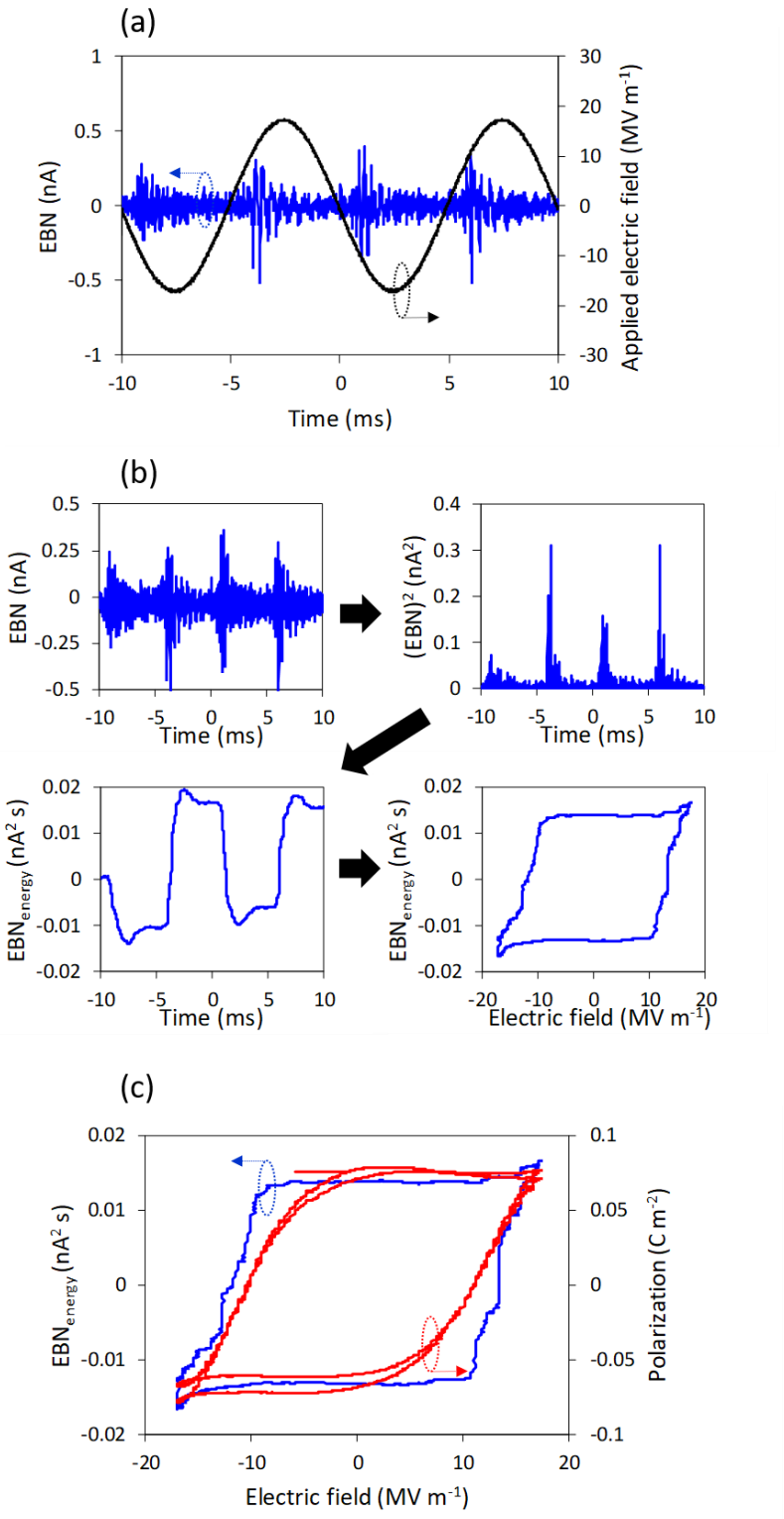

Figure 4.6. *EBN* and reconstructed EBN_{energy} loop. (a) Measured *EBN* current through bandpass filter (blue line) and applied electric field (black line). (b) Process to convert *EBN* to EBN_{energy} loop. (c) Comparison between EBN_{energy} and polarization loop as a result of integration of switching current shown in Figure 4.4.

4.4 Conclusion

In conclusion, the ferroelectric Barkhausen noise and the Barkhausen noise energy hysteresis cycles reconstruction using a bandpass filter for noise extraction, which is well-studied technique in ferromagnetic materials, was firstly observed. The ferroelectric Barkhausen noise has a similar behavior to what has been observed in ferromagnetic materials; the classic ferroelectric P vs E hysteresis loop and EBN_{energy} vs E cycle was closely related. The optimal bandwidth for the Barkhausen noise extraction was the time duration of the domain wall motion across grains, thereby supporting the idea that grain boundaries play a key role in domain wall pinning and cause Barkhausen noise. This direct Barkhausen noise measurement is suggested as a good tool for the analysis of the microstructure – domain wall kinetics relationship.

5. SUMMARY AND FUTURE WORK

This research was conducted to understand the microstructure effects including grain size, residual stress on the polarization response in ferroelectrics. The polarization response in ferroelectrics is the important feature for ferroelectric applications. Ferroelectric switching is the fundamental principle for FeRAM, and electric field induced ferroelastic polarization switching and polarization rotation are the dominant contribution to electromechanical devices. In polycrystalline ferroelectrics, effects of the microstructural parameters such as texture, grain size, and residual stress exist and have not fully been understood due to its complexity. Among these effects, this dissertation addresses (1) the origin of the grain size effects on ferroelastic domain wall motion in a polycrystalline ferroelectric thin film, (2) mechanical stress effects on polarization switching using a thermodynamic approach, and (3) ferroelectric switching kinetics via Barkhausen noise analysis and the relationship to grain size in the polycrystalline ferroelectric thin film. The summary and future work for each topic are discussed as follows.

For the investigation of grain size effects on the electromechanical property, the microscopic origin of ferroelastic domain wall motion suppression in smaller grains which causes degradation of the property is revealed. The microscopic origin was unclear due to the large X-ray diffraction probe size in a previous study reporting the suppression of ferroelastic domain wall motion. Using PFM technique to observe microscopic domain evolutions with applied DC voltage, it is discovered that there is actually no independent grain size effect on ferroelastic domain wall motion; the grain size affects the number of domain stripe colonies in a grain, and the domain structure plays an important role in ferroelastic domain wall motion. This result suggests that the grain size is not a critical parameter for the electromechanical property degradation in a grain < 1 μm as the ferroelastic domain wall motion is a dominant component for the electromechanical property.

Possible future work is engineering the domain structure to improve the electromechanical property. As the domains can be formed due to stress relaxation during cooling across the Curie temperature in a synthesis process, the stress state before the domain formation (above the Curie temperature) should affect the domain structure. The possible stress-free strain inhomogeneity across grain boundaries is thermal expansion, so that grain misorientation is likely a key for determining the stress state above the Curie temperature, according to Eshelby's inclusion model.

Thus, an examination of the relationship between the misorientation and domain structure provides an insight of the origin of the domain structure and a way to engineer it.

Further future work can be improving the electromechanical property in polycrystalline ferroelectrics by mitigating the property degradation based on the insight about the domain engineering. Texture control is likely a good method to adjust a misorientation for accomplishing the preferable domain structure. In polycrystalline ferroelectrics, changing the orientation of a substrate or seed layer helps controlling the texture. For bulk ceramics, using a template is a known way to control texture. Improving the electromechanical property can be achieved by determining the optimal texture based on investigation of the correlation of texture – domain structure – ferroelastic domain wall motion.

The study about the mechanical stress effects on the electric field induced polarization switching rationalizes the emergence of the electric field induced low-symmetry phases in tetragonal PZT and $BaTiO_3$ ceramics. The mechanism causing the emergence of the low-symmetry phases was thought to be polarization rotation due to the applied electric field. However, what causes the difference in the low-symmetry phases of PZT (monoclinic M_A phase) and $BaTiO_3$ (monoclinic M_C phase) was unsure. Also, the lack of the evidence of the electric field induced polarization rotation in a single crystal was questioned. In this work, with a thermodynamic approach, it is demonstrated that a shear stress plays an important role in stabilizing the monoclinic M_A phase in PZT whereas a normal stress along the polarization axis is a key for the monoclinic M_C phase in $BaTiO_3$. It is suggested that the stress sources are residual stress in a polycrystalline form, so that the lack of the electric field induced polarization rotation in PZT and $BaTiO_3$ single crystals can be explained. This study provides a new paradigm for the low-symmetry phase engineering in ferroelectrics by applying an appropriate stress and electric field, so that improvement of the electromechanical response is expected as the low-symmetry phase is known to be a key role in the large electromechanical response at the MPB.

Future work is obtaining the experimental evidence for the low-symmetry phase engineering and the electromechanical property improvement. Based on the calculated stress and electric field condition in this study, a systematic investigation for the relationship between the low-symmetry phase fraction vs the stress and electric field conditions will provide a further insight of the low-symmetry phase engineering and the optimal condition to maximize it. An examination of the

macroscopic and microscopic electromechanical properties of the engineered sample will give us the solid evidence and mechanism of the electromechanical property improvement.

One other possible future investigation related to the stress effects on polarization switching is analysis in various symmetries and materials in ferroelectrics using the thermodynamic approach. The work done here is in tetragonal ferroelectrics. Rhombohedral ferroelectrics such as a Zr rich PZT also show electric field induced ferroelastic switching. The thermodynamic approach may provide a stress – electric field condition and possible low-symmetry phases in the rhombohedral ferroelectrics. Moreover, the electric field induced polarization rotation is also seen in $Na_{0.5}Bi_{0.5}TiO_3$-$BaTiO_3$, $BiFeO_3$ and relaxer ferroelectrics. The comprehensive examination for these materials rationalizes the mechanism of polarization rotation and possible other phases depending on thermodynamic variables.

Extendedly, the gradient descent method utilized in this work can be employed for other multi-variable systems to identify the transition path and possible metastable phases. In a multidimensional free energy density landscape with multiple order parameters, the path can deviate away from a plane including the variable axes, especially in a coupled system, as this study pointed out. This can be a new methodology for designing metastable phases during the transition between the states.

For the work about ferroelectric switching kinetics, the first direct Barkhausen noise associated with ferroelectric domain wall motion is observed. A previous study reported Barkhausen activity in ferroelectrics, but there is a gap for practical use of the technique because of the lack of Barkhausen noise frequency information and post data processing in the report. In this study, a direct Barkhausen noise measurement including noise frequency information is achieved. It is discovered that the dominant domain wall pinning site is grain boundaries based on the noise frequency corresponding to the domain wall jump distance between pinning sites. This result suggests that the technique is a good tool for understanding the relationship between microstructure – domain wall kinetics.

Future research can be a study on the relationship between the Barkhausen noise and artificial pinning sites such as vacancies. It is known that an annealing condition manipulates the oxygen vacancy density, and the ferroelectric *P*- *E* hysteresis loop shows pinned behavior. The vacancy density – Barkhausen noise relationship can lift the technique up to more practical method to

investigate the vacancy density and domain switching kinetics via the direct Barkhausen noise measurement technique developed in this dissertation.

In conclusion, the effects of a grain boundary and stress, which can be manipulated as microstructural parameters, on polarization switching are investigated in ferroelectrics. This dissertation provides the experimental evidences that grain boundaries play a significant role in both ferroelectric and ferroelastic domain wall motion, which are important for ferroelectric and electromechanical applications. In addition, the theoretical framework proves the non-trivial polarization switching behavior induced by an electric field and mechanical stress which naturally occurs in a polycrystalline as a residual stress. The model explains polarization rotation and the low-symmetry phases appearing in $BaTiO_3$ and PZT ceramics. These low symmetry phases are regarded as the origin of the large electromechanical property at the MPB in PZT. Future works based on these discoveries should be carried out to improve the properties of ferroelectric and electromechanical devices.

APPENDIX A. MATLAB SCRIPT FOR POLARIZATION SWITCHING PATH

A MATLAB script for the streamline calculation in a stress and electric field condition in $Pb(Zr_{0.52}Ti_{0.48})O_3$ is as follows. To calculate the entire stress and electric field variable window, the script was looped. The numerical coefficients vary depending on composition as shown in Table 3.1.

```
[Px,Py,Pz] = meshgrid(-0.1:0.004:0.7,-0.4:0.004:0.4,-0.1:0.004:0.7);
u = -(0.85226003438856*Px.^5+2.59843785278887*Py.^2.*Px.^3+2.59843785278887*Pz.^2.*Px.^3+0.220080752066131*Px.^3+1.29921892639443*Py.^4.*Px+1.29921892639443*Pz.^4.*Px+-6.12659833446545*Py.^2.*Pz.^2.*Px+0.344687393813874*Py.^2.*Px+0.344687393813874*Pz.^2.*Px+-9.94742781887373E-02*Px+0*Py+0*Pz+0);
v = -(0.85226003438856*Py.^5+2.59843785278887*Pz.^2.*Py.^3+2.59843785278887*Px.^2.*Py.^3+0.220080752066131*Py.^3+1.29921892639443*Pz.^4.*Py+1.29921892639443*Px.^4.*Py+-6.12659833446545*Pz.^2.*Px.^2.*Py+0.344687393813874*Pz.^2.*Py+0.344687393813874*Px.^2.*Py+-9.94742781887373E-02*Py+0*Pz+0*Px+0);
w = -(0.85226003438856*Pz.^5+2.59843785278887*Px.^2.*Pz.^3+2.59843785278887*Py.^2.*Pz.^3+0.220080752066131*Pz.^3+1.29921892639443*Px.^4.*Pz+1.29921892639443*Py.^4.*Pz+-6.12659833446545*Px.^2.*Py.^2.*Pz+0.344687393813874*Px.^2.*Pz+0.344687393813874*Py.^2.*Pz+-9.94742781887373E-02*Pz+0*Px+0*Py+-0.02);
XYZ = stream3(Px,Py,Pz,u,v,w,0.48591,0,0)
streamline(stream3(Px,Py,Pz,u,v,w,0.48591,0,0))
file = fopen('SL001-001.txt','w');
fprintf(file,'%f\r\n',0);
fprintf(file,'%f\r\n',0);
fprintf(file,'%f\r\n',0);
fprintf(file,'%f\r\n',0);
```

```
fprintf(file,'%f\r\n',0);
fprintf(file,'%f\r\n',0);
fprintf(file,'%f\r\n',0);
fprintf(file,'%f\r\n',0);
fprintf(file,'%f\r\n',0.02);
fprintf(file,'%f\r\n','');
fprintf(file,'%f\r\n',XYZ{1,1});
fclose(file);
```

The MATLAB script for calculating the initial polarization vector with a stress condition in $Pb(Zr_{0.52}Ti_{0.48})O_3$ is as follows. To calculate the entire stress variable range, the script was looped. The numerical coefficients vary depending on composition as shown in Table 3.1.

```
syms Px Py Pz
eqn1 =
0.85226003438856*Px.^5+2.59843785278887*Py.^2.*Px.^3+2.59843785278887*Pz.^2.*Px.^3
+0.220080752066131*Px.^3+1.29921892639443*Py.^4.*Px+1.29921892639443*Pz.^4.*Px+-
6.12659833446545*Py.^2.*Pz.^2.*Px+0.344687393813874*Py.^2.*Px+0.344687393813874*P
z.^2.*Px+-9.94742781887373E-02*Px+0*Py+0*Pz+0 == 0;
eqn2 =
0.85226003438856*Py.^5+2.59843785278887*Pz.^2.*Py.^3+2.59843785278887*Px.^2.*Py.^3
+0.220080752066131*Py.^3+1.29921892639443*Pz.^4.*Py+1.29921892639443*Px.^4.*Py+-
6.12659833446545*Pz.^2.*Px.^2.*Py+0.344687393813874*Pz.^2.*Py+0.344687393813874*P
x.^2.*Py+-9.94742781887373E-02*Py+0*Pz+0*Px+0 == 0;
eqn3 =
0.85226003438856*Pz.^5+2.59843785278887*Px.^2.*Pz.^3+2.59843785278887*Py.^2.*Pz.^3
+0.220080752066131*Pz.^3+1.29921892639443*Px.^4.*Pz+1.29921892639443*Py.^4.*Pz+-
6.12659833446545*Px.^2.*Py.^2.*Pz+0.344687393813874*Px.^2.*Pz+0.344687393813874*P
y.^2.*Pz+-9.94742781887373E-02*Pz+0*Px+0*Py+0 == 0;
[solPx,solPy,solPz] = vpasolve(eqn1,eqn2,eqn3);
file = fopen('001.txt','w');
```

```
fprintf(file,'%f\r\n',0);
fprintf(file,'%f\r\n',0);
fprintf(file,'%f\r\n',0);
fprintf(file,'%f\r\n',0);
fprintf(file,'%f\r\n',0);
fprintf(file,'%f\r\n',0);
fprintf(file,'%f\r\n',0);
fprintf(file,'%f\r\n',0);
fprintf(file,'%f\r\n',0);
fprintf(file,'%f\r\n','');
fprintf(file,'%f\r\n',solPx);
fprintf(file,'%f\r\n',solPy);
fprintf(file,'%f\r\n',solPz);
fclose(file);
```

REFERENCES

[1] G. Shirane, F. Jona, Ferroelectric crystals, Dover, New York, 1993.

[2] J. Scott, Ferroelectric memories, Springer-Verlag, Berlin, 2000.

[3] P. Muralt, Ferroelectric thin films for micro-sensors and actuators: a review, J. Micromechanics Microengineering. 10 (2000) 136–146.

[4] S. Trolier-Mckinstry, P. Muralt, Thin Film Piezoelectrics for MEMS, J. Electroceramics. 12 (2004) 7–17.

[5] A.F. Devonshire, Theory of ferroelectrics, Adv. Phys. 3 (1954) 85.

[6] J.F. Nye, Physical properties of crystals : their representation by tensors and matrices, Clarendon Press, 1985.

[7] W. Cao, L.E. Cross, Theory of tetragonal twin structures in ferroelectric perovskites with a first-order phase transition, Phys. Rev. B. 44 (1991) 5–12.

[8] S. Nambu, D.A. Sagala, Domain formation and elastic long-range interaction in ferroelectric perovskites, Phys. Rev. B. 50 (1994) 5838–5847.

[9] N.A. Pertsev, A.G. Zembilgotov, A.K. Tagantsev, Effect of Mechanical Boundary Conditions on Phase Diagrams of Epitaxial Ferroelectric Thin Films, 80 (1998).

[10] N.A. Pertsev, V.G. Kukhar, H. Kohlstedt, R. Waser, Phase diagrams and physical properties of single-domain epitaxial $Pb(Zr_{1-x}Ti_x)O_3$ thin films, Phys. Rev. B. 67 (2003) 054107.

[11] Y.L. Li, S. Choudhury, Z.K. Liu, L.Q. Chen, Effect of external mechanical constraints on the phase diagram of epitaxial $PbZr_{1-x}Ti_xO_3$ thin films—thermodynamic calculations and phase-field simulations, Appl. Phys. Lett. 83 (2003) 1608–1610.

[12] M. Chiang, D.P. Birnie, W.D. Kingery, Physical Ceramics Principles for Ceramic Science and Engineering, 1997.

[13] S.C. Abrahams, Ferroelasticity, Mater. Res. Bull. 6 (1971) 881–890.

[14] E.K.H. Salje, Ferroelastic Materials, Annu. Rev. Mater. Res. 42 (2012) 265–283.

[15] S.-E. Park, S. Wada, L.E. Cross, T.R. Shrout, Crystallographically engineered single crystals for high-performance piezoelectrics, J. Appl. Phys. 86 (1999).

[16] W. Lu, D.N. Fang, C.Q. Li, K.C. Hwang, Nonlinear electric-mechanical behavior and micromechanics modelling of ferroelectric domain evolution, Acta Mater., 47 (1999) 2913-2926.

[17] H. Landolt, S.G.T. Europe, Numerical data and functional relationships in science and technology: new series. Group 4, Physical chemistry: Vol. 19, Thermodynamic properties of, (2007).

[18] M. Zgonik, P. Bernasconi, M. Duelli, R. Schlesser, P. Gunter, M.H. Garrett, D. Rytz, Y. Zhu, X. Wu, Dielectric, elastic, piezoelectric, electro-optic, and elasto-optic tensors of $BaTiO_3$ crystals, Phys. Rev. B. 50 (1994).

[19] S. Wada, S. Suzuki, T. Noma, T. Suzuki, M. Osada, M. Kakihana, S.-E. Park, L.E. Cross, T.R. Shrout, Enhanced Piezoelectric Property of Barium Titanate Single Crystals with Engineered Domain Configurations in situ domain observation, in situ Raman measurement, crystallographic orientation, electric-field induced phase transition, Jpn. J. Appl. Phys. Japanese J. Appl. Phys. 38 (1999) 5505–5511.

[20] M.C. Ehmke, N.H. Khansur, J.E. Daniels, J.E. Blendell, K.J. Bowman, Resolving structural contributions to the electric-field-induced strain in lead-free $(1-x)Ba(Zr_{0.2}Ti_{0.8})O_3$-$x(Ba_{0.7}Ca_{0.3})TiO_3$ piezoceramics, Acta Mater., 66 (2014) 340-348.

[21] B. Narayan, J.S. Malhotra, R. Pandey, K. Yaddanapudi, P. Nukala, B. Dkhil, A. Senyshyn, R. Ranjan, Electrostrain in excess of 1% in polycrystalline piezoelectrics, Nat. Mater. 17 (2018) 427.

[22] S. Yasui, K. Yazawa, M. Matsushima, T. Yamada, H. Morioka, H. Uchida, T. Iijima, L. You, J. Wang, T. Yamamoto, Y. Ikuhara, H. Funakubo, Unusual 90° domain structure in $(2/3)Bi(Zn_{1/2}Ti_{1/2})O_3$-$(1/3)BiFeO_3$ epitaxial films with giant 22% tetragonal distortion, Appl. Phys. Lett. 103 (2013) 42904.

[23] H. Fu, R.E. Cohen, Polarization rotation mechanism for ultrahigh electromechanical response in single-crystal piezoelectrics, Nature. 403 (2000) 281-283.

[24] W. Ge, H. Cao, J. Li, D. Viehland, Q. Zhang, H. Luo, Influence of dc-bias on phase stability in Mn-doped Na0.5 Bi0.5 TiO3 - 5.6 at. % BaTiO3 single crystals, Appl. Phys. Lett. 95 (2009) 162903.

[25] J.E. Daniels, W. Jo, J. Rödel, J.L. Jones, Electric-field-induced phase transformation at a lead-free morphotropic phase boundary: Case study in a 93% $(Bi_{0.5}Na_{0.5})TiO_3$ -7% $BaTiO_3$ piezoelectric ceramic, Appl. Phys. Lett. 95 (2009) 032904.

[26] A.K. Kalyani, D.K. Khatua, B. Loukya, R. Datta, A.N. Fitch, A. Senyshyn, R. Ranjan, Metastable monoclinic and orthorhombic phases and electric field induced irreversible phase transformation at room temperature in the lead-free classical ferroelectric BaTiO3, Phys. Rev. B 91 (2015) 104104.

[27] R. Guo, L.E. Cross, S.-E. Park, B. Noheda, D.E. Cox, G. Shirane, Origin of the High Piezoelectric Response in $PbZr_{1-x}Ti_xO_3$, Phys. Rev. Lett. 84 (2000) 5423–5426.

[28] B. Noheda, D.E. Cox, G. Shirane, J.A. Gonzalo, L.E. Cross, S.-E. Park, A monoclinic ferroelectric phase in the $Pb(Zr_{1-x}Ti_x)O_3$ solid solution, Appl. Phys. Lett. 74 (1999) 2059–2061.

[29] Y. Saito, H. Takao, T. Tani, T. Nonoyama, K. Takatori, T. Homma, T. Nagaya, M. Nakamura, Lead-free piezoceramics, Nature. 432 (2004) 84–87.

[30] S.O. Leontsev, R.E. Eitel, Progress in engineering high strain lead-free piezoelectric ceramics, Sci. Technol. Adv. Mater. 11 (2010) 044302.

[31] C.A. Randall, N. Kim, J.-P. Kucera, W. Cao, T.R. Shrout, Intrinsic and Extrinsic Size Effects in Fine-Grained Morphotropic-Phase-Boundary Lead Zirconate Titanate Ceramics, J. Am. Ceram. Soc. 81 (1998) 677–688.

[32] Y. Huan, X. Wang, J. Fang, L. Li, Grain size effect on piezoelectric and ferroelectric properties of $BaTiO_3$ ceramics, J. Eur. Ceram. Soc. 34 (2014) 1445–1448.

[33] Y. Huan, X. Wang, J. Fang, L. Li, Grain Size Effects on Piezoelectric Properties and Domain Structure of $BaTiO_3$ Ceramics Prepared by Two-Step Sintering, J. Am. Ceram. Soc. 96 (2013) 3369–3371.

[34] D. Ghosh, A. Sakata, J. Carter, P.A. Thomas, H. Han, J.C. Nino, J.L. Jones, Domain Wall Displacement is the Origin of Superior Permittivity and Piezoelectricity in $BaTiO_3$ at Intermediate Grain Sizes, Adv. Funct. Mater. 24 (2014) 885–896.

[35] Z. Zhao, V. Buscaglia, M. Viviani, M.T. Buscaglia, L. Mitoseriu, A. Testino, M. Nygren, M. Johnsson, P. Nanni, Grain-size effects on the ferroelectric behavior of dense nanocrystalline $BaTiO_3$ ceramics, Phys. Rev. B 70 (2004) 024107.

[36] M. Budimir, D. Damjanovic, N. Setter, Enhancement of the piezoelectric response of tetragonal perovskite single crystals by uniaxial stress applied along the polar axis: A free-energy approach, Phys. Rev. B. 72 (2005) 064107.

[37] J.-W. Lee, C.-S. Park, M. Kim, H.-E. Kim, Effects of Residual Stress on the Electrical Properties of PZT Films, J. Am. Ceram. Soc. 90 (2007) 1077–1080.

[38] V.R. Vedula, S.J. Glass, D.M. Saylor, G.S. Rohrer, W.C. Carter, S.A. Langer, E.R. Fuller, Residual-Stress Predictions in Polycrystalline Alumina, J. Am. Ceram. Soc. 84 (2001) 2947–2954.

[39] H. Simons, A.B. Haugen, A.C. Jakobsen, S. Schmidt, F. Stöhr, M. Majkut, C. Detlefs, J.E. Daniels, D. Damjanovic, H.F. Poulsen, Long-range symmetry breaking in embedded ferroelectrics, Nat. Mater. 17 (2018) 814–819.

[40] A. Pramanick, D. Damjanovic, J.E. Daniels, J.C. Nino, J.L. Jones, Origins of Electro-Mechanical Coupling in Polycrystalline Ferroelectrics During Subcoercive Electrical Loading, J. Am. Ceram. Soc. 94 (2011) 293–309.

[41] Y. Jing, S. Leach, R.E. García, J.E. Blendell, R.E. Garc, Correlated inter-grain switching in polycrystalline ferroelectric thin films, J. Appl. Phys. 116 (2014).

[42] J.D. Eshelby, The Determination of the Elastic Field of an Ellipsoidal Inclusion, and Related Problems, Proc. R. Soc. A Math. Phys. Eng. Sci. 241 (1957) 376–396.

[43] D.A. Hall, A. Steuwer, B. Cherdhirunkorn, P.J. Withers, T. Mori, Micromechanics of residual stress and texture development due to poling in polycrystalline ferroelectric ceramics, J. Mech. Phys. Solids. 53 (2005) 249–260.

[44] T. Mura, Micromechanics of defects in solids, Martinus Nijhoff, Boston (1987).

[45] W. Deeg, The analysis of dislocation, crack, and inclusion problems in piezoelectric solids, Ph.D. Dissertation, Stanford University, Stanford, California (1980).

[46] D.M. Barnett, J. Lothe, Dislocations and line charges in anisotropic piezoelectric insulators, Phys. Status Solidi. 67 (1975) 105–111.

[47] M.L. Dunn, Electroelastic Green's functions for transversely isotropic piezoelectric media and their application to the solution of inclusion and inhomogeneity problems, Int. J. Eng. Sci. 32(1) (1994) 119-131.

[48] M.L. Dunn, H.A. Wienecke, Inclusions and inhomogeneities in transversely isotropic piezoelectric solids, Int. J. Solids Struct. 34 (1997) 357.

[49] J. Li, Orientation-dependent piezoelectric Eshelby S-tensor for a lamellar structure in a transversely isotropic medium, Acta Mech. 162 (2003) 69–81.

[50] K. Yazawa, H. Uchida, J.E. Blendell, Origin of Grain Size Effects on Voltage-Driven Ferroelastic Domain Evolution in Polycrystalline Tetragonal Lead Zirconate Titanate Thin Film, Adv. Funct. Mater. 30 (2020) 1909100.

[51] M. Acosta, N. Novak, V. Rojas, S. Patel, R. Vaish, J. Koruza, G.A. Rossetti, J. Rödel, $BaTiO_3$ -based piezoelectrics: Fundamentals, current status, and perspectives, Appl. Phys. Rev. 4 (2017) 041305.

[52] Z. Zhao, K. Bowman, R.E. García, Modeling 180° Domain Switching Population Dynamics in Polycrystalline Ferroelectrics, J. Am. Ceram. Soc. 95 (2012) 1619–1627.

[53] D.M. Marincel, H. Zhang, A. Kumar, S. Jesse, S. V. Kalinin, W.M. Rainforth, I.M. Reaney, C.A. Randall, S. Trolier-McKinstry, Influence of a Single Grain Boundary on Domain Wall Motion in Ferroelectrics, Adv. Funct. Mater. 24 (2014) 1409–1417.

[54] A. Gruverman, O. Auciello, H. Tokumoto, Imaging and control of domain structures in ferroelectric thin films via scanning force microscopy, Annu. Rev. Mater. Sci. 28 (1998) 101–23.

[55] A. Wu, P.M. Vilarinho, I.M.M. Salvado, J.L. Baptista, Sol-Gel Preparation of Lead Zirconate Titanate Powders and Ceramics: Effect of Alkoxide Stabilizers and Lead Precursors, J. Am. Ceram. Soc. 83 (2000) 1379–1385.

[56] A.Z. Simões, T.B. Onofre, F. Moura, Piezoresponse force microscopy, J. Adv. Microsc. Res. 5 (2010) 129–136.

[57] S. V. Kalinin, B.J. Rodriguez, S. Jesse, J. Shin, A.P. Baddorf, P. Gupta, H. Jain, D.B. Williams, A. Gruverman, Vector Piezoresponse Force Microscopy, Microsc. Microanal. 12 (2006) 206–220.

[58] B.J. Rodriguez, A. Gruverman, A.I. Kingon, R.J. Nemanich, J.S. Cross, Three-dimensional high-resolution reconstruction of polarization in ferroelectric capacitors by piezoresponse force microscopy, J. Appl. Phys. 95 (2004) 1958–1962.

[59] Y. Jing, J.E. Blendell, K.J. Bowman, Three dimensional piezoresponse force microscopy polarization difference maps, J. Appl. Phys. 109 (2011).

[60] T. Tsurumi, Y. Kumano, N. Ohashi, T. Takenaka, O. Fukunaga, 90° Domain Reorientation and Electric-Field-Induced Strain of Tetragonal Lead Zirconate Titanate Ceramics, Jpn. J. Appl. Phys. 36 (1997) 5970–5975.

[61] H. Kungl, T. Fett, S. Wagner, M.J. Hoffmann, Nonlinearity of strain and strain hysteresis in morphotropic LaSr-doped lead zirconate titanate under unipolar cycling with high electric fields, J. Appl. Phys. 101 (2007) 044101.

[62] X. Qi, J. Dho, R. Tomov, M.G. Blamire, J.L. MacManus-Driscoll, Greatly reduced leakage current and conduction mechanism in aliovalent-ion-doped $BiFeO_3$, Appl. Phys. Lett. 86 (2005) 062903.

[63] G.D. Hu, S.H. Fan, C.H. Yang, W.B. Wu, Low leakage current and enhanced ferroelectric properties of Ti and Zn codoped $BiFeO_3$ thin film, Appl. Phys. Lett. 92 (2008) 192905.

[64] W. Cao, C.A. Randall, Grain size and domain size relations in bulk ceramic ferroelectric materials, J. Phys. Chem. Solids. 57 (1996) 1499–1505.

[65] Y. Ivry, D.P. Chu, C. Durkan, Bundles of polytwins as meta-elastic domains in the thin polycrystalline simple multi-ferroic system PZT, Nanotechnology. 21 (2010) 065702.

[66] F. Griggio, S. Jesse, A. Kumar, O. Ovchinnikov, H. Kim, T.N. Jackson, D. Damjanovic, S. V. Kalinin, S. Trolier-Mckinstry, Substrate clamping effects on irreversible domain wall dynamics in lead zirconate titanate thin films, Phys. Rev. Lett. 108 (2012) 157604.

[67] E. Burcsu, G. Ravichandran, K. Bhattacharya, G. Ravichandran, Large strain electrostrictive actuation in barium titanate, Appl. Phys. Lett. 77 (2000) 1698–1619.

[68] X. Ren, Large electric-field-induced strain in ferroelectric crystals by point-defect-mediated reversible domain switching, Nat. Mater. 3 (2004) 91–94.

[69] A.R. Damodaran, S. Pandya, J.C. Agar, Y. Cao, R.K. Vasudevan, R. Xu, S. Saremi, Q. Li, J. Kim, M.R. McCarter, L.R. Dedon, T. Angsten, N. Balke, S. Jesse, M. Asta, S. V. Kalinin, L.W. Martin, Three-State Ferroelastic Switching and Large Electromechanical Responses in $PbTiO_3$ Thin Films, Adv. Mater. 29 (2017) 1702069.

[70] H. Béa, M. Bibes, F. Ott, B. Dupé, X.-H. Zhu, S. Petit, S. Fusil, C. Deranlot, K. Bouzehouane, A. Barthélémy, Mechanisms of Exchange Bias with Multiferroic $BiFeO_3$ Epitaxial Thin Films, Phys. Rev. Lett. 100 (2008) 017204.

[71] J. Dho, X. Qi, H. Kim, J.L. MacManus-Driscoll, M.G. Blamire, Large Electric Polarization and Exchange Bias in Multiferroic $BiFeO_3$, Adv. Mater. 18 (2006) 1445–1448.

[72] J.T. Heron, J.L. Bosse, Q. He, Y. Gao, M. Trassin, L. Ye, J.D. Clarkson, C. Wang, J. Liu, S. Salahuddin, D.C. Ralph, D.G. Schlom, J. ñiguez, B.D. Huey, R. Ramesh, Deterministic switching of ferromagnetism at room temperature using an electric field, Nature. 516 (2014) 370-373.

[73] Y. Kutes, L. Ye, Y. Zhou, S. Pang, B.D. Huey, N.P. Padture, Direct Observation of Ferroelectric Domains in Solution-Processed $CH_3NH_3PbI_3$ Perovskite Thin Films, J. Phys. Chem. Lett. 5 (2014) 3335–3339.

[74] M. Coll, A. Gomez, E. Mas-Marza, O. Almora, G. Garcia-Belmonte, M. Campoy-Quiles, J. Bisquert, Polarization Switching and Light-Enhanced Piezoelectricity in Lead Halide Perovskites, J. Phys. Chem. Lett. 6 (2015) 1408–1413.

[75] A.K. Tagantsev, L.E. Cross, J. Fousek, Domains in Ferroelectric Crystals and Thin Films (Springer, 2010).

[76] C. B. Eom, K. J. Choi, M. Biegalski, Y. L. Li, A. Sharan, J. Schubert, R. Uecker, P. Reiche, Y. B. Chen, X. Q. Pan, V. Gopalan, L.-Q. Chen, D. G. Schlom, Enhancement of Ferroelectricity in Strained $BaTiO_3$ Thin Films, Science 306 (2004) 1005-1009.

[77] D. Zhou, M. Kamlah, High-field dielectric and piezoelectric performance of soft lead zirconate titanate piezoceramics under combined electromechanical loading, J. Appl. Phys. 96 (2004) 6634–6641.

[78] C.S. Lynch, The effect of uniaxial stress on the electro-mechanical response of 8/65/35 PLZT, Acta Mater. 44 (1996) 4137–4148.

[79] R.J. Zeches, M.D. Rossell, J.X. Zhang, A.J. Hatt, Q. He, C.H. Yang, A. Kumar, C.H. Wang, A. Melville, C. Adamo, G. Sheng, Y.H. Chu, J.F. Ihlefeld, R. Erni, C. Ederer, V. Gopalan, L.Q. Chen, D.G. Schldin, N.A. Spaldin, L.W. Martin, R. Ramesh, A strain-driven morphotropic phase boundary in $BiFeO_3$, Science 326 (2009) 977–980.

[80] J.X. Zhang, B. Xiang, Q. He, J. Seidel, R.J. Zeches, P. Yu, S.Y. Yang, C.H. Wang, Y.H. Chu, L.W. Martin, A.M. Minor, R. Ramesh, Large field-induced strains in a lead-free piezoelectric material, Nat. Nanotechnol. 6 (2011) 98–102.

[81] Y.J. Li, J.J. Wang, J.C. Ye, X.X. Ke, G.Y. Gou, Y. Wei, F. Xue, J. Wang, C.S. Wang, R.C. Peng, X.L. Deng, Y. Yang, X.B. Ren, L.Q. Chen, C.W. Nan, J.X. Zhang, Mechanical switching of nanoscale multiferroic phase boundaries, Adv. Funct. Mater. 25 (2015) 3405–3413.

[82] Z. Chen, Z. Luo, C. Huang, Y. Qi, P. Yang, L. You, C. Hu, T. Wu, J. Wang, C. Gao, T. Sritharan, L. Chen, Low-symmetry monoclinic phases and polarization rotation path mediated by epitaxial strain in multiferroic $BiFeO_3$ thin films, Adv. Funct. Mater. 21 (2011) 133–138.

[83] L. Bellaiche, A. García, D. Vanderbilt, Electric-field induced polarization paths in $Pb(Zr_{1-x}Ti_x)O_3$ alloys, Phys. Rev. B. 64 (2001) 060103.

[84] H. Cao, C.P. Devreugd, W. Ge, J. Li, D. Viehland, H. Luo, X. Zhao, Monoclinic M_C phase in (001) field cooled $BaTiO_3$ single crystals, Appl. Phys. Lett. 94 (2009) 032901.

[85] W.C. Carter, J.E. Taylor, J.W. Cahn, Variational methods for microstructural-evolution theories, JOM. 49 (1997) 30–36.

[86] M.J. Haun, E. Furman, S.J. Jang, L.E. Cross, Thermodynamic theory of the lead zirconate-titanatesolid solution system, part I: Phenomenology, Ferroelectrics. 99 (1989) 13–25.

[87] L.-Q. Chen, in Physics of Ferroelectrics: A Modern Perspective, in: Phys. Ferroelectr., 2007: pp. 363–372.

[88] M.J. Haun, Z.Q. Zhuang, E. Furman, S.-J. Jang, L.E. Cross, Electrostrictive Properties of the lead Zirconate Titanate Solid-Solution System, J. Am. Ceram. Soc. 72 (1989) 1140–1144.

[89] A.J. Bell, L.E. Cross, A phenomenological gibbs function for $BaTiO_3$ giving correct e field dependence of all ferroelectric phase changes, Ferroelectrics. 59 (1984) 197–203.

[90] J. Hlinka, P. Márton, Phenomenological model of a 90° domain wall in $BaTiO_3$ -type ferroelectrics, Phys. Rev. B 74 (2006) 104104.

[91] R.A. Granger, Fluid Mechanics, Dover, New York, 1995.

[92] B. Noheda, D.E. Cox, G. Shirane, J.A. Gonzalo, L.E. Cross, S.-E. Park, A monoclinic ferroelectric phase in the solid solution, Appl. Phys. Lett. 74 (1999) 2059–1804.

[93] M. Davis, M. Budimir, D. Damjanovic, N. Setter, Rotator and extender ferroelectrics: Importance of the shear coefficient to the piezoelectric properties of domain-engineered crystals and ceramics, J. Appl. Phys. 101 (2007) 054112.

[94] M. Nakajima, S. Okamoto, H. Nakaki, T. Yamada, H. Funakubo, Enhancement of piezoelectric response in (100)/(001) oriented tetragonal Pb(Zr, Ti)O_3 films by controlling tetragonality and volume fraction of the (001) orientation, J. Appl. Phys. 109 (2011).

[95] B. Noheda, D.E. Cox, G. Shirane, R. Guo, B. Jones, L.E. Cross, Stability of the monoclinic phase in the ferroelectric perovskite $PbZr_{1-x}Ti_xO_3$, Phys. Rev. B. 63 (2000) 014103.

[96] K. Yazawa, S. Yasui, H. Morioka, T. Yamada, H. Uchida, A. Gruverman, H. Funakubo, Composition dependence of crystal structure and electrical properties for epitaxial films of $Bi(Zn_{1/2}Ti_{1/2})O_3$–$BiFeO_3$ solid solution system, J. Ceram. Soc. Japan. 118 (2010) 659–663.

[97] K. Yazawa, B. Ducharne, H. Uchida, H. Funakubo, J.E. Blendell, Barkhausen noise analysis of thin film ferroelectrics, Appl. Phys. Lett. 117 (2020) 012902.

[98] M. Lindgren, T. Lepistö, Application of a novel type Barkhausen noise sensor to continuous fatigue monitoring, NDT E Int. 33 (2000) 423–428.

[99] I. Altpeter, R. Tschuncky, K. Szielasko, Electromagnetic Techniques for Materials Characterization, in: Mater. Charact. Using Nondestruct. Eval. Methods, Elsevier Inc., 2016: pp. 225–262.

[100] G. Bertotti, Hysteresis in magnetism: for physicists, materials scientists, and engineers, Academic Press, 1998.

[101] J.S. Urbach, R.C. Madison, J.T. Markert, Reproducibility of magnetic avalanches in an Fe-Ni-Co ferromagnet, Phys. Rev. Lett. 75 (1995) 4694–4697.

[102] J.R. Petta, M.B. Weissman, K.P. O'Brien, Multiple magnetization paths in Barkhausen noise, Phys. Rev. E. 54 (1996) R1029.

[103] J.R. Petta, M.B. Weissman, G. Durin, Dependence of barkhausen pattern reproducibility on hysteresis loop size, Phys. Rev. 56 (1997) 2776–2780.

[104] X. Kleber, A. Vincent, On the role of residual internal stresses and dislocations on Barkhausen noise in plastically deformed steel, NDT E Int. 37 (2004) 439–445.

[105] X. Kleber, S.P. Barroso, Investigation of shot-peened austenitic stainless steel 304L by means of magnetic Barkhausen noise, Mater. Sci. Eng. A. 527 (2010) 6046–6052.

[106] K. Gurruchaga, A. Martínez-De-Guerenu, M. Soto, F. Arizti, Magnetic barkhausen noise for characterization of recovery and recrystallization, in: IEEE Trans. Magn., 2010: pp. 513–516.

[107] B. Ducharne, B. Gupta, Y. Hebrard, J.B. Coudert, Phenomenological model of barkhausen noise under mechanical and magnetic excitations, IEEE Trans. Magn. 54 (2018).

[108] B. Ducharne, M.Q. Le, G. Sebald, P.J. Cottinet, D. Guyomar, Y. Hebrard, Characterization and modeling of magnetic domain wall dynamics using reconstituted hysteresis loops from Barkhausen noise, J. Magn. Magn. Mater. 432 (2017) 231–238.

[109] B. Gupta, B. Ducharne, T. Uchimoto, G. Sebald, T. Miyazaki, T. Takagi, Non-destructive testing on creep degraded 12% Cr-Mo-W-V ferritic test samples using Barkhausen noise, J. Magn. Magn. Mater. 498 (2020).

[110] R.C. Smith, C.L. Hom, Domain Wall Theory for Ferroelectric Hysteresis, J. Intell. Mater. Syst. Struct. 10 (1999) 195–213.

[111] C. Dehoff, B.J. Rodriguez, A.I. Kingon, R.J. Nemanich, A. Gruverman, J.S. Cross, Atomic force microscopy-based experimental setup for studying domain switching dynamics in ferroelectric capacitors, Rev. Sci. Instrum. 76 (2005) 023708.

[112] B.J. Rodriguez, R.J. Nemanich, A. Kingon, A. Gruverman, S. V. Kalinin, K. Terabe, X.Y. Liu, K. Kitamura, Domain growth kinetics in lithium niobate single crystals studied by piezoresponse force microscopy, Appl. Phys. Lett. 86 (2005) 012906.

[113] W.J. Merz, Domain formation and domain wall motions in ferroelectric $BaTiO_3$ single crystals, Phys. Rev. 95 (1954) 690–698.

[114] E.K.H. Salje, E. Dul'kin, M. Roth, Acoustic emission during the ferroelectric transition Pm $\bar{3}$m to P4mm in $BaTiO_3$ and the ferroelastic transition R $\bar{3}$m-C2/c in $Pb_3(PO_4)_2$, Appl. Phys. Lett. 106 (2015) 152903.

[115] R.J. Harrison, E.K.H. Salje, The noise of the needle: Avalanches of a single progressing needle domain in $LaAlO_3$, Appl. Phys. Lett. 97 (2010) 021907.

[116] C.D. Tan, C. Flannigan, J. Gardner, F.D. Morrison, E.K.H. Salje, J.F. Scott, Electrical studies of Barkhausen switching noise in ferroelectric PZT: Critical exponents and temperature dependence, Phys. Rev. Mater. 3 (2019) 034402.

[117] V.Y. Shur, E.L. Rumyantsev, S.D. Makarov, V. V. Volegov, How to extract information about domain kinetics in thin ferroelectric films from switching transient current data, Integr. Ferroelectr. 5 (1994) 293–301.

[118] T. Tybell, P. Paruch, T. Giamarchi, J.-M. Triscone, Domain Wall Creep in Epitaxial Ferroelectric $Pb(Zr_{0.2}Ti_{0.8})O_3$ Thin Films, Phys. Rev. Lett. 89 (2002) 097601.

[119] B.J. Rodriguez, Y.H. Chu, R. Ramesh, S. V. Kalinin, Ferroelectric domain wall pinning at a bicrystal grain boundary in bismuth ferrite, Appl. Phys. Lett. 93 (2008) 142901.

PUBLICATIONS

Publications related to this work

K. Yazawa, R. E. García and J. E. Blendell, "Stress-Induced Metastable Phases and Ferroelastic Switching Mechanisms", Commun. Phys., submitted.

K. Yazawa, B. Ducharne, H. Uchida, H. Funakubo and J. E. Blendell, "Barkhausen Noise Analysis of Thin Film Ferroelectrics", Appl. Phys. Lett., 117 (2020) 012902.

K. Yazawa, H. Uchida and J. E. Blendell, "Origin of grain size effects on voltage driven ferroelastic domain evolution in polycrystalline lead zirconate titanate thin film", Adv. Funct. Mater., 30 (2020) 1909100.

Publications not related to this work

K. Yazawa, M. Parsons, A. Jackson, W. Chen, A. Campbell, J. Blendell, C. Handwerker and P. Su, "An evaluation of effects of molding compound properties on the reliability of Ag wire bonded components", Electronic Components and Technology Conference (ECTC) IEEE 67th, (2017) 2231-2236.

K. Yazawa, S. Yasui, H. Morioka, T. Yamada, H. Uchida, A. Gruverman, and H. Funakubo, "Composition dependence of crystal structure and electrical properties for epitaxial films of $Bi(Zn_{1/2}Ti_{1/2})O_3$-$BiFeO_3$ solid solution system", J. Ceram. Soc. Jpn. 118 (2010) 659-663.

K. Yazawa, S. Yasui, M. Matsushima, H. Uchida and H. Funakubo, "MOCVD growth and characterization of $BiFeO_3$–$Bi(Zn_{1/2}Ti_{1/2})O_3$ ferroelectric films", Mater. Sci. Eng. B, 173 (2010) 14-17.

S. Yasui, K. Yazawa, M.Matsushima, T. Yamada, H. Morioka, H. Uchida, T. Iijima, L. You, Junling Wang, T. Yamamoto, Y. Ikuhara, and H. Funakubo, "Unusual 90^{o} domain structure in (2/3)Bi($Zn_{1/2}Ti_{1/2}$)O_3-(1/3)$BiFeO_3$ epitaxial films with giant 22% tetragonal distortion" Appl. Phys. Lett., 103 (2013) 042904-1-5.

S. Yasui, K. Yazawa, T. Yamada, K. Nishida, H. Uchida, M. Azuma, and H. Funakubo, "Effect of film thickness and crystal orientation on the constituent phase in epitaxial $BiFeO_3$-$BiCoO_3$ films grown on $SrTiO_3$ substrates" Jpn. J. Appl. Phys., 49 (2010) 09MB04-1-5.

M. Ishikawa, K. Yazawa, T. Fujisawa, S. Yasui, T. Yamada, T. Hasegawa, T. Morita, M. Kurosawa, and H. Funakubo, "Growth of Epitaxial $KNbO_3$ Thick Films by Hydrothermal Method and Their Characterization", Jpn. J. Appl. Phys., 48 (2009) 09KA14.

M. Ishii, S. Kasuga, K. Yazawa, Y. Sakata, T. Okino, Y. Sato, J. Hirase, Y. Hirose, T. Tamaki, Y. Matsunaga, Y. Kato, "An Ultra-Low Noise Photoconductive Film Image Sensor With a High-speed Column Feedback Amplifier Noise Canceller" VLSI Circuits, 2013 Symposium on, (2013) C8-C9.

H. Funakubo, S. Yasui, K. Yazawa, J. Nagata, T. Oikawa, T. Yamada, H. Uchida, "Development of Novel Pb, Li, Na and K-free Piezoelectric Materials for Si-based MEMS Application" ISAF/ECAPD/PFM, 2012 Intl. Symp., (2012) 1-2.

Y. Kamimura, B. Y. Lee, K. Yazawa, H. Funakubo T. Iijima and H. Uchida, "Fabrication and Evaluation of Mn-Substituted Ba($Cu_{1/3}Nb_{2/3}$)O_3 Ceramics" IOP Conference Series: Mater. Sci. & Eng., 18 (2011) 092038.

S. Yasui, O. Sakata, M. Nakajima, S. Utsugi, K. Yazawa, T. Yamada and H. Funakubo, "Piezoelectric Properties of {100}-Oriented Epitaxial $BiCoO_3$–$BiFeO_3$ Films Measured Using Synchrotron X-ray Diffraction", Jpn. J. Appl. Phys., 48 (2009) 09KD06.